BIOLOGICALLY-INSPIRED, ELECTRICALLY SMALL ANTENNA ARRAYS

by

Amir Reza Masoumi

A dissertation submitted in partial fulfillment of
the requirements for the degree of

Doctor of Philosophy

(Electrical and Computer Engineering)

at the

UNIVERSITY OF WISCONSIN–MADISON

2015

Date of final oral examination: 11/19/2014

The dissertation is approved by the following members of the Final Oral Committee:

Nader Behdad, Associate Professor, Electrical and Computer Engineering

Hongrui Jiang, Professor, Electrical and Computer Engineering

Zhenqiang Ma, Professor, Electrical and Computer Engineering

Zongfu Yu, Assistant Professor, Electrical and Computer Engineering

Alan McMillan, Associate Scientist, University of Wisconsin-Madison School of Medicine and Public Health

To mum and dad

and my wonderful sisters

ACKNOWLEDGMENTS

First, I would like to thank my advisor, Professor Nader Behdad, for his supervision and support during my PhD studies. I would also like to thank the committee members, professors Hongrui Jiang, Zhenqiang (Jack) Ma, Zongfu Yu and Dr. Alan McMillan for their time in reviewing my thesis and taking part in my defense.

I would like to thank my officemates/friends Amin Momeni, Kasra Ghaemi, Alireza Ousati Ashtiani, Chien-Hao Liu, Tonmoy Bhatacharjee, Ting-Yen Shih, Yahya Mohtashami, Dr. Arash Rashidi, Dr. Meng Li and Dr. Yazid Yusuf.

I would like to thank Dr. Chiya Saeidi, Solmaz Forutan, Ali Kheirandish, Sharareh Fakhraei, Mohammad Moghimi, Arezoo Movaghar, Mohammad Khabbazian, Amirhossein Davoody, Farhad Karimi, Hadi Moghaddam and Saman Cyrus for their friendship during the past few years.

Finally, I would like to thank my parents and sisters for their never ending love and support.

DISCARD THIS PAGE

TABLE OF CONTENTS

Page

LIST OF TABLES vi

LIST OF FIGURES viii

ABSTRACT xiv

1 Introduction 1

1.1 Motivation 1
1.1.1 Direction Finding 1
1.1.2 High-resolution radar and microwave imaging 3
1.1.3 MIMO Communications 4
1.1.4 Radio Astronomy 4
1.2 Literature Review on Electrically Small Antenna Arrays 5
1.2.1 Superdirectivity 5
1.2.2 Mutual Coupling 5
1.2.3 Addition of a Passive Multi-port Network 6
1.3 Proposed approach: The biomimetic concept 8
1.4 Thesis overview 12
1.4.1 Chapter 2: Biomimetic Antenna Arrays Based on the Directional Hearing Mechanism of the Parasitoid Fly *Ormia Ochracea* 12
1.4.2 Chapter 3: An Improved Architecture for Two-Element Biomimetic Antenna Arrays 13
1.4.3 Chapter 4: Architecture, Design, and Nonlinear Optimization of Three-Element Biomimetic Antenna Arrays 14
1.4.4 Chapter 5: A Two-Element Biomimetic Antenna Array with Enhanced Angular Resolution and Optimized Power Extraction . . . 14

Page

1.4.5 Chapter 6: Bandwidth Enhancement of Biomimetic Antenna Arrays using Non-Foster Coupling Networks 15
1.4.6 Chapter 7: Biomimetic Nano-Antenna Arrays: A Concept for Designing Sub-Wavelength Angle-Sensing Detectors at Optical Wavelengths 15

2 Biomimetic Antenna Arrays Based on the Directional Hearing Mechanism of the Parasitoid Fly *Ormia Ochracea* 16

2.1 Introduction 16
2.2 Theory 17
2.3 Design of Optimized BMAAs 26
2.3.1 BMAA Design Using Ideal Transformers 26
2.3.2 Design of Optimized BMAAs With Nonideal Transformers . . . 32
2.4 Experimental Verification 37
2.5 Conclusions 42

3 An Improved Architecture for Two-Element Biomimetic Antenna Arrays . 45

3.1 Introduction 45
3.2 The Proposed Two-Element BMAA Architecture 47
3.3 Design Example and Measurement Results 50
3.4 Noise Analysis of the BMAA 57
3.5 Conclusions 59

4 Architecture, Design, and Nonlinear Optimization of Three-Element Biomimetic Antenna Arrays 61

4.1 Introduction 61
4.2 Problem Formulation 63
4.3 BMAA Optimization 67
4.4 Conclusions 72

5 A Two-Element Biomimetic Antenna Array with Enhanced Angular Resolution and Optimized Power Extraction 73

5.1 Introduction 73

Appendix

Page

5.2 Optimum BMAA Design 75
5.2.1 Principles of Achieving Angular Phase Sensitivity in Previously-Reported BMAAs 75
5.2.2 Optimum BMAA Design 78
5.3 Experimental verification 84
5.4 Application in Designing Directive End-fire Antenna Arrays 90
5.5 Conclusions 92

6 Bandwidth Enhancement of Biomimetic Antenna Arrays using Non-Foster Coupling Networks 94

6.1 Introduction 94
6.2 Design Procedure 95
6.3 Practical Implementation 100
6.4 Conclusions 102

7 Biomimetic Nano-Antenna Arrays: A Concept for Designing Sub-Wavelength Angle-Sensing Detectors at Optical Wavelengths 105

7.1 Introduction 105
7.2 Sub-wavelength Nano-Antenna Arrays: Design and Principles of Operation 106
7.3 Simualtion Results 108
7.4 Conclusion 111

8 Future work 114

8.1 Design of small aperture compact direction finding systems 114
8.2 MIMO Communications 115
8.3 Infrared angle sensing detectors 115

LIST OF REFERENCES 116

LIST OF TABLES

Table Page

2.1 Calculated Z-parameters of the two monopole antenna system discussed in Section 2.3.1 at 600 MHz. 26

2.2 The four possible implementations of the external coupling network of the BMAA examined in Section 2.3.1. At 600 MHz, the reactance value of X_1 is obtained using an inductor with an inductance of L and the reactance value of $X_2/2$ is obtained using a capacitor with a capacitance of C. 29

3.1 Calculated Y-parameters of the two-element array discussed in Section 3.3 at 600 MHz. The Y-parameters are inclusive of the lengths of the transmission lines that connect the antennas to the external coupling network. 50

3.2 The four possible implementations of the external coupling network of the BMAA examined in Section 3.3. At 600 MHz, the admittance value of B_1 is obtained using an inductor with an inductance of L and the reactance value of $B_2/2$ is obtained using a capacitor with a capacitance of C. 52

4.1 Simulated conductance and susceptance values for the linear three element monopole array at 600 MHz. Each element has a length of $\lambda/4$. All values are reported in mS. 69

4.2 Value of variables found by SNOPT, which maximize the objective and the calculated values for the components of the external coupling network. All values are reported in mS. 70

5.1 Calculated Y-parameters of the two monopole antenna system discussed in Section 5.2 at 600 MHz. 85

Table Page

5.2 Values for the components of the external coupling network (in mS) obtained from an optimization process. 86

5.3 Length and characteristic impedances of the different transmission lines used in the coupling network. 88

6.1 Simulated Y-parameters of the two-element array discussed in Section 6.2 at 500 MHz. The monopoles have a length of 5cm and are spaced 2.5cm apart. Values are in mS. 97

LIST OF FIGURES

Figure Page

1.1 Direction finding based on the received signal amplitude from two crossed electrically small loop antennas [6]. 2

1.2 The Watson-Watt direction finder [6]. 3

1.3 Topology of the decoupling network presented in [31]. 7

1.4 Topology of the decoupling/beamforming network presented in [35]. 8

1.5 Proposed network for optimal noise matching in coupled arrays [36]. 8

1.6 An illustrative view of mechanisms used for directional hearing in humans and insects. (a) Humans have directional hearing capability for sound frequencies in the range of 80 Hz - 20 kHz. The directional hearing capability in humans is aided by the large separation between the two ears (approximately 22-23 cm), the considerable scattering of sound caused by the large head that causes amplitude difference between the received signals, and a powerful brain which can accomplish sophisticated signal processing. (b) In insects such as *Ormia Ochracea*, none of these traits are present. To compensate for this disadvantage, such insects use a coupled-ear system, which enhances the contrast between the two received signals to make it easier for the brain of the animal to distinguish them. Photograph of *O. Ochracea* courtesy of Prof. W. Cade. 10

2.1 (a) Photograph of the parasitoid fly *Ormia Ochracea* (courtesy of Prof. William Cade). (b) Block diagram of a two-element biomimetic antenna array. (c) Equivalent circuit model of a two-element biomimetic antenna array taking into account the mutual coupling effects between the two antennas. 19

Figure Page

2.2 (a) Equivalent circuit model of the two-element biomimetic antenna array shown in Fig. 2.1. (b) The common-mode circuit. (c) The differential-mode circuit. 20

2.3 Variation of maximum phase enhancement factor as a function of output power for the two-element BMAA discussed in Subsection 2.3.1. The result for a hypothetical BMAA composed of two antennas that have the same values of $R_s = \mathrm{Re}(Z_{11})$ but have no mutual coupling between them, i.e., $R_{12} = 0$, is also shown for comparison. 28

2.4 The simulated responses of the four biomimetic antenna arrays examined in Section 2.3.1. (a) The phase responses of the BMAAs employing the external coupling networks identified in Table 2.2. The output phase response of a regular array (the same antennas without the coupling network) has also been included. (b)-(c) The output power of these BMAAs as a function of angle of incidence of the EM wave. The output power values are normalized to P_0, which is the power available from a regular antenna array (A BMAA without coupling network) at boresight. See (2.11). (b) The output power at the contralateral output port. (c) The output power at the ipsilateral output port. The ipsilateral (contralateral) antenna is the one closer (further) from the incident EM wave. 30

2.5 (a) The common mode half circuit of the BMAA. (b) The differential mode half circuit of the BMAA. Here, the transformer is assumed to be nonideal. . 33

2.6 Locus of $Z_{in,\,c}$ as $X_1 + X_2$ varies from $-\infty$ to $+\infty$ and for constant input power to the external coupling network of $P_{in,\,c} = -10$ dB. 35

2.7 The real and imaginary parts of $Z_{in,\,c}$ as a function of $X_1 + X_2$. 36

2.8 Variation of $|\eta|$ as a function of X_1 for a coupling network that results in $P_{out} \approx -12$ dB. 37

2.9 Photograph of the fabricated two-element biomimetic antenna array. (a) 3D view of the two monopoles. (b) The two-input two-output external coupling network. 40

Appendix
Figure Page

2.10 Measured and simulated output phase responses of the two-element BMAA discussed in Section 2.4. The simulated and measured output phase response of the regular array (BMAA without the external coupling network) is also shown. For comparison, the phase difference between two isotropic receiving antennas with a spacing of d, $kd\sin(\theta)$, is also shown. See Fig. 2.1 for definitions of positive and negative incidence angles. 41

2.11 Angular variations of the output power at the two output ports of the BMAA discussed in Section 2.4. The results are normalized to the output power available from the regular array at boresight, P_0 in (2.11). Port 2 is the output closer to the incident wave (the ipsilateral antenna) and port 1 is the output further from the incident EM wave (the contralateral output). 43

3.1 (a) Block diagram of the proposed two-element biomimetic antenna array (BMAA). (b) Equivalent circuit model of the two-element biomimetic antenna array. (c) The common-mode circuit. (d) The differential-mode circuit. 48

3.2 Variation of the maximum phase enhancement factor as a function of the output power for the two-element BMAA discussed in Section 3.3. This curve is obtained for the antenna array whose Y-parameters are provided in Table 5.1. 51

3.3 Measured and simulated output phase responses of the two-element BMAA discussed in Section 3.3 and that of a regular array ($k = \frac{2\pi}{\lambda}$). 54

3.4 Measured and simulated amplitude responses of the two-element BMAA discussed in Section 3.3. Ipsilateral output is closer to the incident wave (port2) and the contralateral output is further from the incident wave (port 1). 55

3.5 Photograph of the fabricated two-input two-output external coupling network used in the BMAA reported in this subsection. 56

3.6 Equivalent circuit of the BMAA for noise analysis. $I_{sc,1}$ and $I_{sc,2}$ are the short circuit currents of the two antennas (without considering noise currents). . . 59

3.7 Simulated output noise spectral density of the two-element BMAA discussed in Section 3.3. 60

Appendix
Figure Page

4.1 Block diagram of a three element biomimetic antenna array. The antennas are assumed to be identical and the external coupling network is symmetric. . . . 63

4.2 a) Equivalent circuit model of the BMAA. b) common-mode circuit. c) differential-mode circuit. 64

4.3 (a) Simulated output phase responses of the three-element BMAA. $\Phi_{out,1} = \measuredangle V_{o1} - \measuredangle V_{o2}$, $\Phi_{out,2} = \measuredangle V_{o3} - \measuredangle V_{o2}$ and $\Phi_{out,3} = \measuredangle V_{o1} - \measuredangle V_{o3}$. (b) Simulated output power of the three-element BMAA. The output power is normalized to the available power from an isolated monopole antenna of the same length as the BMAA antenna elements. 71

5.1 (a) A two-element regular antenna array where the receiving elements are individually impedance matched. (b) Block diagram of a two-element biomimetic antenna array (BMAA). 77

5.2 (a) Block diagram of a two-element biomimetic antenna array. (b) The equivalent circuit model of the two-element BMAA shown in part (a) and the architecture of its external coupling network are shown. 78

5.3 Normalized magnitudes of the short-circuit currents of two 13.5 cm long monopole antennas spaced at a distance of 2.5 cm and operating at 600 MHz. The inset shows the definition of positive and negative angles of incidence and the orientation of antennas 1 and 2 with respect to the incident wave. . . 80

5.4 The equivalent circuit model of the two-element BMAA shown in Fig. 5.2 in the (a) common mode and (b) differential mode of excitation. 81

5.5 (a) Topology of the modified external coupling network. (b) Photograph of the fabricated two-input two-output external coupling network. $C_1 = 3.6$ pF, $C_2 = 6.2$ pF, and $L \approx 19$ nH. Thickness of thick and thin lines are respectively 3.36 mm and 0.8 mm (refer to Fig. 5.2 for port naming conventions). . 87

5.6 Measured and simulated output phase responses of the two-element BMAA discussed in Section 5.2 as well as the phase response corresponding to the propagation of an electromagnetic wave over a distance of d at an angle of θ. 90

Appendix
Figure Page

5.7 Measured and simulated amplitude responses of the two-element BMAA discussed in Section 5.2. Port 2 is the output closer to the incident wave (the ipsilateral antenna) and port 1 is the output further from the incident EM wave (the contralateral antenna). 91

5.8 Block diagram of a two-element end-fire array based on the BMAA presented in this chapter. 91

5.9 Normalized output power at the output of the end-fire array shown in Fig. 5.8 and a regular array followed by a 180° hybrid and phase shifter (the structure shown in Fig. 5.8 without the external coupling network of the BMAA). . . . 92

6.1 Block diagram of a two-element regular antenna array (BMAA). 96

6.2 Variation of the maximum phase enhancement factor as a function of the normalized output power for the two-element BMAA discussed in this chapter. This curve is obtained for the antenna array whose Y-parameters are provided in Table 6.1. 98

6.3 Circuit implementation of the coupling networks discussed in this chapter. a) Passive. b) Non-Foster. c) Common-mode equivalent circuit of non-Foster BMAA at 500 MHz. d) Differential-mode equivalent circuit of non-Foster BMAA at 500 MHz ($\alpha = \pi \frac{d}{\lambda} \sin(\theta)$). 99

6.4 Negative impedance converter (NIC) topology employed for implementing the non-Foster components in this chapter. 101

6.5 Transistor implementation of the non-Foster elements. a) -4.14 pF capacitor. b) -4.6 kΩ resistor in parallel with a -0.185 pF. 102

6.6 Comparison of the real and imaginary parts of the admittance of the non-Foster elements with their corresponding circuit implementations using transistors. a) -4.14 pF capacitor. b) -4.6 kΩ resistor in parallel with a -0.185 pF capacitor. 103

Appendix
Figure Page

6.7 a) Phase enhancement factor as a function of frequency for the three different circuit implementations of the coupling network. b) Normalized output power as a function of frequency. The power is normalized to the available power from the antenna array at 500 MHz. 104

7.1 Permittivity of silicon at optical wavelengths. 108

7.2 (a) Cross sectional view of the asymmetric optical antenna elements located on top of a silicon substrate. (b) Top view of the structure showing dimensions. A thin layer of silicon dioxide is placed between the antenna elements and the silicon substrate. Silicon and silicon dioxide are shown with green and red, respectively. 108

7.3 Magnitude of electric field distribution in the cross sections of the two asymmetric optical antenna elements at two different wavelengths. The structure is illuminated with a plane wave with a transverse electric polarization and an angle-of-incidence of $\theta = 0$. 109

7.4 Ratio of the power absorbed (dissipated) at the cross sections of the two asymmetric elements as a function of the wavelength. 110

7.5 (a) Cross sectional view of the symmetric optical antenna elements located on top of a silicon substrate. (b) Top view of the structure showing dimensions. 111

7.6 Magnitude of electric field distribution in the cross sections of the two optical antenna elements for different angles of incidence. The structure is illuminated with a plane wave with a transverse electric polarization and various different angles of incidence as indicated in each figure. 112

7.7 Ratio of the power absorbed (dissipated) at the cross sections of the two symmetric elements as a function of the angle-of-incidence. The wavelength of the incident wave is $\lambda = 650nm$. 113

ABSTRACT

First, the motivation behind adding a passive external coupling network after antenna arrays is discussed, the concept of biomimetic antenna arrays (BMAAs) introduced and some of the previous work done in this area have been reviewed. Next, a BMAA which achieves an angular resolution of roughly 15 times its regular counterpart is introduced and fully characterized. The introduced BMAA employs transformers which considerably degrade its performance, namely its output power. To cicumvent this shortcoming a new architecture of a BMAA that does not employ transformers and therefore yields a higher output power for the same angular resolution has been subsequently presented. Moreover, a detailed noise analysis of this BMAA is carried out and the output noise of the new architecture is compared with the output noise of the original design. The modified two-element BMAA architecture is then extended to multiple elements. A novel nonlinear optimization process is introduced that maximizes the total power captured by the BMAA for a given angular resolution and the concept illustrated for a three-element antenna array. Next an optimum two-element BMAA which achieves the maximum possible angular resolution while obtaining the same output power level of a regular antenna array with the same elements and spacing is introduced. A novel two-element superdirective array based on this optimum BMAA has been also discussed. The passive BMAAs discussed in

this thesis have a relatively narrow bandwidth. To extend the bandwidth of BMAAs, non-Foster networks have been employed in their external coupling networks and it has been demonstrated that they can increase their bandwidth by a factor of roughly 33. Finally, the BMAA concept has been extended to nano-antenna arrays and a concept for designing sub-wavelength angle-sensing detectors at optical wavelengths has been introduced.

Chapter 1

Introduction

1.1 Motivation

Antenna arrays provide spatial sampling of an incident signal over an aperture [1]. Due to their high cost and large size, they have usually only had applications in high-end military systems such as phased array radars. In recent years, decreasing costs in RF/microwave and digital components and advancements in array signal processing techniques [2] have made the application of antenna arrays in low-cost civilian systems viable. Most of these systems are located on mobile platforms (cell phones, laptop computers,...), where due to space limitations, the distance between elements is relatively small compared to the wavelength. Therefore, electrically small antenna arrays (ESA) have recently become an area of active research. In this section we summarize a few different areas of application for ESAs.

1.1.1 Direction Finding

Direction finding has many applications such as source (transmitter) localization [3], navigation, tracking [4] and channel parameter estimation in modern communication systems [5]. Many simple direction finding systems currently in use utilize the amplitude of the received signal from the elements of a small antenna array to determine the direction of the incoming wave. The elements of the array could be directional or omnidirectional.

Examples of some systems are shown in Fig. 1.1 and Fig. 1.2. In Fig. 1.1 two electrically small loop antennas with figure-eight radiation patterns are placed at a right-angle to eachother. The relative amplitude of the signal received by the two loops can narrow down the direction of the incoming wave to two possible directions (these two directions have a 180^o phase difference). A third omnidirectional antenna is used to generate a blanking signal to resolve this ambiguity. In Fig. 1.2, four omnidirectional antennas are used in pairs of two (blue and orange) to generate two orthogonal beams similar to Fig. 1.1 for direction finding and the signal obtained by summing the outputs of the four elements is used to resolve the ambiguity. This system is often referred to as the Watson-Watt direction finder. As can be seen in both systems, the signals received from the antennas are directly connected to the receiver without any further (analog) processing. The possibility of enhancing the directional resolution of antenna array by adding a passive multi-port network between the antenna array and the receiver is a main area of focus in this thesis.

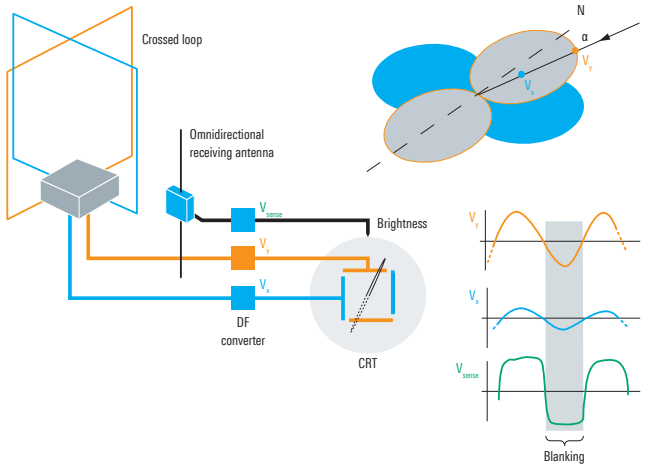

Figure 1.1 Direction finding based on the received signal amplitude from two crossed electrically small loop antennas [6].

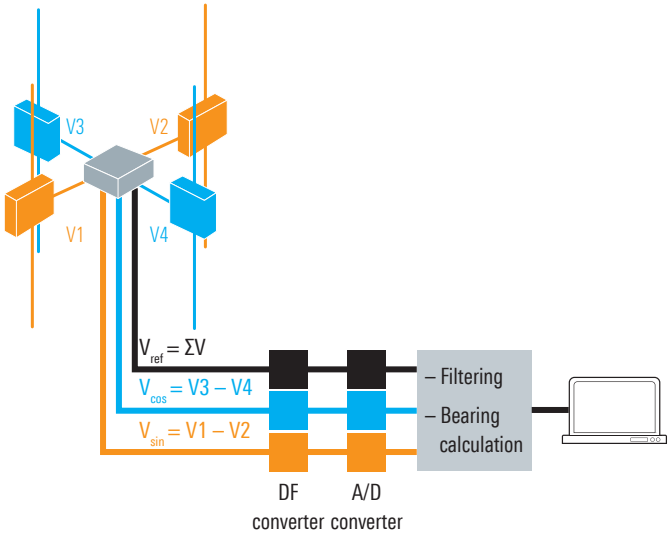

Figure 1.2 The Watson-Watt direction finder [6].

Modern advanced systems use phased array antennas. They employ adaptive beamforming techniques along with algorithms such as MUSIC [7] and ESPRIT [8] for high precision direction finding. They usually have many elements, are expensive and are not investigated in this thesis.

1.1.2 High-resolution radar and microwave imaging

Another potential application of electrically small antenna arrays (ESA) is High-resolution radar imaging systems [9]. For instance the inverse synthetic aperture radar (ISAR) technique uses the radar returns obtained from the elements of an antenna array to form a 2-D image of the target. Such systems have applications in surveillance and reconnaissance, and more recently through-the-wall imaging [10], [11]. To reduce mutual coupling effects, the spacing between the elements is set to half a wavelength. To obtain higher image resolution, more elements are needed in the array and the array size increases. This would

make the use of such systems on mobile/airborne platforms impractical. Small aperture antenna arrays can potentially lead to light-weight high-resolution mobile imaging systems.

1.1.3 MIMO Communications

Multiple-input-multiple-output communications can be thought of as a spatial multiplexing scheme where the signal is split into separate streams and transmitted by different elements of an antenna array in the same frequency band [12]. The transmitted streams are received by elements of a receiving antenna array and if the characteristics of the channel (channel state) is known the original signal is recovered. Increasing the number of antennas in the transmitter and receiver antenna arrays would increase the channel capacity. However, due to space limitations in wireless devices, increasing the number of elements without performance degradation due to large inter-element mutual coupling is unavoidable [13], [14]. The problem is more severe in communication networks operating in the UHF frequency range such as some LTE networks. Small-aperture antenna arrays can potentially have applications in these networks where the wavelength is relatively high compared to the size of wireless devices and therefore large antenna spacings are impractical.

1.1.4 Radio Astronomy

In radio astronomy the signal of interest has very low power density [15]. To increase the received signal power, the effective aperture is increased by increasing the number of antenna elements. For example the planned Square Kilometer Array (SKA) [16] will have a total aperture of one square kilometer by combining the signal received by thousands of small antennas spread over a distance of 3000 km. The large distance between elements

necessitates the use of high capacity links between receiving stations. Small aperture antenna arrays could potentially lead to smaller arrays for radio astronomy.

1.2 Literature Review on Electrically Small Antenna Arrays

1.2.1 Superdirectivity

The spacing between the elements in phased array antennas is usually half the wavelength. This would make phased arrays operating in VHF/UHF frequencies prohibitively large. Therefore, there is a strong need for small aperture low cost antenna arrays that have an enhanced angular accuracy compared to a regular antenna array of the same size. A method for obtaining higher angular resolution is the nonuniform excitation of the antenna elements. It can be shown that if the amplitude of the currents of the antenna elements vary rapidly over distances that are short compared to the wavelength, a higher directivity can be obtained compared to uniform excitation [62], [18]. This phenomenon is commonly referred to as superdirectivity. In a superdirective small aperture antenna array the amplitude of the currents have large variation from element to element [19], [20]. This would make the precise control of the currents (both amplitude and phase) impractical. Moreover, high current values can lead to significant ohmic losses in the antenna array and reduce antenna efficiency. It is for this reason that some researchers have investigated the application of superconductors to superdirective antenna arrays [21], [22]. Due to the aforementioned practical issues of superdirectivity, superdirective arrays have had limited applications in low-cost mobile devices.

1.2.2 Mutual Coupling

If the spacing between the elements in an antenna array is small compared to the wavelength, mutual coupling between the elements can lead to problems such as reduction

of realized gain and radiation efficiency, pattern distortion and reduction of capacity in MIMO communication systems [23], [24], [25]. Mutual coupling can also lead to error in direction-of-arrival (DOA) estimation in small antenna arrays [26]. Due to the aforementioned deleterious effects that mutual coupling has on the performance of small-aperture arrays, much research has been devoted to compensate for its effects. It has been shown that if mutual between antenna elements is completely accounted for and a compensation scheme is implemented in the signal processing algorithm, performance comparable to the case of no mutual coupling present can be obtained [27], [28], [29]. However, current compensation schemes based solely on signal processing techniques require accurate modeling of the location of antenna elements, calibration and are fairly complex. Therefore, it is highly desirable to decouple the antenna elements in the analog domain at front-end of the system rather than compensation in the digital domain.

1.2.3 Addition of a Passive Multi-port Network

There has been considerable work done on adding a passive multi-port network between the antenna array and the signal processing section for the purpose of port decoupling (for arrays in the receive mode) and beamforming (for arrays in the transmit mode) in small aperture antenna arrays [30], [31], [32], [33], [34], [35]. Due to the fact that decoupling networks isolate the different inputs to the antenna array, each port can be independently matched to its respective impedance, thus they can also perform the function of impedance-matching and are commonly referred to as decoupling/impedance matching networks (DCM). Fig. 1.3 shows the topology of the decoupling network presented in [31]. Here, ports 1-3 are isolated from each other even in the presence of strong mutual coupling between the antennas. To avoid any losses in the decoupling network, all the elements are reactive (capacitors or inductors). The authors obtain the actual values from

an optimization routine. As can be seen, this topology is fairly complicated even in the case of three antenna elements.

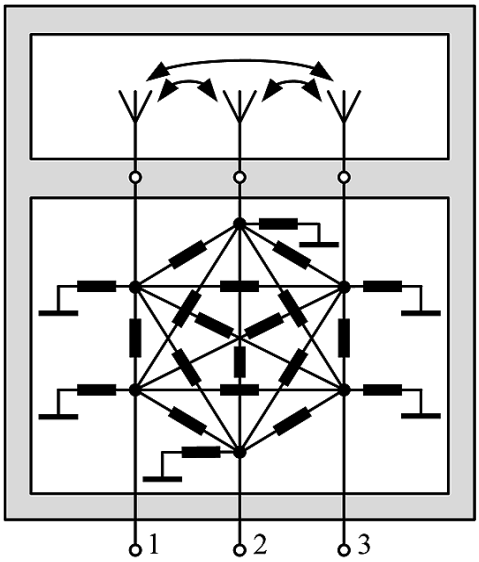

Figure 1.3 Topology of the decoupling network presented in [31].

Another approach for the design of a decoupling network can be seen in Fig. 1.4. The decoupling network employs four rat-race couplers to isolate the inputs from each other. Moreover, due to the fact that the input ports are isolated, each one of the modes of the system can be independently excited and consequently different patterns synthesized. A related concept can be seen in [38], where a multi-port network has been used for the purpose of impedance-matching and optimization of of radiation pattern for maximum gain.

Another purpose of adding a passive multi-port network between the antenna array and the receiver is noise optimization. As we know for any given amplifier, there is an optimal source impedance that minimizes the noise at its output. The question then arises, “For a given coupled antenna array and specified amplifiers what multi-port matching network

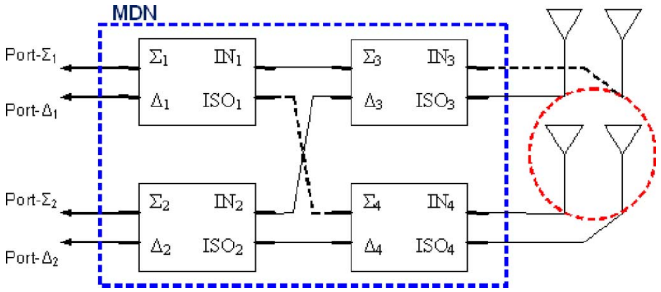

Figure 1.4 Topology of the decoupling/beamforming network presented in [35].

yields the lowest output noise". In [36], [37], the authors have proposed a multi-port matching network which minimizes the noise contributed by the amplifiers.

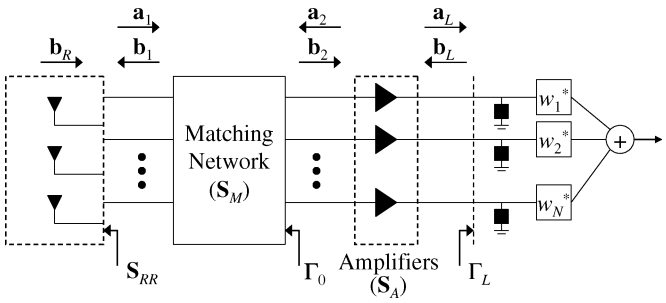

Figure 1.5 Proposed network for optimal noise matching in coupled arrays [36].

1.3 Proposed approach: The biomimetic concept

Directional hearing refers to the capability of humans and most animals in being able to detect the direction of arrival of a sound wave of interest by just listening to it. This ability is one of the keys to survival for many large and small animals in nature [39]. The basic physics underlying the concept of directional hearing is rather straight forward. Most

animals with directional hearing capability have two ears that sense the pressure of the incoming sound wave. Based on its direction of arrival (DoA), the sound wave arrives at one of the ears earlier than the other. In most cases, two ears are separated by a relatively large head that causes significant scattering of sound. This causes the amplitude of the received signal to be larger at the ipsilateral ear (the one closer to the incident sound wave) compared to that of the contralateral ear (the one further away from the incident wave), which is shadowed by the large head. The differences in the time of arrival and the amplitude of the two received signals are the main cues used by the auditory system of most animals to determine the location of the emitting source. In large animals and humans, the separation between the two ears is physically large and significant scattering of sound is created by the large head separating the two ears. Therefore, the contrast between the two received signals is rather large. Additionally, such animals have large brains capable of conducting sophisticated signal processing, which further aids the sense of directional hearing. In small animals and insects that have tympanal hearing capabilities, however, the contrast between the two received signals is very small [39]. Moreover, small animals and insects do not have sophisticated brains, which further complicates the task of directional hearing. Therefore, smaller animals and especially insects are inherently at a disadvantage when it comes to directional hearing. However, despite these disadvantages, many small animals and insects demonstrate acute directional hearing capabilities [42]-[43].

Fig. 1.6 illustrates a system level comparison between the auditory systems of a human and an insect that possesses directional hearing capability. From a system point of view, the auditory system of a human acts as two isolated pressure receivers that convert the pressure of the received sound wave to nerve impulses transmitted to the brain. In a small animal or insect, on the other hand, the auditory system takes advantage of a set of coupled ears that act as a pressure difference receiver [39]-[41]. As seen from Fig. 1.6(b), such an auditory system acts as a two-input two-output system that takes two inputs that have

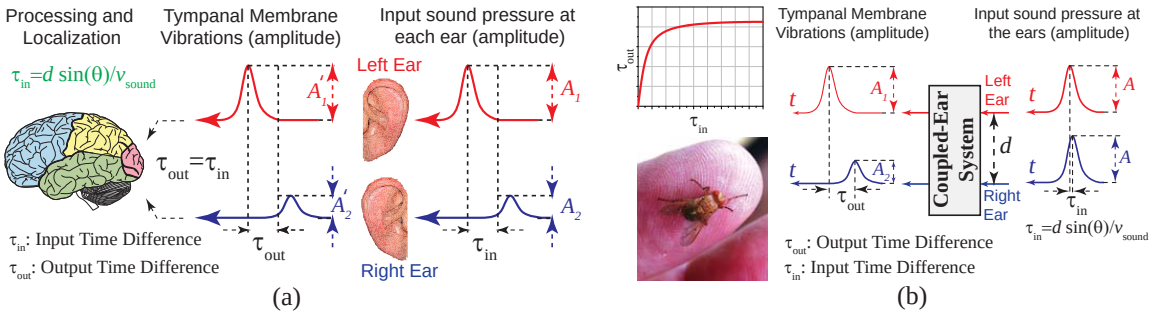

Figure 1.6 An illustrative view of mechanisms used for directional hearing in humans and insects. (a) Humans have directional hearing capability for sound frequencies in the range of 80 Hz - 20 kHz. The directional hearing capability in humans is aided by the large separation between the two ears (approximately 22-23 cm), the considerable scattering of sound caused by the large head that causes amplitude difference between the received signals, and a powerful brain which can accomplish sophisticated signal processing. (b) In insects such as *Ormia Ochracea*, none of these traits are present. To compensate for this disadvantage, such insects use a coupled-ear system, which enhances the contrast between the two received signals to make it easier for the brain of the animal to distinguish them. Photograph of *O. Ochracea* courtesy of Prof. W. Cade.

almost the same magnitude and a small time difference between them and converts them to two outputs that have a considerably larger contrast. The outputs of this system excite nerve pulses transmitted to the brain of the animal. Due to their larger contrast, it is easier for the brain of the animal to distinguish the differences between these signals as opposed to nerve pulses that would have been proportional to the pressure of the received sound wave had the insect been using isolated pressure receivers. Using such coupled ear systems, insects are able to determine the direction of arrival of sound sources of interest with extremely small receiving apertures. An example of an insect that possesses a hyperacute sense of directional hearing is the parasitoid fly *Ormia Ochracea* shown in Fig. 2.1(a). This insect has two ears that are separated from each other by about 1 mm and

can detect the DoA of a sound wave at $5\,$kHz with an angular resolution of $1^\circ - 2^\circ$ [44]-[45]. At $5\,$kHz the wavelength of sound is about $70\,$mm. While $5\,$kHz is the frequency of most interest to *O. Ochracea*, the fly has directional hearing capability over a broad frequency band ranging approximately from $4\,$kHz to $25\,$kHz [46].

O. Ochracea's super-resolving capabilities have been the source of inspiration for engineers in a number of different fields. Various research groups have worked on developing directional microphones based on the hearing mechanism of this insect [47]-[49]. More recently, the analogies between the auditory system of *O. Ochracea* and antenna arrays have been examined by two research groups [50]-[52]. In [50]-[51], we presented a prototype of a two-element electrically-small antenna array based on the hearing mechanism of this insect. Using theoretical analysis verified by measurement results, we demonstrated that such antenna arrays show enhanced directional sensitivity compared to regular antenna arrays that occupy the same aperture dimensions. Independent of our work, another research group reported a different idea for designing antenna arrays based on the directional hearing mechanism of *O. Ochracea* at about the same time [52]. The authors of [52] suggest that such antenna arrays provide higher directivity values compared to regular arrays with the same aperture size. While these works both examine the same physical concept, their conclusions are different. In particular, unlike the conclusions of [52], our theoretical analysis shows that passive antenna arrays that directly mimic the sense of directional hearing of *O. Ochracea* do not offer an enhanced directivity compared to a regular array of the same size.

Similar to the system shown in Fig. 1.6(b), a two-element biomimetic antenna array (BMAA) of the type reported in [51] takes two signals with the same magnitude and a small phase difference between them and converts them to two output signals that have a considerably larger phase difference between them. The relationship between the input and output phase differences of the system (Φ_{in} and Φ_{out}) can be expressed with a nonlinear,

one-to-one function (e.g., see the inset of Fig. 1.6(b)). This phase enhancement, however, is achieved at the expense of sacrificing the output power of the array along the direction of maximum sensitivity (i.e., the direction where maximum variation of Φ_{out} with respect to Φ_{in} occurs). This angle-of-incidence- (AoI-) dependent amplitude variation indicates that the large contrast between the input and output time differences of the coupled ear system of an insect (τ_i and τ_{out} in Fig. 1.6(b)) is obtained at the expense of sacrificing the range of the system[1]. Thus, we believe that insects with directional hearing capabilities have traded the capability of hearing sounds over large distances in favor of the capability of being able to localize the sound sources of interest in a smaller region. The goal of the current thesis is to investigate the trade-offs involved in the design of biomimetic antenna arrays and characterize their performance.

1.4 Thesis overview

The thesis is organized as follows:

1.4.1 Chapter 2: Biomimetic Antenna Arrays Based on the Directional Hearing Mechanism of the Parasitoid Fly *Ormia Ochracea*

We present a thorough examination of two-element antenna arrays that mimic the sense of directional hearing of the parasitoid fly *Ormia Ochracea* and examine the design trade-offs of such arrays. Recently, it was demonstrated that these antenna arrays demonstrate enhanced sensitivity to the direction of incidence of an electromagnetic wave, compared to regular arrays occupying the same aperture. This, however, comes at the expense of

[1]The directivity of a passive two-element antenna array that mimics the sense of directional hearing of *O. Ochracea* is not larger than that of a regular two-element antenna array as a result of this AoI-dependent amplitude variation. This can be observed by coherently adding the output signals of a BMAA specified by equations (1) and (2) of [51] and observing that the resulting function represents the array factor of a conventional antenna array.

sacrificing the available power at the outputs of such arrays. In this chapter, we present a model for these two-element biomimetic antenna arrays (BMAAs) that takes the mutual coupling effects into account. Using this model, we examine the tradeoffs that exist between the phase enhancement, which can be achieved from these arrays, and their output power levels. We demonstrate that for any given desired phase enhancement factor, an optimum BMAA design exists that maximizes the output power level of the array. We also show that strong mutual coupling between the two antennas can be exploited to enhance the output power of the array. A method for designing practical two-element BMAAs is also presented along with simulation and measurement results of a fabricated prototype.

1.4.2 Chapter 3: An Improved Architecture for Two-Element Biomimetic Antenna Arrays

A new architecture is presented for two-element biomimetic antenna arrays (BMAAs) that mimic the sense of directional hearing of the parasitoid fly *Ormia Ochracea*. The proposed architecture addresses a major practical shortcoming of the previously reported design in this area, namely the use of lossy transformers at high RF/microwave frequencies. The new topology does not employ any RF transformers and results in a substantially higher output power level for a given phase sensitivity, compared to the previously proposed design. Moreover, because the new design does not use any transformers, it is expected to be more amenable to operation at higher RF/microwave frequencies. A noise analysis is also conducted and the output signal-to-noise ratio (SNR) of the proposed design is theoretically compared with that of the previously reported design. It is shown that, for the same system level performance indicators, the proposed design demonstrates a higher SNR compared to the previous one. A prototype of a two-element biomimetic antenna array exploiting the proposed coupling network is designed, fabricated, and experimentally characterized.

1.4.3 Chapter 4: Architecture, Design, and Nonlinear Optimization of Three-Element Biomimetic Antenna Arrays

The architecture, design, and nonlinear optimization process of a three-element biomimetic antenna array (BMAA) are presented and discussed. The array is composed of three $\lambda/4$ monopoles with an element spacing of $\lambda/20$. The optimization process is based on choosing the desired phase enhancement factor and output power level of the side elements and maximizing the output power of the center element. A design example in conjunction with numerical simulations and optimization are presented to illustrate the design and principles of operation of the proposed array. The new array architecture addresses some of the shortcomings of the previously reported two-element BMAAs and its architecture can be readily extended to arrays with more than three elements.

1.4.4 Chapter 5: A Two-Element Biomimetic Antenna Array with Enhanced Angular Resolution and Optimized Power Extraction

A new architecture for a two element biomimetic antenna array (BMAA) is presented. This two-element BMAA is in the form of a coupled antenna array with an external coupling network that is designed to efficiently extract power from both linearly-independent modes of excitation of the array. These include the common mode and the differential modes of excitation. This new array offers an enhanced phase response compared to the regular antenna array that occupies the same aperture. However, unlike previous BMAA designs, the output power of the array does not need to be sacrificed to achieve this phase enhancement factor. Compared to a regular array, this two-element coupled array extracts the same amount of power from an incoming electromagnetic wave but provides a considerably larger phase sensitivity. The chapter describes the theory of operation and the design process of this antenna. Using the design procedure presented in this chapter, a

prototype of such a two-element BMAA is designed and and experimentally characterized in the lab. Measurement results confirm the advantages of this new design compared to the previous BMAAs reported in the literature.

1.4.5 Chapter 6: Bandwidth Enhancement of Biomimetic Antenna Arrays using Non-Foster Coupling Networks

In this chapter the bandwidth of biomimetic antenna arrays has been considerably improved by using non-Foster elements in their external coupling network. The proposed non-Foster design is compared to a passive design of the same phase enhancement factor and output power level. It is demonstrated that the non-Foster design improves the phase enhancement factor bandwidth by a factor of roughly 33. A practical implementation of the non-Foster coupling network using transistors is also discussed and the results compared with its ideal circuit element counterpart.

1.4.6 Chapter 7: Biomimetic Nano-Antenna Arrays: A Concept for Designing Sub-Wavelength Angle-Sensing Detectors at Optical Wavelengths

In this chapter, the concept of a two-element biomimetic antenna array is extended to optical frequencies and a new design for a two-element nano-antenna array that can act as a sub-wavelength angle-sensing optical detector is presented. The main feature of the proposed sub-wavelength detector is that it can be used to perform angle sensing without the need to perform coherent measurements at optical frequencies. This is particularly important at infrared and optical frequencies where conducting phase coherent measurement is challenging. The principles of operation of the new nano-antenna array along with the design and simulation results of a prototype are presented and discussed in this chapter.

Chapter 2

Biomimetic Antenna Arrays Based on the Directional Hearing Mechanism of the Parasitoid Fly *Ormia Ochracea*

2.1 Introduction

In this section, we present a thorough examination of two-element antenna arrays that mimic the sense of directional hearing of *O. Ochracea*. The antennas considered in this work are not electrically-small. They, however, are closely spaced and the mutual coupling between them is very strong. We present a model for these two-element BMAAs that takes the mutual coupling effects into account. Using this model, we theoretically examine the tradeoffs that exist between the phase enhancement factor and the output power level of these antennas. We demonstrate that for any given desired phase enhancement factor, an optimum BMAA design exists that maximizes the output power level of the array. We also show that mutual coupling between the two antennas can be beneficial in enhancing the output power level of the array. Additionally, we examine the impact of using non-ideal transformers on the performance of such arrays and present a method for designing two-element BMAAs that use nonideal transformers. Finally, we present the measurement results of a two-element BMAA designed using the proposed design procedure and experimentally validate the theoretical analyses presented in this section.

2.2 Theory

In this subsection, we analyze a two-element biomimetic antenna array composed of two closely-spaced antennas with a potentially strong mutual coupling between them. Through this analysis, we will derive the conditions required to achieve maximum output power from such an antenna with a given desired output phase response. Fig. 2.1(b) shows the block diagram of a two-element BMAA composed of two omnidirectional receiving antennas. The two antennas are separated by a distance of $d \ll \lambda$ from each other. A plane wave with an incidence angle of θ is incident on the two antennas, where θ is measured from the boresight direction. The outputs of the antennas ($x_1,\ x_2$) are fed to the two inputs of an external coupling network. The external coupling network is a four-port network with two inputs and two outputs. It takes two input signals, x_1 and x_2, with roughly the same amplitudes and a small phase difference of $\Phi_{in}(\theta)$ between them and converts them to two output signals, y_1 and y_2, with a considerably larger phase difference of $\Phi_{out}(\theta)$. Here, $\Phi_{in}(\theta) = \angle x_2 - \angle x_1$ and $\Phi_{out}(\theta) = \angle y_2 - \angle y_1$ as shown in Fig. 2.1(b) [51]. The external coupling network is implemented using a passive RLC circuit as shown in Fig. 2.1(c) [51]. Comparison of the coupling network used in the present work and the original coupling network reported in Fig. 2(d) of [51] shows some important modifications done in the new design. These changes, which add more flexibility to our design, are summarized as follows: 1) The present coupling network is assumed to be lossless (i.e., $R_c = 0$ in Fig. 2(d) of [51]). 2) The coupling capacitor C_c used in [51] is replaced with the impedance $jX_2/2$ to accommodate the possibility of implementation by an inductor. 3) Dependent voltage sources have been added to take the effect of mutual coupling into account. Furthermore, in this paper the effect of the impedance seen at the inputs of the transformers have also been considered. As discussed in [51], the relationship between $\Phi_{out}(\theta)$ and $\Phi_{in}(\theta)$ can be quantified using a nonlinear one-to-one function and for small

θ values, $\Phi_{out}(\theta) \gg \Phi_{in}(\theta)$. The two closely-spaced receiving antennas in this structure are represented by their Z parameters as shown in Fig. 2.1(c) [53]-[54]. Here, the antennas are represented by their self and mutual impedances and:

$$Z_s = R_s + jX_s \tag{2.1a}$$

$$Z_{12} = R_{12} + jX_{12}\ . \tag{2.1b}$$

$R_s(X_s)$ is the real (imaginary) part of the self impedance of the antennas and $R_{12}(X_{12})$ is the real (imaginary) part of the mutual impedance between the two antennas. The two antennas are assumed to be identical and their outputs are connected to the passive external coupling network comprised of transformers and reactances shown in Fig. 2.1(c). The two outputs of the BMAA, which are outputs of the external coupling network, are connected to $50\,\Omega$ loads.

In this theoretical analysis, we assume that the open circuit voltages of the two antennas have equal magnitudes and a phase difference of 2α. Additionally, we assume that the transformers used in the external coupling network are ideal transformers. Under these assumptions, we can convert the equivalent circuit model shown in Fig. 2.1(c) to the circuit shown in Fig. 2.2(a). Here, $R_L = \frac{50\,\Omega}{n^2}$ and α is assumed to be $\pi \frac{d}{\lambda} \sin(\theta)$. Note that (for small θ values around zero) α may be slightly different from this value if the mutual coupling between the elements is strong. This, however, does not impact the validity of the presented design procedure. In this figure, the two receiving antennas are modeled with their Thevenin equivalent circuit models and each voltage source represents the normalized open circuit voltage of each antenna. The circuit shown in Fig. 2.2(a) can be analyzed by dividing it into an even-mode circuit and an odd-mode circuit as shown in Figs. 2.2(b) and 2.2(c) respectively. From symmetry (anti-symmetry) of the structure shown in Fig. 2.2(b)

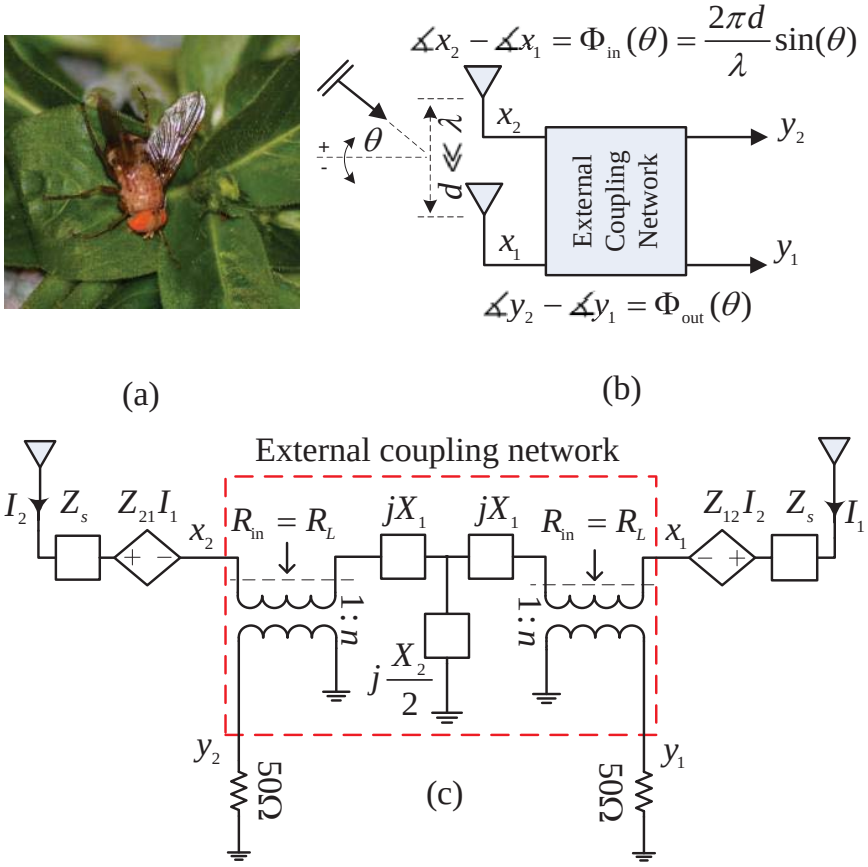

Figure 2.1 (a) Photograph of the parasitoid fly *Ormia Ochracea* (courtesy of Prof. William Cade). (b) Block diagram of a two-element biomimetic antenna array. (c) Equivalent circuit model of a two-element biomimetic antenna array taking into account the mutual coupling effects between the two antennas.

(Fig. 2.2(c)), we can see that:

$$I_{1,c} = I_{2,c} = I_c \tag{2.2a}$$

$$-I_{1,d} = I_{2,d} = I_d \tag{2.2b}$$

The total currents, I_1 and I_2, can be obtained from the following equations:

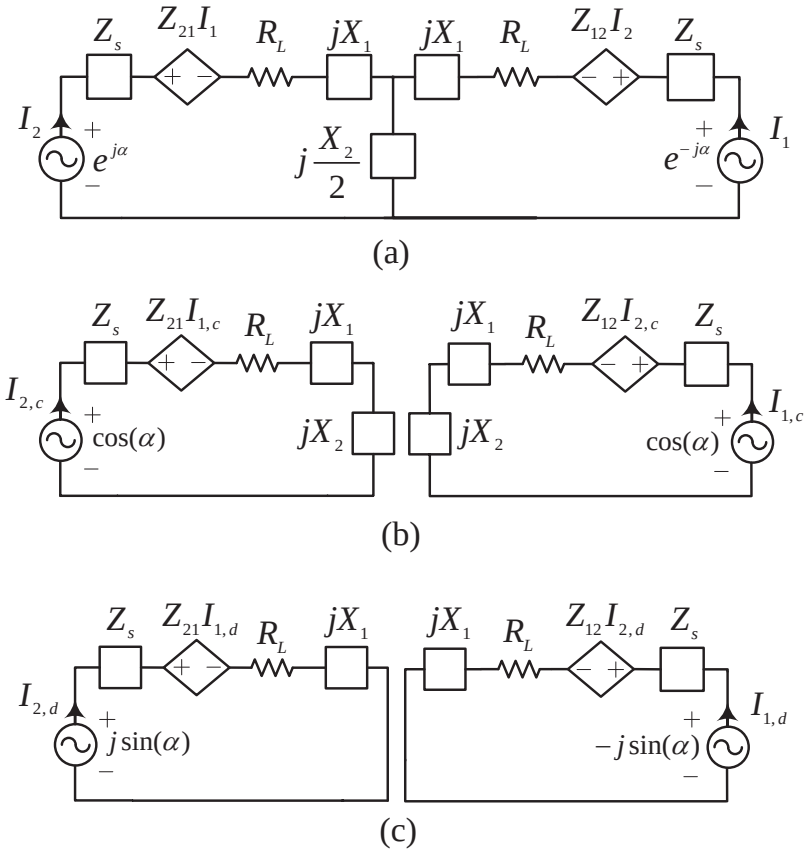

Figure 2.2 (a) Equivalent circuit model of the two-element biomimetic antenna array shown in Fig. 2.1. (b) The common-mode circuit. (c) The differential-mode circuit.

$$I_1 = I_c - I_d \tag{2.3a}$$

$$I_2 = I_c + I_d \tag{2.3b}$$

Using the equivalent circuit models shown in Figs. 2.2(b) and 2.2(c) in conjunction with the relationships given in (2.3a)-(2.3b), we can obtain closed-form expressions for I_1 and

I_2 as:

$$I_1 = \frac{\cos(\alpha)}{(R+R_{12})+jb} - j\frac{\sin(\alpha)}{(R-R_{12})+ja} \tag{2.4a}$$

$$I_2 = \frac{\cos(\alpha)}{(R+R_{12})+jb} + j\frac{\sin(\alpha)}{(R-R_{12})+ja} \tag{2.4b}$$

where

$$R = R_L + R_s \tag{2.5a}$$

$$a = X_1 + X_s - X_{12} \tag{2.5b}$$

$$b = X_1 + X_2 + X_s + X_{12} \tag{2.5c}$$

For incidence angles close to the boresight, i.e. $\theta \approx 0^\circ$, we can use the Taylor series expansion for the sine and cosine functions in (2.4a) and (2.4b) to arrive at:

$$I_1 \approx \frac{1}{(R+R_{12})+jb} - j\frac{\alpha}{(R-R_{12})+ja} \tag{2.6a}$$

$$I_2 \approx \frac{1}{(R+R_{12})+jb} + j\frac{\alpha}{(R-R_{12})+ja}. \tag{2.6b}$$

At boresight, the output power at both ports are the same and are given by:

$$\begin{aligned} P_{out} &= \frac{1}{2}R_L|I_1|^2\Big|_{\theta=0} = \frac{1}{2}R_L|I_2|^2\Big|_{\theta=0} \\ &= \frac{1}{2}(R-R_s)\left|\frac{1}{(R+R_{12})+jb}\right|^2 \\ &= \frac{1}{2}(R-R_s)\frac{1}{(R+R_{12})^2+b^2}. \end{aligned} \tag{2.7}$$

To find a condition for P_{out} that yields realizable values of R and b, we rearrange (2.7) for b^2 and get:

$$b^2 = -R^2 + \left(\frac{1}{2P_{out}} - 2R_{12}\right)R - \left(\frac{R_s}{2P_{out}} + R_{12}^2\right). \tag{2.8}$$

b^2 is a real nonnegative quantity. Thus we must have:

$$-R^2 + \left(\frac{1}{2P_{out}} - 2R_{12}\right) R - \left(\frac{R_s}{2P_{out}} + R_{12}^2\right) \geq 0. \tag{2.9}$$

The left hand side of (2.9) is a quadratic function of the independent variable R. Due to the negative leading term, the quadratic function graphically represents a concave down parabola. To ensure that the quadratic function has nonnegative values, its discriminant should be nonnegative, i.e.

$$\Delta_1 = \left(\frac{1}{2P_{out}} - 2R_{12}\right)^2 - 4\left(\frac{R_s}{2P_{out}} + R_{12}^2\right) \geq 0. \tag{2.10}$$

By rearranging, we arrive at the following necessary condition for the output power:

$$P_{out} \leq \frac{1}{8(R_s + R_{12})} \triangleq P_0\,. \tag{2.11}$$

It is easy to verify that P_0 in (2.11) is simply the available power that can be obtained from each antenna. Thus, for P_{out} values that are less than P_0, real values for R and b can be found.

The "output phase" (i.e., the phase difference between the two outputs of the BMAA), is equal to the phase difference between I_2 and I_1. The ratio of I_2 to I_1 can be written as:

$$\frac{I_2}{I_1} = \frac{1 + j\alpha\frac{(R+R_{12})+jb}{(R-R_{12})+ja}}{1 - j\alpha\frac{(R+R_{12})+jb}{(R-R_{12})+ja}} = \frac{1+j\alpha z}{1-j\alpha z} \tag{2.12}$$

where

$$z = \frac{(R+R_{12})+jb}{(R-R_{12})+ja} = \eta + j\xi \tag{2.13}$$

$$\eta = Re(z) = \frac{(R^2 - R_{12}^2) + ab}{(R-R_{12})^2 + a^2}\,. \tag{2.14}$$

Thus,

$$\begin{aligned}\Phi_{out}(\theta) &= \angle I_2 - \angle I_1 = \angle(I_2/I_1) \\ &= \tan^{-1}(\frac{\alpha\eta}{1-\alpha\xi}) + \tan^{-1}(\frac{\alpha\eta}{1+\alpha\xi}) \\ &= \tan^{-1}(\frac{2\alpha\eta}{1-\alpha^2(\eta^2+\xi^2)}).\end{aligned} \tag{2.15}$$

At boresight, the slope of the output phase with respect to θ is:

$$s = \left.\frac{d\Phi_{out}}{d\theta}\right|_{\theta=0} = \left(\left.\frac{d\Phi_{out}}{d\alpha}\right|_{\alpha=0}\right)\left(\left.\frac{d\alpha}{d\theta}\right|_{\theta=0}\right) = 2\eta\pi\frac{d}{\lambda}\,. \tag{2.16}$$

The external coupling network is designed to enhance the phase difference between the two output signals of the BMAA compared to that of its two input signals. The phase difference between two isotropic antennas located at a distance of d from each other and illuminated by an incident plane EM wave from an angle of θ with respect to the boresight is $kd\sin(\theta)$ where $k = \frac{2\pi}{\lambda}$ is the free space wavenumber. At boresight, the slope of this phase difference, with respect to the incidence angle, is:

$$s_0 = \left.\frac{d}{d\theta}\left(2\pi\frac{d}{\lambda}\sin(\theta)\right)\right|_{\theta=0} = 2\pi\frac{d}{\lambda}\,. \tag{2.17}$$

Thus, $\eta = \frac{s}{s_0}$ is a measure that can be used to quantify the phase enhancement capabilities of a two-element BMAA. In the remainder of this work η will be referred to as the "phase enhancement factor". As demonstrated in [51], a two-element BMAA can have phase enhancement factors significantly larger than one (i.e., $\eta \gg 1$). This means that the phase difference between the two output signals of a BMAA (y_2 and y_1 in Fig. 2.1) is larger than what is normally achieved using an ideal antenna array composed of two isotropic receivers with the same separation. This, however, comes at the expense of sacrificing the output power level of the antenna [51]. In general, as η is increased, the output power that is available at the output of a two-element BMAA decreases. Our goal in

this work is to quantitatively examine this tradeoff and determine the maximum available output power that can be achieved for a given desired phase enhancement factor. Since the minimum power level occurs for angles where η is maximum (i.e. close to the boresight), we define the maximum power that is available from a BMAA output at boresight as P_{out}^{max}.

Rearranging (2.14), we have:

$$\eta a^2 - ab + \eta(R - R_{12})^2 - (R^2 - R_{12}^2) = 0\ . \tag{2.18}$$

This is a quadratic equation with respect to a. Since a is a real quantity, the discriminant of (2.18) should be non-negative to ensure that (2.18) can be satisfied. Therefore, we have:

$$\Delta_2 = b^2 - 4\eta\Big[\eta(R - R_{12})^2 - (R^2 - R_{12}^2)\Big] \geq 0. \tag{2.19}$$

using (2.8) we can rewrite (2.19) as:

$$\begin{aligned}(2\eta - 1)^2 R^2 - \left(\frac{1}{2P_{out}} + 2R_{12}(4\eta^2 - 1)\right) R \\ + \left((2\eta + 1)^2 R_{12}^2 + \frac{R_s}{2P_{out}}\right) \leq 0\ .\end{aligned} \tag{2.20}$$

The left hand side of (2.20) is a quadratic function of R that graphically represents a concave up parabola (positive leading term). To ensure that (2.18) can be satisfied, at least one real value of R must exist that satisfies (2.20). Thus, if the quadratic function on the left hand side of (2.20) has real roots (as a function of R), real value(s) of R that satisfy (2.20) will exist. Thus, (2.20) can only be satisfied if the discriminant of the quadratic function is non-negative, i.e.:

$$\begin{aligned}\Delta_3 = \left(\frac{1}{2P_{out}} + 2R_{12}(4\eta^2 - 1)\right)^2 \\ - 4(2\eta - 1)^2 \left((2\eta + 1)^2 R_{12}^2 + \frac{R_s}{2P_{out}}\right) \geq 0\ .\end{aligned} \tag{2.21}$$

By rearranging, we arrive at the following necessary condition for the output power:

$$\frac{1}{P_{out}} \geq 8R_s(2\eta-1)^2\left(1-(\frac{2\eta+1}{2\eta-1})\frac{R_{12}}{R_s}\right). \tag{2.22}$$

For a given pair of phase enhancement factor and desired output power level (η, P_{out}) values, conditions specified by (2.11) and (2.22) are *necessary* conditions for the existence of a realizable external coupling network[1]. If these conditions are not satisfied, real values for X_1 and X_2 and a real positive value for R_L can not be found. However, the *sufficient* condition for obtaining a realizable external coupling network for a given pair of (η, P_{out}) values is the existence of a real value of $R > R_s$ that satisfies both (2.9) and (2.20) simultaneously. Conditions (2.11) and (2.22) simply state that there are real values for R that satisfy inequalities (2.9) and (2.20), respectively. However these values for R might not overlap, in which case the external coupling network will not be realizable. For any given P_{out} value, a maximum phase enhancement factor (denoted by η_{max}) exist where for $\eta > \eta_{max}$, no value of R exists that can simultaneously satisfy (2.9) and (2.20). Under these circumstances, the BMAA can not be physically realized. For $\eta < \eta_{max}$, a range of values for R can be found that satisfy (2.9) and (2.20). Using any value of R within this range, a and b can be obtained using (2.8) and (2.18). The circuit values for the external coupling network can then be found using (2.5a)-(2.5c) and the coupling network is therefore determined. It is noted that different values of R within the overlap range result in different coupling networks. However, all these alternative networks provide the same combination of P_{out} and η values at bore-sight. For $\eta = \eta_{max}$, the range of R values that satisfy (2.9) and (2.20) is reduced to a single value and only one possible coupling network exists that results in the desired P_{out} and η combination.

[1]Notice that (2.11) is a condition derived by analyzing the output power of the system and (2.22) is a condition derived by analyzing the phase enhancement factor. Under certain circumstances (e.g., strong mutual coupling), the upper bound specified by (2.22) is higher than that of (2.11).

2.3 Design of Optimized BMAAs

2.3.1 BMAA Design Using Ideal Transformers

First, we examine design of an optimized two-element BMAA that uses lossless ideal transformers. This procedure is demonstrated through a design example. The two-element array, considered in this example, is composed of two $13.5\,\text{cm}$ long monopole antennas separated from one another by a distance of $2.5\,\text{cm}$. At the operating frequency of $600\,\text{MHz}$, each monopole is slightly larger than $\lambda_0/4$ and the spacing between the two antennas is $0.05\lambda_0$. The two antennas are assumed to be mounted on a common ground plane with infinite dimensions. Since the antennas are closely spaced and operate close to their resonant frequencies, the mutual coupling between them is very strong. This structure is simulated in CST Microwave Studio and the two-port Z-parameters of the antennas, at the desired frequency of operation, are obtained and presented in Table 2.1.

Table 2.1 Calculated Z-parameters of the two monopole antenna system discussed in Section 2.3.1 at $600\,\text{MHz}$.

$R_s = \text{Re}(Z_{11})$	$42.36\,\Omega$
$R_{12} = \text{Re}(Z_{12})$	$40.57\,\Omega$
$X_s = \text{Im}(Z_{11})$	$0.79\,\Omega$
$X_{12} = \text{Im}(Z_{12})$	$-53.80\,\Omega$

In designing the optimum BMAA, the goal is to maximize the output power level for a given phase enhancement factor or to maximize the phase enhancement factor for a given output power level. In this subsection, we assume that the desired output power level of the optimized BMAA, normalized to the power that is available from a regular array at boresight, is known and design the structure to provide the maximum phase enhancement

factor. In all subsequent discussions, we assume that the power at the outputs of the BMAA is normalized to the available power at the output of the regular array when the antennas are connected to matched loads and the array is illuminated by a plane wave at boresight. It can be shown that this power is P_0 as defined in (2.11). For this design example, η_{max} has been calculated as a function of the normalized output power of the BMAA, P_{out}, using the following procedure. For a specific value of P_{out}, we obtain the roots of the left hand side of (2.9) and denote them by R_1 and R_2. This gives us the range of values for $R \in [R_1, R_2]$ which satisfy condition (2.9). For each value of R in this interval we obtain a maximum value of η that satisfies (2.20) and denote it by η^*. By plotting η^* as a function of R in the interval [R_1, R_2], the maximum value of this function is obtained and denoted by η_{max}. Fig. 3.2 is a plot of η_{max} as a function of P_{out} and shows the maximum phase enhancement factor that can be theoretically achieved for a given output power level[2]. Alternatively, Fig. 2.3 can be used to determine the maximum output power level achievable for a given η_{max}. For comparison, η_{max} has also been calculated for a hypothetical two-element BMAA in which the antenna elements have the same R_s =Re(Z_{11}) values but have no mutual coupling between them ($R_{12} = 0$) and the results are also presented in Fig. 2.3. The comparison between the two results presented in Fig. 2.3 shows that in a two-element BMAA the presence of mutual coupling can be exploited to enhance the output power level of the array.

As can be seen from Fig. 2.3, for an ideal coupling network and an arbitrarily chosen output power of $P_{out} = -12$ dB, the value of η_{max} is approximately equal to 27. Therefore, for this design example, we choose an output power level of $P_{out} = -12$ dB and a phase enhancement factor of $\eta = 25$. Notice that this value of η is below that of η_{max} for

[2]Notice that the maximum output power level that can be achieved from a two-element BMAA is the output power level when no coupling network is used and the antennas are impedance matched. Therefore, the maximum value of the normalized P_{out} in Fig. 2.3 is 0 dB

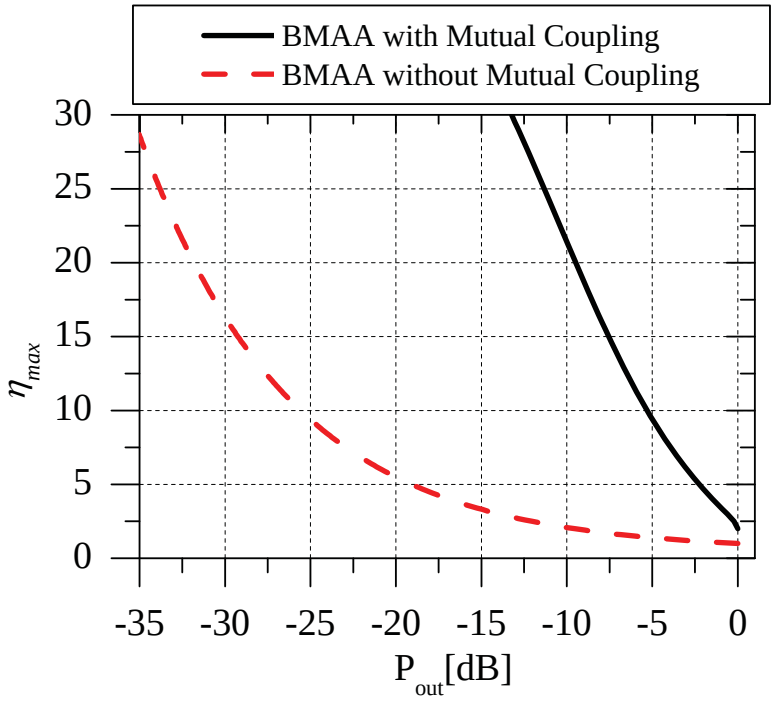

Figure 2.3 Variation of maximum phase enhancement factor as a function of output power for the two-element BMAA discussed in Subsection 2.3.1. The result for a hypothetical BMAA composed of two antennas that have the same values of $R_s = \mathrm{Re}(Z_{11})$ but have no mutual coupling between them, i.e., $R_{12} = 0$, is also shown for comparison.

the desired output power level. Therefore, as described in Subsection 2.2, more than one coupling network exists that results in this $(\eta,\ P_{out})$ combination. Following the theoretical analysis presented in Subsection 2.2, it can easily be shown that for these P_{out} and η values, any value of $R \in [43.75\,\Omega, 44.25\,\Omega]$ satisfies (2.9) and (2.20)[3]. This limited range of admissible R values is due to the close proximity of the selected η value to η_{max} for the given P_{out} value. Notice that as η gets closer to η_{max}, the range of admissible values for R becomes smaller and smaller until it reaches a single value for $\eta = \eta_{max}$.

[3]This can be shown by simply plotting the left hand sides of (2.9) and (2.20) as a function of R.

If we choose $R = 44\,\Omega$, using (2.8), the value of b is calculated to be $b = \pm 38.34$. If we arbitrarily choose the positive value for b, (2.18) can be used to calculate the value of a. Here, $a = 1.42$ or $a = 0.114$. By choosing $a = 1.42$ and using (2.5a)-(2.5c) in conjunction with the equivalent circuit values given in Table I, the element values of the external coupling network of the BMAA can be calculated as:

$$X_1 = -53.17\,\Omega \tag{2.23a}$$

$$X_2 = 144.52\,\Omega \tag{2.23b}$$

$$R_L = 1.64\,\Omega. \tag{2.23c}$$

The reactance values of X_1 and X_2 can be obtained using a $4.988\,$pF capacitor and a $19.17\,$nH inductor at $600\,$MHz. R_L can be realized by using an ideal transformer with a turn ratio of $n = \sqrt{50/1.64} \approx 5.52$ terminated at a $50\,\Omega$ load as shown in Fig. 2.1(c).

Table 2.2 The four possible implementations of the external coupling network of the BMAA examined in Section 2.3.1. At 600 MHz, the reactance value of X_1 is obtained using an inductor with an inductance of L and the reactance value of $X_2/2$ is obtained using a capacitor with a capacitance of C.

	C (pF)	L (nH)
Case 1	4.988	19.17
Case 2	4.869	19.34
Case 3	4.736	9.370
Case 4	4.849	9.200

For the specific value of $R = 44\,\Omega$ chosen in this design example, there are a total of four different circuits that result in the same η and P_{out} values. The element values of the other three circuits can be obtained by using different combinations of values obtained for

the variables a and b as discussed in the previous paragraph. Following the same procedure, the element values of these four coupling networks are calculated and the results are presented in Table 2.2. Notice that a different choice of R from the admissible values in the range of $[43.75\,\Omega, 44.25\,\Omega]$ results in a different set of a and b values, which will in turn result in a different set of coupling networks that provide the same combination of η and P_{out} values. Therefore, if the value of η is less than η_{max}, numerous different coupling networks exist that will result in given P_{out} and η values.

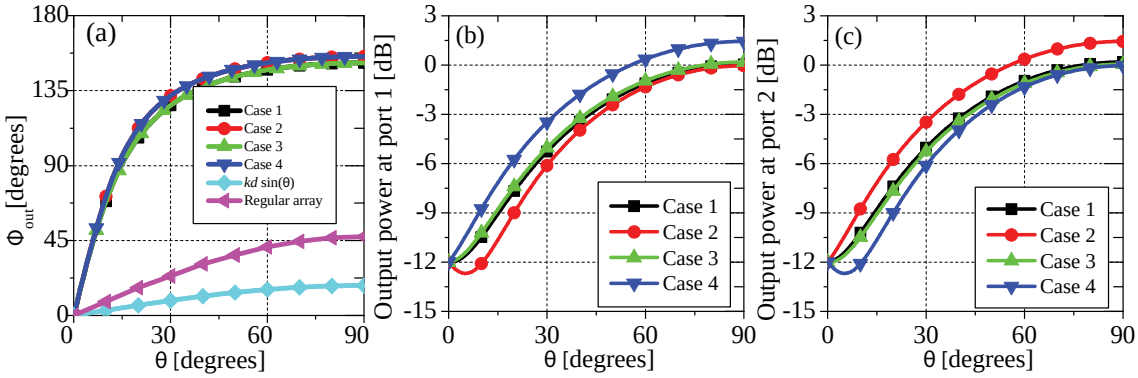

Figure 2.4 The simulated responses of the four biomimetic antenna arrays examined in Section 2.3.1. (a) The phase responses of the BMAAs employing the external coupling networks identified in Table 2.2. The output phase response of a regular array (the same antennas without the coupling network) has also been included. (b)-(c) The output power of these BMAAs as a function of angle of incidence of the EM wave. The output power values are normalized to P_0, which is the power available from a regular antenna array (A BMAA without coupling network) at boresight. See (2.11). (b) The output power at the contralateral output port. (c) The output power at the ipsilateral output port. The ipsilateral (contralateral) antenna is the one closer (further) from the incident EM wave.

To simulate the responses of these antennas, the Thevenin equivalent circuit model of the two antennas is used in a circuit simulation software, Agilent's Advanced Design System (ADS), in conjunction with the coupling networks whose parameters are provided in Tables 2.1 and 2.2. Using these circuit simulations, the output phase and amplitude

responses of each BMAA is calculated. The results of these simulations are presented in Fig. 2.4. Fig. 2.4(a) shows the output phase response (Φ_{out}) for each BMAA. Cases 1 to 4 refer to BMAAs with external coupling network parameters identified in Table 2.2. As a reference for comparison, $kd\sin(\theta)$, which is the phase difference between two uncoupled isotropic receiving antennas separated by a distance of d, is also plotted in this figure. As can be observed from this figure, all four BMAAs result in the same phase enhancement factor, which is defined to be the ratio of the slopes of their $\Phi_{out}(\theta)$ curves to the slope of the $kd\sin(\theta)$ curve at $\theta = 0^{\circ}$. More specifically, all four BMAAs offer a phase enhancement factor of $\eta = 25$ as expected. Fig. 2.4(a) also shows the phase difference between the two outputs of the regular antenna array, composed of the two closely-spaced monopoles without the external coupling network. As can be observed, this output phase difference is enhanced compared to $kd\sin(\theta)$. This phenomenon is a direct consequence of the strong mutual coupling between the two closely-spaced monopole antennas. Fig. 2.4(b) and 2.4(c) show the normalized output power of the BMAAs at each output port. As defined in Fig. 2.1, Port 1 is the output port that is further from the incident EM wave (the contralateral output) and Port 2 is the output port that is closer to the incident EM wave (the ipsilateral output). As can be observed from Figs. 2.4(b) and 2.4(c), all BMAAs provide the expected P_{out} value of -12 dB at boresight. While the different BMAAs provide the same η and P_{out} values at boresight, their responses are not identical to each other for other incidence angles. This stems from the fact that the design goals of the analysis procedure presented in Section 2.2 are to optimize the response of the BMAA along the direction of maximum sensitivity, i.e. $\theta \approx 0^{\circ}$, and the approximations used are most accurate for incidence angles in the vicinity of the boresight. Therefore, it is not unexpected to see differences in the output power level of the array at directions other than the boresight. Nonetheless, the results presented in Fig. 2.4 confirm the validity of the theoretical analysis presented in Section 2.2 for BMAAs that use ideal transformers.

2.3.2 Design of Optimized BMAAs With Nonideal Transformers

The design of a two-element BMAA using ideal transformers is rather straight forward and follows directly from the design procedure presented in the previous subsection. In practice, however, the transformers used at high frequencies are not ideal transformers and have losses associated with them. This impacts the performance of a two-element BMAA. In this subsection, we present a procedure that can be used to design BMAAs which use well-characterized, nonideal transformers. This design procedure is based on selecting a desired normalized output power level for the BMAA, P_{out}, and determining the parameters of the coupling network that result in maximum phase enhancement factor, η_{max}. In this subsection, we demonstrate this process using a design example. Similar to the previous case, the BMAA considered in this example is composed of two $13.5\,$cm monopole antennas, which are separated from each other by $2.5\,$cm and mounted on an infinite ground plane.

Fig. 2.5 shows the common and differential mode half circuits of the BMAA shown in Fig. 2.1(c). In this figure, $v_c(\theta)$ and $v_d(\theta)$ are the common mode and differential mode open-circuit antenna voltages and both are functions of the incidence angle. The values of $v_c(\theta)$ and $v_d(\theta)$ for various angles of incidence are obtained using full-wave electromagnetic simulations. To do this, the monopole array is simulated in CST Microwave studio by illuminating it with vertically polarized plane waves incident from various incidence angles along the azimuth plane and calculating the open circuited voltage at the terminals of the two antennas. The goal is to design the coupling network so that for $P_{out} \approx -12$ dB, the maximum possible phase enhancement factor is obtained. Before we calculate the component values of the coupling network (X_1 and X_2 in Figs. 2.1 and 2.5), we have to characterize the transformer used in the external coupling network. As seen in the previous subsection, for $P_{out} = -12\,$dB, the value of the transformer turn ratio that resulted

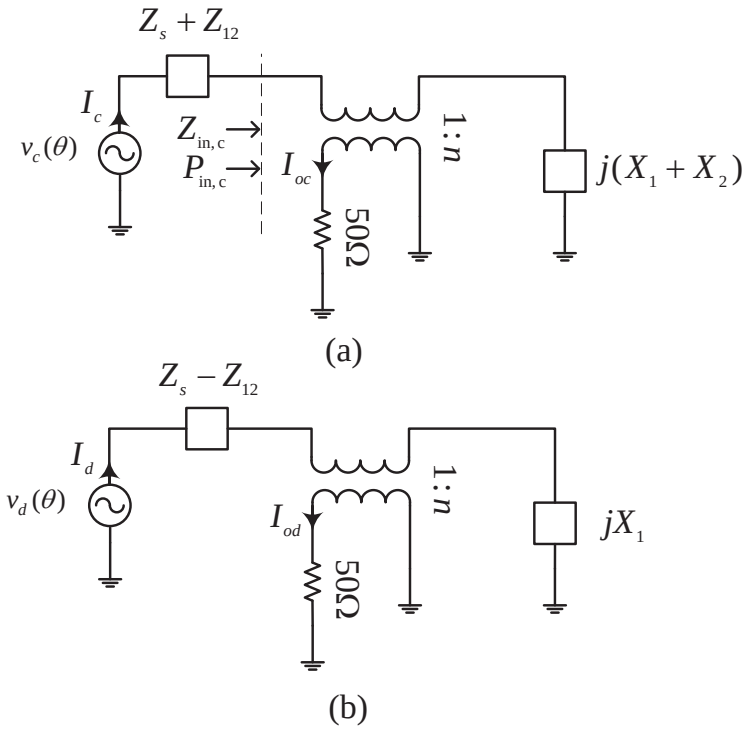

Figure 2.5 (a) The common mode half circuit of the BMAA. (b) The differential mode half circuit of the BMAA. Here, the transformer is assumed to be nonideal.

in the optimum coupling network was $n = 5.5$. In this design example, however, we use a transformer manufactured by Coilcraft (model number Z9314-AL) with a turn ratio of $n = 2.5$. This choice was motivated by practical concerns, since a low loss transformer with a turn ratio of 5.5 that could operate at $600\,\text{MHz}$ was not readily available to us. The four-port S-parameters of the transformer are measured using a four-port vector network analyzer (VNA) and its Z-parameters are calculated from the measured data. The measured Z-parameters of the transformer are then used in the design process.

The remainder of the design process consists of determining the values of the remaining elements used in the external coupling network. These are the two reactances X_1 and

X_2 as shown in Fig. 2.5. First, we calculate $X_1 + X_2$. At boresight ($\theta = 0°$), $v_d = 0$. Therefore, the output power of the BMAA at boresight can be calculated by only using the common mode circuit. As can be seen from Fig. 2.5(a), in this case the output power is only a function of $X_1 + X_2$ (and not on the values of X_1 and X_2 individually). Since we have assumed that these reactive components are lossless, part of the power entering the coupling network (denoted by $P_{in,\,c}$ in Fig. 2.5(a)) is delivered to the $50\,\Omega$ load and the rest is lost in the transformer. While the exact value of the transformer loss depends on the unknown value of $X_1 + X_2$, the variation of transformer loss with respect to $X_1 + X_2$ is negligible and it is found to be between 1.5 to $2\,$dB[4]. Therefore, we take the power entering the coupling network to be $P_{in} = -10\,$dB to ensure that P_{out} is in the range of $-12\,\text{dB} < P_{out} < -11.5\,\text{dB}$. Using Fig. 2.5(a) and basic circuit analysis techniques, it can be shown that the locus of points on the complex $Z_{in,\,c}$ plane that result in a constant $P_{in,\,c}$ value is a circle. A section of this circle, which corresponds to $P_{in,\,c} = -10$ dB, is shown with a dashed line in Fig. 2.6. Moreover, as $X_1 + X_2$ takes on real values from $-\infty$ to $+\infty$, $Z_{in,\,c}$ is calculated using ADS circuit simulator and the measured Z-parameters of the transformer and is found to map the curve shown with a solid line in Fig. 2.6. As can be observed, the two curves cross at the value of $Z_{in,\,c} \approx 9.9 - j102\,\Omega$. This means that there is a real value of $X_1 + X_2$ that results in an input power of $P_{in,\,c} = -10$ dB. By plotting the real and imaginary parts of the input impedance, $Z_{in,\,c}$, as a function of $X_1 + X_2$ (as shown in Fig. 2.7), we can easily see that $X_1 + X_2 = 131\,\Omega$ realizes this input impedance. For this value of $X_1 + X_2$, the value of the transformer loss is equal to $1.6\,$dB. Thus, the output power level of the BMAA, at boresight, is expected to be equal to

[4]This is done by simulating the circuit shown in Fig. 2.5(a) in ADS where the values of $X_1 + X_2$ are changed from $-\infty$ to $+\infty$ and the transformer loss is calculated. In doing this, the measured S-parameters of the transformer are used.

$P_{out} = -11.6$ dB. The common mode output current, I_{oc}, is then calculated as a function of angle-of-incidence (θ) using this reactance.

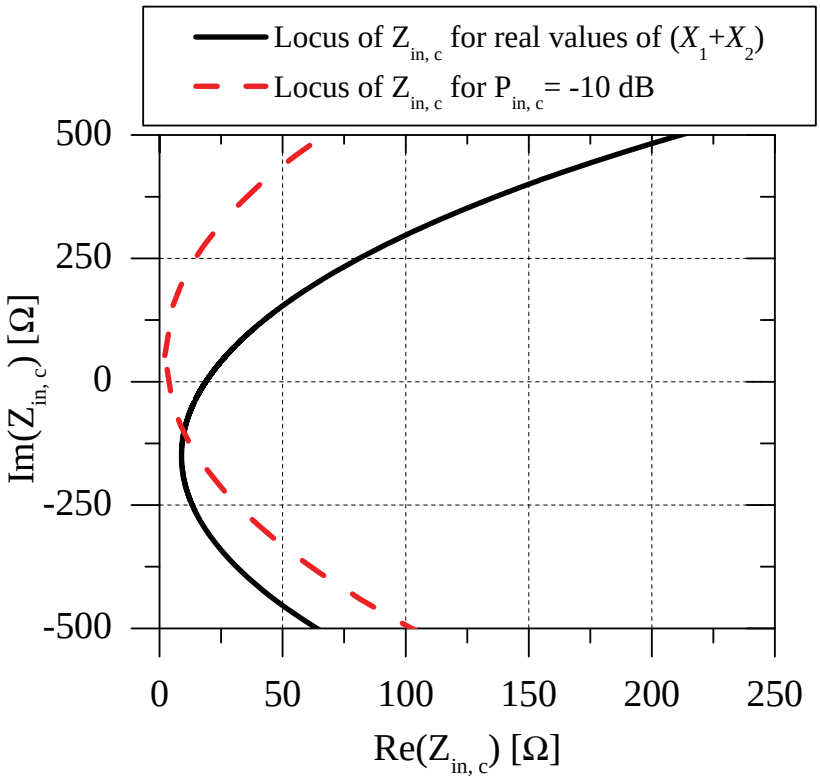

Figure 2.6 Locus of $Z_{in,\,c}$ as $X_1 + X_2$ varies from $-\infty$ to $+\infty$ and for constant input power to the external coupling network of $P_{in,\,c} = -10$ dB.

Now that the value of $X_1 + X_2$ is determined, by determining the value of X_1, all of the parameters of the external coupling network can be identified. To do this, I_{od} is calculated as a function of X_1 using the equivalent circuit shown in Fig. 2.5(b). Subsequently, η is calculated from:

$$\eta = \frac{1}{\frac{2\pi d}{\lambda}} \frac{d\Phi_{out}}{d\theta}\bigg|_{\theta=0} = \frac{1}{\frac{2\pi d}{\lambda}} \frac{d}{d\theta}\left(\angle \frac{I_{oc} + I_{od}}{I_{oc} - I_{od}}\right)\bigg|_{\theta=0} \tag{2.24}$$

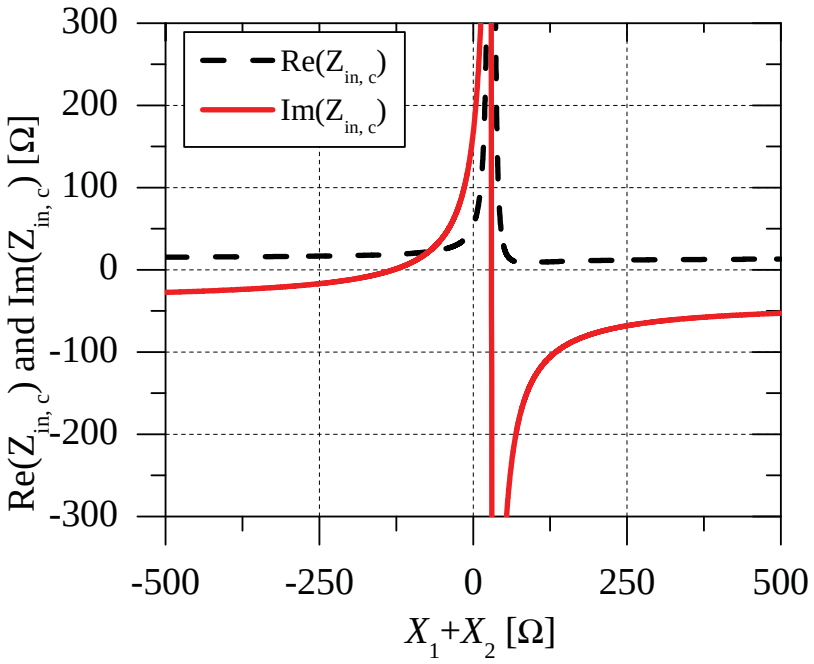

Figure 2.7 The real and imaginary parts of $Z_{in,c}$ as a function of $X_1 + X_2$.

as a function of X_1. Here Φ_{out} is the phase difference between the outputs of the BMAA and $2\pi\frac{d}{\lambda}$ is the slope of the function $kd\sin(\theta)$ at $\theta = 0°$. Fig. 2.8 shows the variations of $|\eta|$ as a function of X_1. As can be seen, the maximum value of phase enhancement factor is approximately equal to 16.8. Choosing $X_1 = 350\,\Omega$ results in a phase enhancement factor of $\eta \approx 15$. Using this value of X_1, we can calculate $X_2 = 131\,\Omega - 350\,\Omega = -219\,\Omega$. Using these X_1 and X_2 values, the values of the lumped element components that constitute the external coupling network of this BMAA can be determined. At $600\,$MHz, X_1 can be implemented using an inductor with an inductance value of $92.84\,$nH and X_2 can be implemented using a capacitor with a capacitance of $2.42\,$pF.

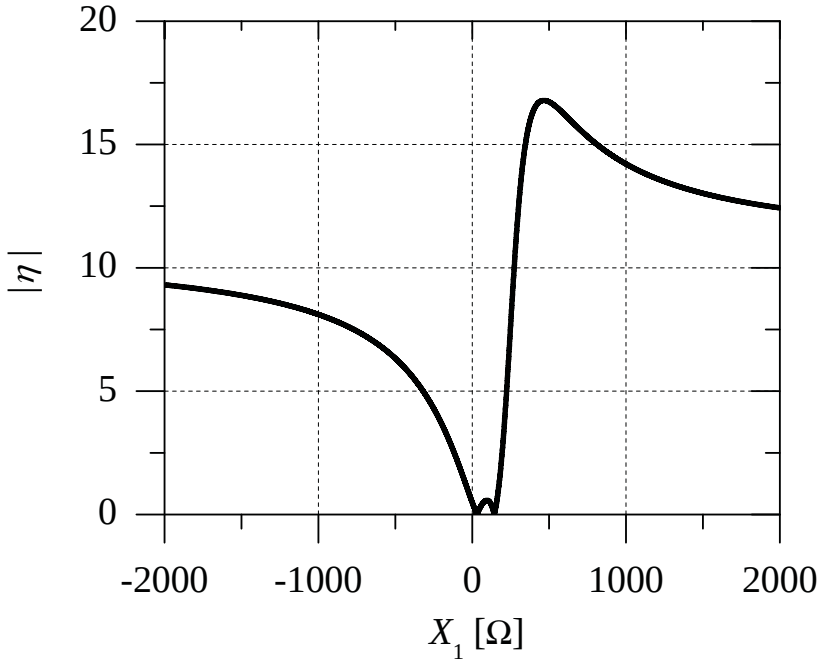

Figure 2.8 Variation of $|\eta|$ as a function of X_1 for a coupling network that results in $P_{out} \approx -12$ dB.

2.4 Experimental Verification

The optimized BMAA discussed in Section 2.3.2 and its associated coupling network are fabricated as shown in Fig. 2.9. The two monopole antennas are made out of hollow copper tubes with a circular cross section with inner and outer radii of 1.8 mm and 2.4 mm respectively. The antennas are mounted on a brass ground plane with physical dimensions of 60 cm $\times$ 60 cm as shown in Fig. 2.9(a). The monopole antennas are fed using SMA connectors mounted underneath the ground plane. The external coupling network is fabricated on a separate dielectric substrate as is shown in Fig. 2.9(b). Two Z9314-AL transformers (from Coilcraft), two 82 nH inductors, and a 2.7 pF capacitor are used to implement the external coupling network. The inductors had a tolerance of 2% and a quality factor of

$Q \approx 60$ at 600 MHz. The capacitors had a tolerance of ± 0.1 pF and a quality factor of $Q \approx 1000$ at 600 MHz. The input ports of the external coupling network are connected to the SMA connectors that feed the two monopole antennas and the outputs of the BMAA are taken from the two outputs of the external coupling network as shown in Fig. 2.9(b). The response of the BMAA is measured by illuminating it with plane waves arriving from different directions. Measurements are conducted using three ports of a four-port VNA. One of the VNA ports is connected to a dipole antenna operating at 600 MHz, which is used to illuminate the BMAA. The two other VNA ports are connected to the two BMAA outputs and the complete S-parameters of this three-port system are measured for various incidence angles. To minimize the impact of the scattering and diffraction from the edges of the finite ground plane on the BMAA response, the edges of the ground plane are covered with thin absorbers (6.35 mm thick ECCOSORB LS-30/SS-3 absorbers manufactured by Emerson & Cuming). The dipole antenna and the BMAA are placed in the far field of each other in an open environment free of scatterers and the center of the dipole is aligned with the edge of the ground plane of the BMAA to ensure that the incident plane wave is arriving along the azimuth plane. Absorbers are placed on the ground to suppress specular reflections from ground. For each incidence angle, the magnitude and phase of the three-port S-parameters of the system are recorded and the results are used to extract the BMAA amplitude and phase responses. These measurements are also repeated for a regular two-element antenna array with the same element type and spacing (i.e., BMAA without the coupling network).

Fig. 2.10 shows the measured and simulated output phase responses of this BMAA as a function of angle of incidence of the EM wave and compares it with that of a regular array with the same elements and dimensions. The simulations are done using CST Microwave studio and Agilent ADS as described in Section 2.3.2. As can be seen from Fig. 2.10, an excellent agreement is observed between the measured and simulated phase

responses of the regular antenna array. However, the measured output phase response of the BMAA is shifted towards negative θ values (the zero crossing occurs for $\theta \approx -15^\circ$). This shift is primarily attributed to the asymmetries in the coupling network, since it is conspicuously absent in the measurement result of the regular array. These asymmetries are most likely caused by the differences between the exact element values of the two inductors and the small (but inevitable) differences in the responses of the two transformers. Since the primary impact of these asymmetries on the BMAA's phase response is to move the zero crossing points away from boresight, their effects can be compensated for by using a simple phase shifter in line with one of the inputs of the BMAA's external coupling network. To accomplish this, a phase shifter with a phase shift of 4.7° was added between the second antenna element and the second input of the external coupling network. The phase shifter is implemented with a small piece of coaxial transmission line[5]. The output phase response of this BMAA with the added phase shifter is also presented in Fig. 2.10. As can be observed, adding this extra phase shifter recovers the desired BMAA output phase response. Finally, for comparison, the phase difference between two ideal isotropic receiving antennas separated by a distance of d ($kd\sin(\theta)$) is also plotted in Fig. 2.10. As can be observed, the measured phase enhancement factor of the BMAA at boresight is $\eta \approx 15.6$, which agrees very well with the designed value of $\eta \approx 15$.

Fig. 2.11 shows the measured and simulated output power levels at the two BMAA outputs. The results presented in this figure are normalized to the output power level achieved from a regular antenna array at boresight (i.e. BMAA without the coupling network). As expected, the simulated output power at the two ports of the BMAA is $11.6\,$dB lower at boresight compared to that of a regular array. The difference between the measured and simulated values for the normalized output power levels are attributed to the

[5]In doing this, the measured S-parameters of the antenna are imported into ADS and the phase shifter is implemented in ADS (A physical phase shifter has not been used.)

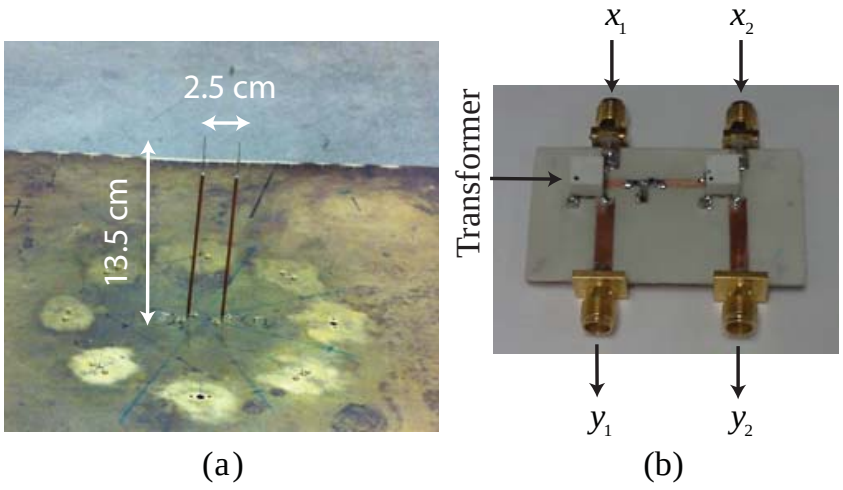

Figure 2.9 Photograph of the fabricated two-element biomimetic antenna array. (a) 3D view of the two monopoles. (b) The two-input two-output external coupling network.

asymmetries in the coupling network, which can not be compensated by the phase shifter, and also the lossy nature of the reactive components used[6]. It can be seen that the phase enhancement observed in the BMAA is indeed achieved at the expense of the reduction of the available output power. Specifically, the phase amplification factor of $\eta \approx 15.6$ (measured) in this device is achieved with a power reduction of approximately 12 dB. By comparing the results presented in this section with those of Section 2.3.1, it can be seen that the nonideal transformers used in this case have a significant impact on the performance of the BMAA. In particular, for the same output power level of $P_{out} = -12$ dB, the BMAAs that use ideal transformers offer a considerably larger phase enhancement factor ($\eta = 25$ compared to a simulated η value of 15.2). Alternatively, a phase enhancement

[6]Notice that in our design procedure, the components of the external coupling network except the transformers were assumed to be lossless. However, inductors with large inductance values are quite lossy at these frequencies. Additionally, because of the tolerances of these elements, these losses are not necessarily identical for the two inductors used in the external coupling network, which results in additional asymmetry in the circuit.

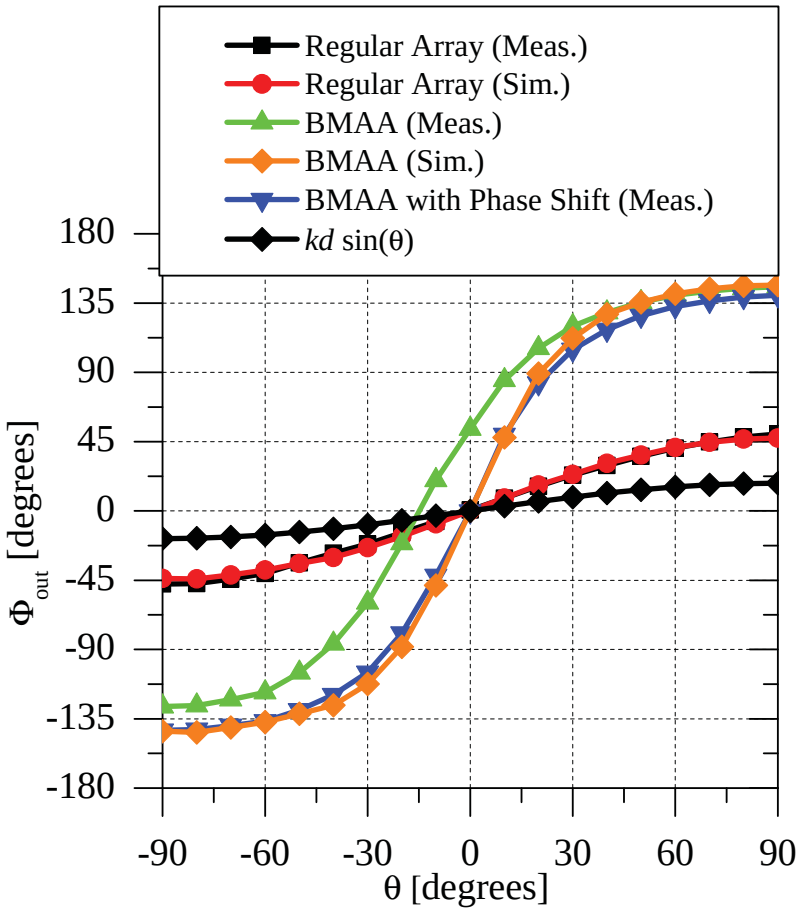

Figure 2.10 Measured and simulated output phase responses of the two-element BMAA discussed in Section 2.4. The simulated and measured output phase response of the regular array (BMAA without the external coupling network) is also shown. For comparison, the phase difference between two isotropic receiving antennas with a spacing of d, $kd\sin(\theta)$, is also shown. See Fig. 2.1 for definitions of positive and negative incidence angles.

factor of $\eta = 15.2$ can be achieved from a BMAA using ideal transformers with an output power level of $P_{out} = -7.5$ dB (see Fig. 2.3). The adverse impact of using nonideal transformers on the performance of the BMAA is attributed to two main factors. The first

reason is the loss of the transformer. When an ideal transformer is used in the external coupling network, the power entering the external coupling network and the output power P_{out} are equal. But when a non-ideal transformer is used, part of the power entering the external coupling network is lost in the transformer and the rest is delivered to the load. In the BMAA examined in this section, the power entering the external coupling network at boresight is $P_{in,\,c} = -10$ dB and the loss of the transformer is 1.6 dB. Thus, it is more appropriate to compare the phase amplification capability of the two coupling networks when the same amount of power is delivered to them. For comparison, an ideal external coupling network with an input power of -10 dB has a maximum phase amplification of $\eta \approx 21$ (refer to Fig. 2.3).

The other reason can be explained using Fig. 2.6. The value of the power entering the coupling network (at boresight) is determined by $Z_{in,\,c}$. As is evident in Fig. 2.6, the attainable values of $Z_{in,\,c}$ are limited to the solid curve in the complex plane. Particularly, the minimum value of the real part (resistance) of $Z_{in,\,c}$ is $9\,\Omega$. Thus, the optimum load resistance (in the ideal transformer case) of $R = 1.64\,\Omega$ can never be obtained with this transformer. The goal in the design of a BMAA with a non-ideal transformer is to find the optimum "achievable" phase amplification for a given output power. This is primarily dictated by the characteristics of the transformer. Due to the two reasons outlined above, there will generally be a difference between the values obtained when using ideal and nonideal transformers.

2.5 Conclusions

We presented a thorough examination of two-element antenna arrays that mimic the hyperacute sense of directional hearing of the parasitoid fly *Ormia Ochracea*. It was demonstrated that the phase enhancing properties of such BMAAs come at the expense

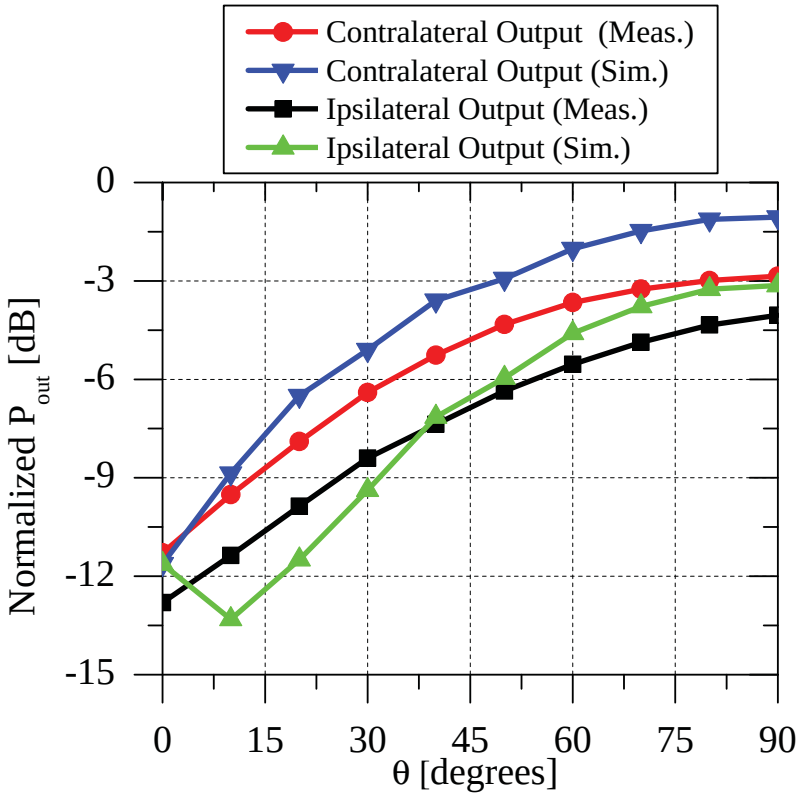

Figure 2.11 Angular variations of the output power at the two output ports of the BMAA discussed in Section 2.4. The results are normalized to the output power available from the regular array at boresight, P_0 in (2.11). Port 2 is the output closer to the incident wave (the ipsilateral antenna) and port 1 is the output further from the incident EM wave (the contralateral output).

of sacrificing the available power at the outputs of the array. However, for a given desired phase response, an optimum BMAA implementation exists that maximizes the output power level of the array. Alternatively, for a tolerable output power reduction compared to a regular array, the optimum BMAA implementation results in maximum phase enhancement factor. The effect of mutual coupling on the performance of the array was also examined. It was demonstrated that mutual coupling between the two receiving antennas

can enhance the available power at the output of a two-element BMAA. The impact of using nonideal transformers in the design of these arrays was also examined and a method for designing two-element BMAAs, which takes the actual frequency response of the transformers into account, was presented. Using this method, a prototype of a two-element BMAA was designed and experimentally characterized. The measurement results of this prototype verify the accuracy of the theoretical analyses presented in the paper. The results presented in this paper can be used to evaluate the suitability (or lack thereof) of such antenna arrays for applications such as small-aperture radio direction finding as well as sensing and imaging systems.

Chapter 3

An Improved Architecture for Two-Element Biomimetic Antenna Arrays

3.1 Introduction

The hyperacute sense of directional hearing of the parasitoid fly *Ormia Ochracea* has been studied since 1970s [44]-[45]. The amazing ability of this insect in detecting the direction of arrival of a sound wave, despite using an extremely small receiving aperture, inspired the development of new types of directional microphones in recent years [47]-[49]. Recently, biomimetic antenna arrays (BMAAs) that mimic the sense of directional hearing of this insect were also examined [50]-[51]. It was shown that such antenna arrays demonstrate enhanced directional sensitivities compared to regular antenna arrays that occupy the same aperture sizes [51]. However, this enhanced directional sensitivity comes at the expense of sacrificing the power level at the output of the BMAA [51]. In a recent article, we proposed an architecture for designing two-element BMAAs that mimic the sense of directional hearing of *Ormia Ochracea* and obtained a relationship between the maximum available power at the output and the phase sensitivity that can be achieved from these arrays [55]. It was demonstrated that as the desired phase sensitivity of the two-element BMAA increases, its available power decreases. Therefore, for any desired phase sensitivity, an optimum BMAA exists that provides the maximum available output power [55]. However, the two-element BMAA architecture examined in [55] suffers from

a practical limitation. Namely, it requires the use of two RF transformers in its external coupling network. Since transformers tend to become lossy and inefficient at high RF and microwave frequencies, the BMAAs of the type reported in [55] suffer from two major shortcomings. First, due to the transformer losses, they cannot offer the maximum output power level that can be theoretically achieved for a given phase enhancement factor [55]. Furthermore, due to the lack of suitable, low-loss RF transformers, they cannot be efficiently used at high RF and microwave frequencies.

In this paper, we present a new architecture for two-element BMAAs that mimic the sense of directional hearing of the parasitoid fly *Ormia Ochracea*. The new BMAA architecture does not employ any transformers and, for the same phase enhancement factor, it can provide a considerably higher output power level compared to the architecture examined in [55]. A two-element BMAA of the type reported in [55] or the type studied in this paper will inevitably be used as part of a wireless system. In such systems, the signal-to-noise ratio achievable at the antenna outputs is generally of particular importance. In this paper, we also examine the output noise of the proposed two-element BMAAs and compare it to that of the two-element BMAA reported in [55] (for the same output phase sensitivity). We demonstrate that the noise generated by the coupling network of the proposed BMAA architecture is comparable to that of the BMAA architecture reported in [55]. Therefore, the gains in signal-to-noise ratio (SNR) in the proposed design come from the increase in the level of the output signal power.

A prototype of a two-element BMAA that uses the proposed architecture is designed, fabricated, and experimentally characterized. This new prototype achieves a (simulated) measured output power level that is within $(1.5dB)$ $2dB$ of the theoretical limit at 600 MHz. Additionally, because it does not use any transformers, the new BMAA architecture is expected to be more amenable for operation at higher RF/microwave frequencies

and its coupling network can potentially be integrated on a single chip. Due to these advantages and the higher SNR that this structure provides, the two-element BMAA architecture reported in this paper is expected to be more suitable for practical high-frequency RF/microwave applications.

3.2 The Proposed Two-Element BMAA Architecture

The topology of the proposed two-element BMAA is shown in Fig. 3.1(a) and its equivalent circuit model is shown in Fig. 3.1(b). The two antennas are modeled with their Norton equivalent circuit models and the mutual coupling between them is modeled using two voltage controlled current sources. The external coupling network between the two antennas is composed of the reactances B_1 and B_2. The output loads are modeled with two parallel conductances of G_L as shown in Fig. 3.1(a). We assume that the two antennas are identical and that $I_{sc,1} = e^{-j\alpha}$ and $I_{sc,2} = e^{j\alpha}$ where $\alpha = \pi d \sin(\theta)/\lambda$. Using the common-mode and the differential-mode half circuits of the two-element BMAA shown respectively in Figs. 3.1(c) and 3.1(d), the voltages at the inputs of the coupling network, V_1 and V_2, can be obtained as:

$$V_1 = V_c - V_d = \frac{I_c(\theta)}{(G + G_{12}) + j\,b} - \frac{I_d(\theta)}{(G - G_{12}) + j\,a} \tag{3.1a}$$

$$V_2 = V_c + V_d = \frac{I_c(\theta)}{(G + G_{12}) + j\,b} + \frac{I_d(\theta)}{(G - G_{12}) + j\,a} \tag{3.1b}$$

where

$$I_c(\theta) = \frac{I_{sc,\,1}(\theta) + I_{sc,\,2}(\theta)}{2} \tag{3.2a}$$

$$I_d(\theta) = \frac{I_{sc,\,2}(\theta) - I_{sc,\,1}(\theta)}{2} \tag{3.2b}$$

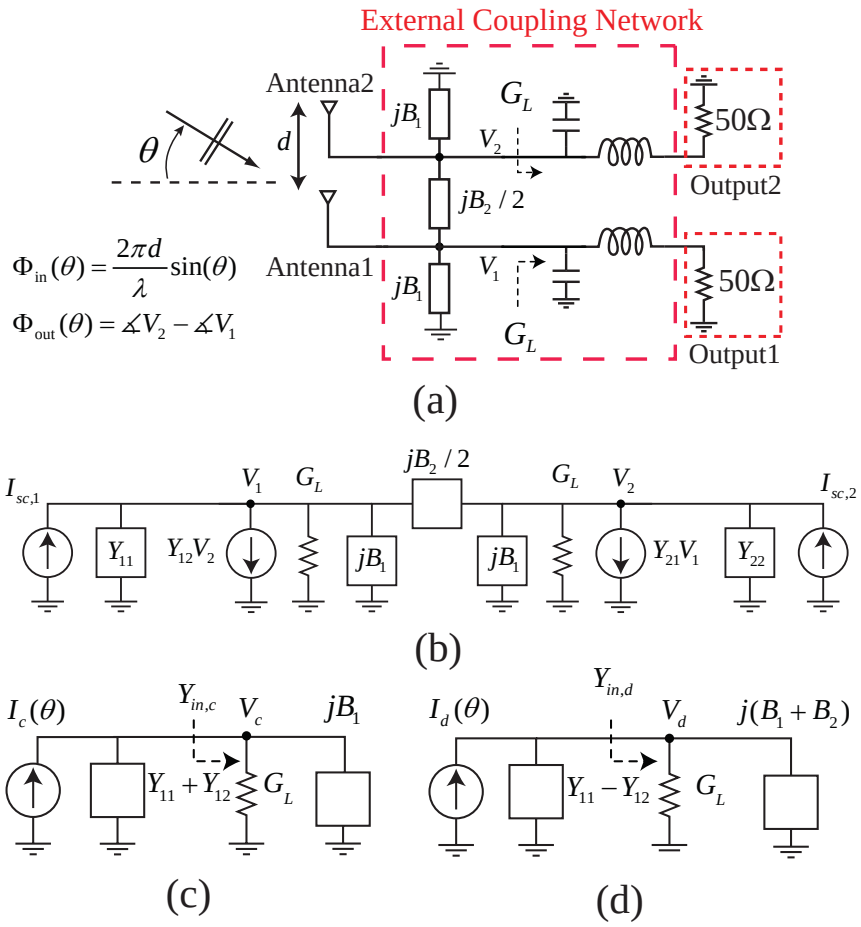

Figure 3.1 (a) Block diagram of the proposed two-element biomimetic antenna array (BMAA). (b) Equivalent circuit model of the two-element biomimetic antenna array. (c) The common-mode circuit. (d) The differential-mode circuit.

and

$$G = G_L + G_{11} \tag{3.3a}$$

$$a = B_{11} - B_{12} + B_1 + B_2 \tag{3.3b}$$

$$b = B_{11} + B_{12} + B_1 \, . \tag{3.3c}$$

At boresight, the output powers at both ports, corresponding to V_1 and V_2 in Fig. 3.1(a), are the same and are given by:

$$P_{out} = \frac{1}{2}G_L|V_1|^2\Big|_{\theta=0} = \frac{1}{2}G_L|V_2|^2\Big|_{\theta=0} \tag{3.4}$$

Let us define the output phase difference of the BMAA, $\Phi_{out}^{BMAA}(\theta) = \angle V_2 - \angle V_1$, as the phase difference between the two outputs of the BMAA. We will denote the slope of $\Phi_{out}^{BMAA}(\theta)$ with respect to θ at $\theta = 0^\circ$ by s (i.e., $s = \frac{d}{d\theta}\Phi_{out}^{BMAA}(\theta)|_{\theta=0^\circ}$). We define the slope of $\Phi_{in}(\theta)$ with respect to θ at $\theta = 0^\circ$ as s_0. Using this definition, the phase enhancement factor is defined to be $\eta = \frac{s}{s_0}$. Using a procedure similar to the one reported in [55], it can be shown that the *sufficient* condition for obtaining a realizable external coupling network for a given pair of (η, P_{out}) values is the existence of a real value of $G > G_{11}$ that satisfies both (3.5) and (3.6) simultaneously:

$$-G^2 + \left(\frac{1}{2P_{out}} - 2G_{12}\right)G - \left(\frac{G_{11}}{2P_{out}} + G_{12}^2\right) \geq 0. \tag{3.5}$$

$$\begin{aligned}(2\eta-1)^2G^2 - \left(\frac{1}{2P_{out}} + 2G_{12}(4\eta^2-1)\right)G \\ + \left((2\eta+1)^2G_{12}^2 + \frac{G_{11}}{2P_{out}}\right) \leq 0\ .\end{aligned} \tag{3.6}$$

Also, it can be shown that a and b must satisfy the following equations:

$$b^2 = -G^2 + \left(\frac{1}{2P_{out}} - 2G_{12}\right)G - \left(\frac{G_{11}}{2P_{out}} + G_{12}^2\right). \tag{3.7}$$

$$\eta a^2 - ab + \eta(G - G_{12})^2 - (G^2 - G_{12}^2) = 0\ . \tag{3.8}$$

The design procedure of the proposed BMAA is based on using the desired values of η and P_{out} in (3.3)-(3.8) to determine all of the parameters of the equivalent circuit model shown in Fig. 3.1(b). In Section 3.3, this will be demonstrated using a design example.

Table 3.1 Calculated Y-parameters of the two-element array discussed in Section 3.3 at 600 MHz. The Y-parameters are inclusive of the lengths of the transmission lines that connect the antennas to the external coupling network.

$G_{11} = \mathrm{Re}(Y_{11})$	$5.71\, m\mho$
$G_{12} = \mathrm{Re}(Y_{12})$	$5.30\, m\mho$
$B_{11} = \mathrm{Im}(Y_{11})$	$0.875\, m\mho$
$B_{12} = \mathrm{Im}(Y_{12})$	$10.26\, m\mho$

3.3 Design Example and Measurement Results

The design procedure of the proposed BMAA is demonstrated using a simple design example in this section. For this design, we consider a two-element antenna array composed of two 13.5 cm long monopole antennas spaced at a distance of 2.5 cm away from each other. The design and experiments are conducted at a frequency of 600 MHz. Therefore, the two monopole antennas are approximately a quarter wavelength long each and their separation is $0.05\lambda_0$ where λ_0 is the wavelength at 600 MHz. The two-port Y-parameters of the antennas, at the operating frequency of 600 MHz, are obtained from full-wave electromagnetic simulations in CST Microwave Studio and the results are presented in Table 5.1[1]. As can be seen in Table 5.1, $G_{12} \neq 0$. Therefore, there is mutual coupling between the two antenna elements.

For a given value of P_{out}, (3.3)-(3.8) can be used to determine the maximum possible value of η, henceforth referred to as η_{max}. Fig. 3.2 shows the value of η_{max}, which can be

[1]The transmission lines connecting the antenna elements to the coupling network are regarded as a part of the antenna. The length of these transmission lines is different in the current BMAA compared to the BMAA reported in [55]. This is due to the fact that the two monopoles are connected to SMA connectors and a shunt element cannot be inserted between them and the ground. Therefore a piece of a microstrip transmission line (shown by a dashed box in Fig. 3.5), was added to facilitate the fabrication of the antenna's coupling network.

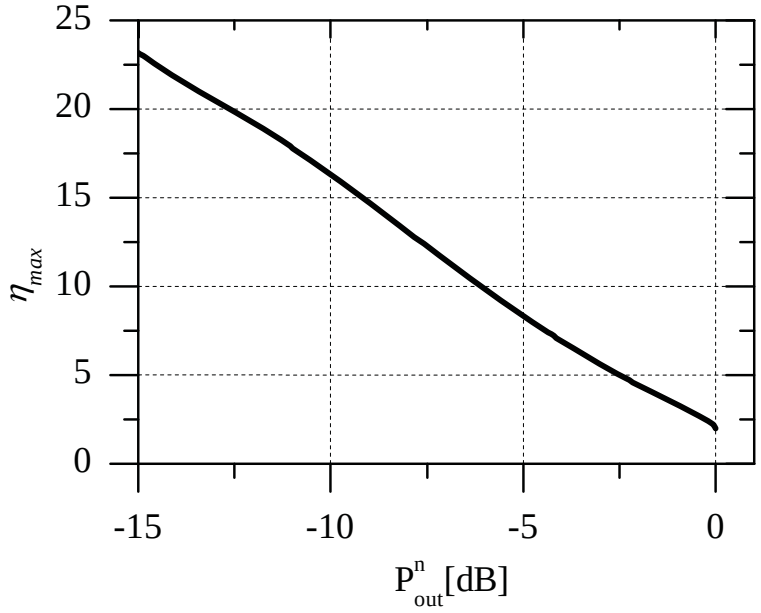

Figure 3.2 Variation of the maximum phase enhancement factor as a function of the output power for the two-element BMAA discussed in Section 3.3. This curve is obtained for the antenna array whose Y-parameters are provided in Table 5.1.

theoretically achieved for a given output power level for the antenna whose Y-parameters are given in Table 5.1[2]. In this figure, the horizontal axis shows the power at the outputs of the BMAA normalized to $P_0 = \frac{1}{8(G_{11}+G_{12})}$ (i.e., $P^n_{out} = P_{out}/P_0$). P_0 is the available power at the output of a regular two-element array (i.e., the BMAA without the external coupling network) when the antennas are connected to matched loads and the array is illuminated by a plane wave at boresight[3].

[2]Notice that since the Y-parameters of this antenna are different from those of the antenna reported in [55], the relationship between P^n_{out} and η_{max} shown in Fig. 3.2 is different from the one presented in [55].

[3]Assuming that the magnitude of the Norton equivalent circuit current sources is unity.

As can be seen from Fig. 3.2, for an arbitrarily chosen output power level of $P_{out}^n = -6$ dB, the value of η_{max} that can be achieved from a two-element BMAA with an ideal coupling network is approximately equal to 10. Therefore, for this design example, we choose $P_{out}^n = -6$ dB and $\eta = 9.85$. Using these values for P_{out}^n and η in conjunction with the theoretical analysis presented in Section 3.2, it can easily be shown that, $G = 6.501\, m\mho$ satisfies (3.5) and (3.6). Using (3.7) the value of b is calculated to be $b = \pm 0.193\, m\mho$. For each value of b, two distinct values of a can be obtained from (3.8). Thus there are a total of four possible coupling networks which yield the same pair of (P_{out}^n, η). Notice that the solution to this design example is not unique because for this desired output power level, a phase enhancement factor value smaller than η_{max} is chosen. Using these four values of a, b in conjunction with (3.3) and the equivalent circuit values given in Table 5.1, the element values of the external coupling network of the BMAA can be calculated. The four different possible realizations of the external coupling network is shown in Table 3.2. All four possible implementations have the same load conductance of $G_L = G - G_{11} = 6.501\, m\mho - 5.706\, m\mho = 0.795\, m\mho$. For the remainder of this example,

Table 3.2 The four possible implementations of the external coupling network of the BMAA examined in Section 3.3. At 600 MHz, the admittance value of B_1 is obtained using an inductor with an inductance of L and the reactance value of $B_2/2$ is obtained using a capacitor with a capacitance of C.

	C (pF)	L (nH)
Case 1	2.749	23.41
Case 2	2.695	24.24
Case 3	2.743	23.41
Case 4	2.701	24.24

we use the circuit values of Case 1 in Table 3.2. Using these values, the response of the BMAA is simulated in Agilent ADS and the results are presented in Figs. 5.6 and 5.7. Fig. 5.6 shows the output phase response of the BMAA as a function of the angle of incidence of the EM wave. Fig. 5.7 shows the normalized output power of the BMAA at its two outputs as a function of angle of incidence. The output power of the BMAA is normalized to the available power from a regular antenna array (i.e., BMAA without the coupling network) at boresight. As can be observed, at boresight, an output power level of -6 dB and a phase enhancement factor of 9.8 is achieved as predicted from the design example. The simulation results are also repeated by taking into account the effects of the losses of the lumped element components used in the coupling and impedance matching networks and the results are also presented in Fig. 5.7. As can be observed, the output power level at boresight is decreased by approximately 1.5 dB compared to the theoretically predicted value, due to the losses. To compare the proposed BMAA architecture to the one that was previously reported in [55], we have also designed a two-element BMAA using the architecture reported in [55]. The BMAA uses two Z9314-AL transformers (from Coilcraft corporation) along with ideal lumped elements and is designed to provide a phase enhancement factor of $\eta = 10$. For this design, the simulated maximum output power level that can be achieved at the BMAA output is $P_{out}^{n} = -11.8$ dB, which is 4.3 dB lower than what is achieved here. Therefore, the proposed BMAA architecture improves the output power level by about 4.3 dB compared to the previously reported one.

The proposed two-element BMAA is fabricated and experimentally characterized. The fabricated external coupling netwrok is shown in Fig. 3.5. Two lumped-element L-C impedance matching networks are used in this BMAA (see Fig. 3.1(a)) to convert the 50Ω load impedances at the two output ports of the BMAA to the optimum G_L values calculated from the design procedure. The inductance and capacitance values used in this impedance matching network are respectively 65.2 nH and 1.04 pF. The fabricated

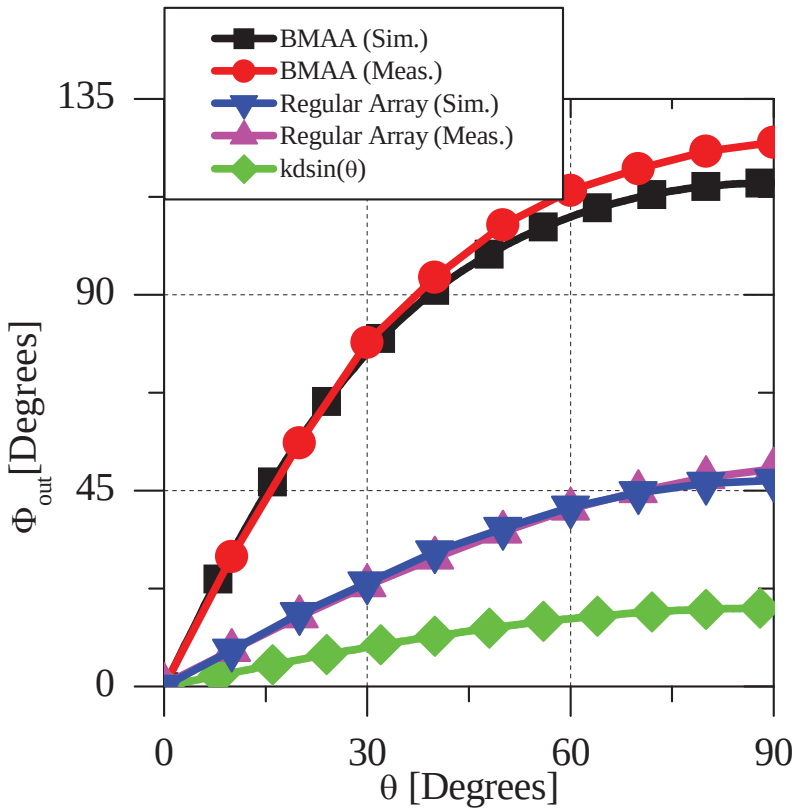

Figure 3.3 Measured and simulated output phase responses of the two-element BMAA discussed in Section 3.3 and that of a regular array ($k = \frac{2\pi}{\lambda}$).

BMAA was experimentally characterized using the measurement setup described in [55]. The measurement procedure used to obtain the results is identical to the one described in [55] and will not be repeated here for brevity. The measured output phase response of the BMAA is presented in Fig. 5.6 along with the simulated one. As can be observed, there is good agreement between the two results [4]. In particular, the measured output phase response shows a phase enhancement factor of approximately 10 as expected. The power

[4] As in [55], to compensate for asymmetries in the coupling network, a piece of 50 Ω transmission line with a length of ≈ 5 mm was added between the second antenna element and the second input of the external coupling network in ADS.

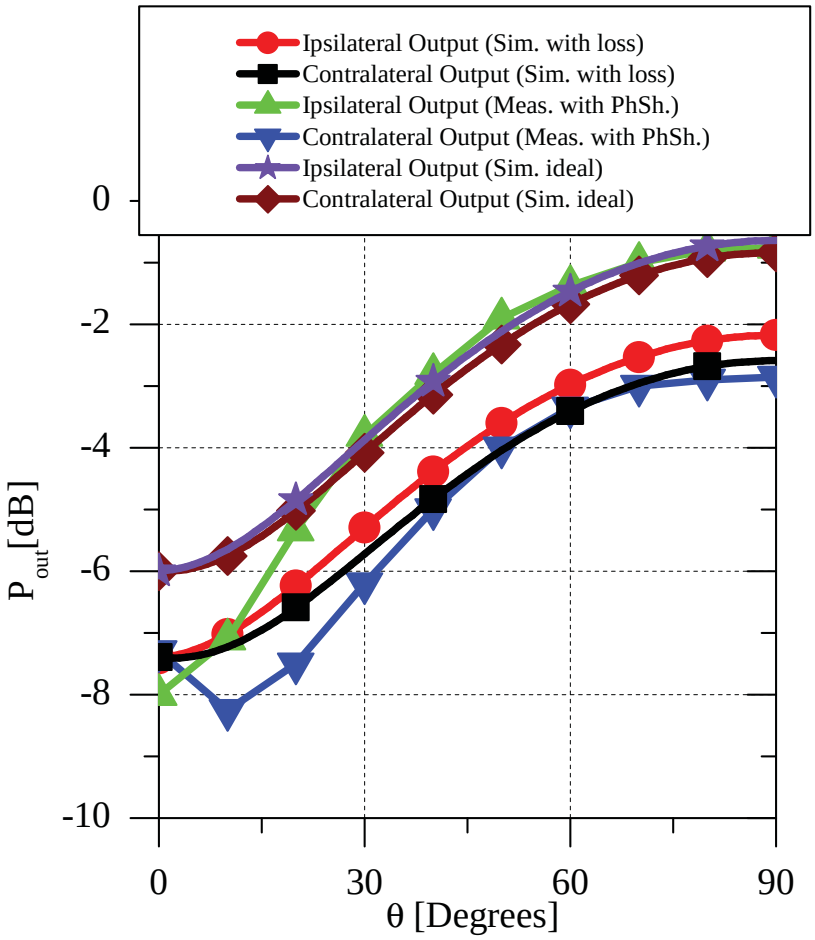

Figure 3.4 Measured and simulated amplitude responses of the two-element BMAA discussed in Section 3.3. Ipsilateral output is closer to the incident wave (port2) and the contralateral output is further from the incident wave (port 1).

at the two output ports of the BMAA are also measured and the results are presented in Fig. 5.7 along with the simulated ones. The measured output power level, at boresight, is approximately 1.3 dB and 2.0 dB lower than the output power value for the two ports predicted from the ideal coupling network (i.e., $P_{out}^{n} = -6.0$ dB). The difference observed between the output power levels of the two ports at boresight is attributed to the

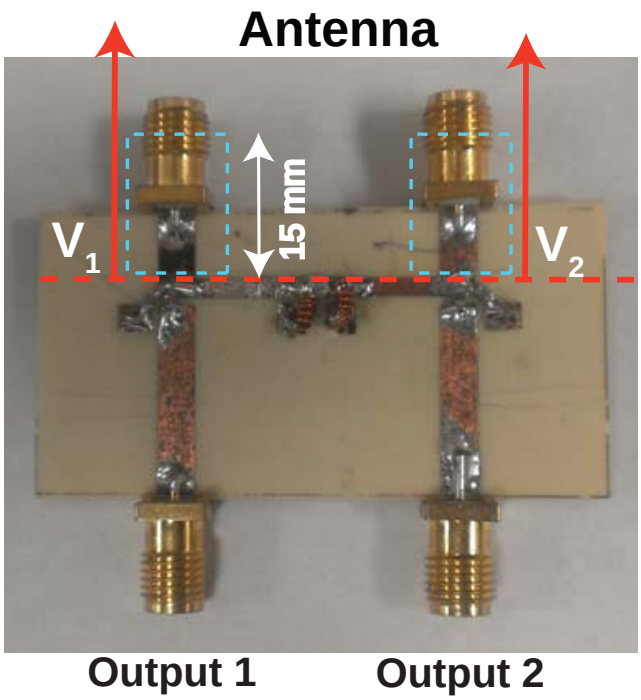

Figure 3.5 Photograph of the fabricated two-input two-output external coupling network used in the BMAA reported in this subsection.

inevitable asymmetries that exists in the construction of the coupling network as discussed in [55]. Similarly, the discrepancies observed between the measured and simulated results are attributed to the losses and component tolerances of the lumped elements used in the construction of the external coupling network and the inevitable asymmetries that exist in the fabricated coupling network as comprehensively described in [55]. Nonetheless, the measurement results demonstrate that the desired combination of P_{out} and η values can be achieved as predicted from the theoretical analysis.

It is noted that the BMAA has a relatively narrow phase enhancement factor bandwidth. The simulated 3-dB bandwidth of η for the BMAA presented in this work is $\approx$30 MHz

(or equivalently 5% fractional bandwidth). The narrow-band nature of the response of this BMAA can be explained using the differential and common-mode equivalent circuits of Fig. 3.1. If we consider a $200\,\text{MHz}$ frequency range around the center frequency of $f = 600\,\text{MHz}$, the common-mode antenna admittance does not vary considerably while the differential-mode antenna admittance changes significantly over this frequency range. Therefore, the optimum input admittance for the differential-mode could not be achieved over this entire frequency range. Furthermore, the narrow bandwidth of the matching section (which transforms the $50\,\Omega$ load to the load conductance G_L) further decreases the bandwidth of η.

3.4 Noise Analysis of the BMAA

In this section we present an analysis of the output noise of the proposed BMAA architecture and compare the results with the output noise of the two-element BMAA architecture presented in [55]. Fig. 3.6 shows the equivalent circuit model of the proposed two-element BMAA, which includes three main sources of noise. The thermal noises due to the antennas' ohmic losses are modeled using two $\bar{i}^2_{n,Loss}$ current sources. The root mean square value of this current is $i_{n,Loss} = \sqrt{4kT\Delta f G_{Loss}}$, where T is the antenna temperature in degrees Kelvin, Δf is the system bandwidth, k is the Boltzman's constant, and G_{Loss} is the loss conductance associated with the antennas. The second source of noise is due to the non-ideal (lossy) components that are used in the coupling and matching network. Specifically, the inductors are modeled by an ideal inductor in series with a resistance of $R_{ind} = \frac{\omega L}{Q_L}$, where Q_L is the inductor's quality factor and the capacitors are modeled by an ideal capacitor in parallel with a resistance of $R_{cap} = \frac{Q_C}{\omega C}$, where Q_C is the capacitor's quality factor. The noise sources of the inductors and capacitors of the matching network are modeled in a similar fashion. The lumped elements used

in the fabricated antenna prototype have $Q_L = 60$ and $Q_C = 1000$ at 600 MHz. The noise contribution of the elements of the coupling network are due to the thermal noise of the R_{ind} and R_{cap} resistors. The third source of noise is the noise of the load resistance $R = 50\,\Omega$ with a root mean square value of $i_{n,L} = \sqrt{\frac{4kT\Delta f}{R}}$. There is also the noise picked up by the antennas from the environment which is modeled using the $\bar{i}^2_{n,ext}$ current source. The strength of this source depends on the background temperature and the environment in which the antennas are located in. Since in this work we are primarily concerned with the impact that the coupling network has on the output noise of the antenna, we ignore this noise source in our analysis. Notice, however, that this noise source is in parallel with the two $\bar{i}^2_{n,Loss}$ noise sources. Therefore, its effect can easily be taken into account once the strength of the source is determined from the knowledge of the environment in which the antennas are located in as well as the background temperatures.

The output noise spectral density of the BMAA discussed in Section 3.3 is calculated using basic circuit analysis techniques and the results are shown in Fig. 3.7. The results for three different values of G_{loss} are presented. As can be observed, the available output noise power for the antenna examined in this work is ≈ -172.5 dBm. A similar noise analysis is also performed for a two-element BMAA of the type reported in Fig. 2 of [55]. To make a fair comparison, this BMAA is designed to provide the same value of η as the one examined in this work. In this structure, in addition to the losses of the antenna and the inductors and capacitors, the transformer losses also contribute to the output noise. The equivalent noise sources of the transformers reported in [55] are calculated based on their equivalent circuit model. Using these, the output noise of the structure is calculated and the results are presented in Fig. 3.7 for the same three values of G_{loss}. As can be observed, the output noise spectral density of a BMAA of the type reported in [55] is approximately ≈ -172.25 dBm. Considering the fact that the BMAA examined in this work offers a 4.3

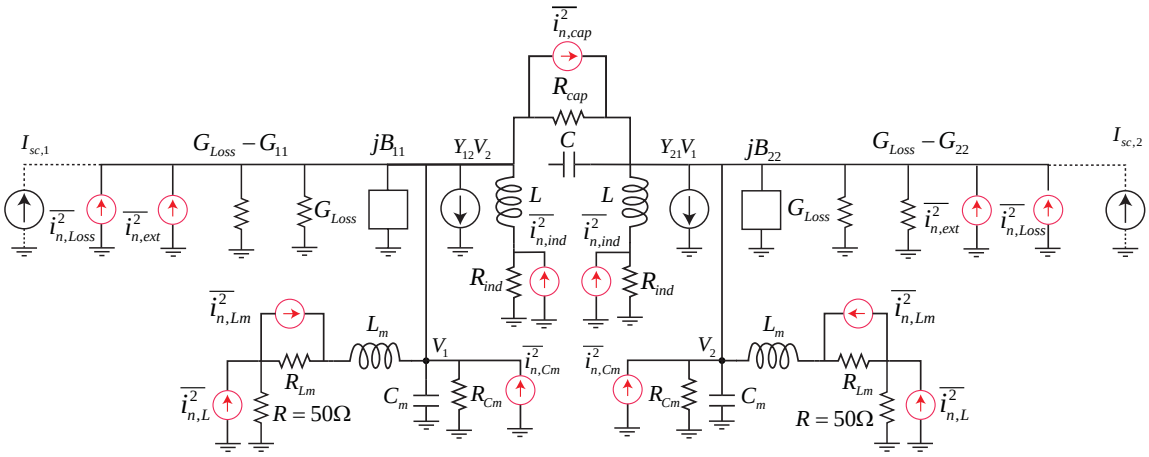

Figure 3.6 Equivalent circuit of the BMAA for noise analysis. $I_{sc,1}$ and $I_{sc,2}$ are the short circuit currents of the two antennas (without considering noise currents).

dB higher output power level, it can be seen that an SNR improvement of 4.55 dB can be achieved by using the proposed design compared to the one reported in [55].

3.5 Conclusions

In this section, a new architecture for two-element antenna arrays that mimic the sense of directional hearing of *Ormia Ochracea* was presented. The new BMAA architecture does not rely on using high-frequency RF transformers to achieve the desired performance and hence, offers two major improvements compared to the structure reported previously [55]. First, for the same phase enhancement factor, it offers a significantly higher output power level compared to the structure reported in [55]. Thus, the output signal to noise ratio of the antenna can be enhanced considerably. Additionally, because of the elimination of transformers from the antenna's coupling network, the new BMAA is expected to be more amenable to operation at higher RF/microwave frequencies where low-loss transformers are not available. A prototype of such a two-element BMAA was also designed,

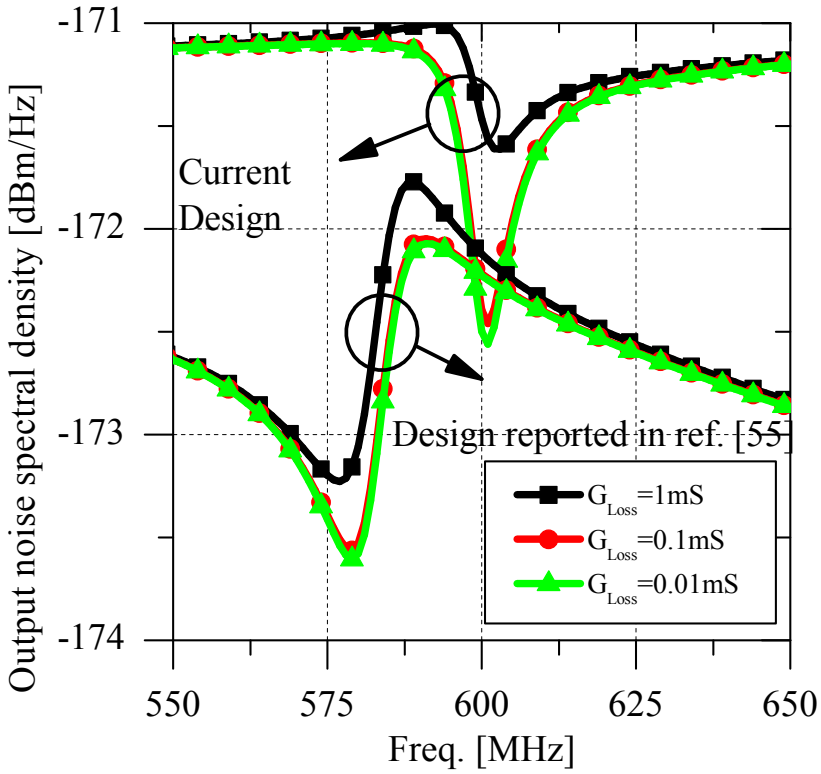

Figure 3.7 Simulated output noise spectral density of the two-element BMAA discussed in Section 3.3.

fabricated, and experimentally characterized. Measurement results presented in the paper were in good agreement with the theoretical predictions and demonstrated the gains that could be achieved in enhancing the output power level for a given output phase sensitivity.

Chapter 4

Architecture, Design, and Nonlinear Optimization of Three-Element Biomimetic Antenna Arrays

4.1 Introduction

Antenna arrays with closely-spaced elements are needed in array applications where sufficient space may not be available to accommodate a large aperture (e.g. small-aperture direction finding, mobile VHF/UHF communication systems, etc.). Typically, these arrays are connected to a passive external network for the purposes of pattern synthesis [31], noise matching [36], and decoupling of the antenna elements [30]. Two-element biomimetic antenna arrays (BMAAs), which mimic the sense of directional hearing of insects, are an example of such small-aperture arrays [50]-[51]. A BMAA consist of a regular antenna array with closely-spaced elements connected to a passive external coupling network. A two-element BMAA can provide a significantly enhanced phase sensitivity compared to its regular array counterpart. However, this comes at the expense of sacrificing the output power of the array [51],[55]. In particular, the main drawback of the previously reported two-element BMAA designs is the degradation of the output power level of the array as its phase sensitivity is increased [51],[55]. Therefore, systems that use such two-element BMAAs will inevitably sacrifice the range of the system in favor of the enhanced resolution that the BMAA offers [55]. Furthermore, the two-element BMAA architectures

discussed in [51],[55] are not readily expandable to arrays with an arbitrary number of elements.

In this chapter, a new BMAA architecture suitable for multi-element arrays is presented. This array architecture is used to design a three-element BMAA with uniform spacing between the elements. Similar to the previously-reported BMAAs, the proposed array exhibits an enhanced output phase sensitivity compared to a regular antenna array with the same aperture size and elements. However, the array is optimized to extract the maximum available power that this three-element aperture can receive, irrespective of the phase enhancement factor. In other words, this three-element BMAA architecture combines the advantages of the previously reported BMAAs (i.e., enhanced phase sensitivity) and a conventional array (i.e., maximum output power). This added feature can be advantageous in low signal-to-noise-ratio (SNR) scenarios where the output power level of a conventional BMAA is near the noise level. In such a situation, not only a reliable phase measurement cannot be made (i.e., phase enhancement properties of the BMAA are not used) but also no signal can be detected in the first place (i.e., gain of the system is reduced resulting in a reduced range). Using the new architecture, however, one of the outputs of the array always receives the maximum power that can be received from a three-element antenna array of this dimension. Therefore, in situations where the SNR is high, both the phase enhancement capabilities and the high output power level of the array may be exploited by the receiver. In low SNR situations on the other hand, while the array may not be capable of taking full advantage of the phase enhancement capabilities of the BMAA, it receives the maximum available power that can be extracted from the incoming wave nonetheless. Furthermore, the topology of the three-element BMAA introduced in this work may also be easily extended to other arrays with an arbitrary number of elements. The introduced BMAA can potentially have applications in long-range small-aperture direction finding systems, MIMO communications and microwave imaging. In what follows

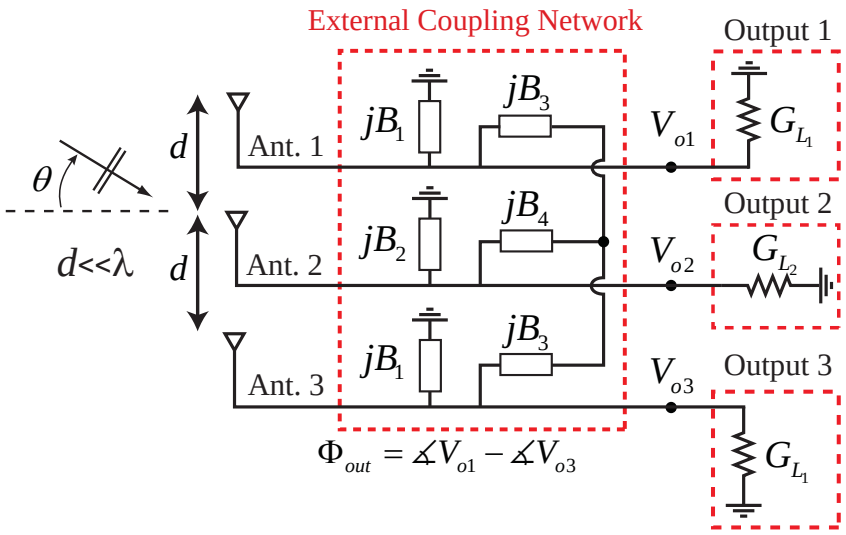

Figure 4.1 Block diagram of a three element biomimetic antenna array. The antennas are assumed to be identical and the external coupling network is symmetric.

details of the design and optimization process of the proposed three-element BMAA along with numerical simulation results of a prototype are presented and discussed.

4.2 Problem Formulation

The block diagram of a three element BMAA is shown in Fig. 4.1. We consider a linear array consisting of three $\lambda/4$ monopole antennas with an element spacing of $d = \frac{\lambda}{20}$. The monopoles are mounted on an infinite ground plane and the frequency of operation is 600 MHz. The admittance matrix of the three element antenna array is denoted by Y_a. Due to the fact that the antennas are identical and uniformly spaced, we have:

$$Y_a = \begin{pmatrix} G_{11}+jB_{11} & G_{12}+jB_{12} & G_{13}+jB_{13} \\ G_{12}+jB_{12} & G_{22}+jB_{22} & G_{12}+jB_{12} \\ G_{13}+jB_{13} & G_{12}+jB_{12} & G_{11}+jB_{11} \end{pmatrix}. \tag{4.1}$$

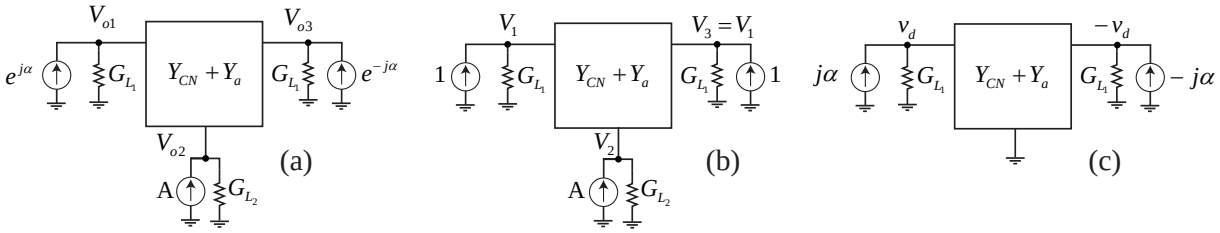

Figure 4.2 a) Equivalent circuit model of the BMAA. b) common-mode circuit. c) differential-mode circuit.

A plane-wave with an incidence angle of θ is assumed to be incident on the array (θ is measured from boresight). The external coupling network is a symmetric, passive three port network, which consists of six reactive passive components. The admittance matrix of the external coupling network is denoted by Y_{CN} and is given by:

$$Y_{CN} = \begin{pmatrix} j(B_1 + \frac{B+B_3}{2}) & -jB & j(\frac{B-B_3}{2}) \\ -jB & j(B_2+2B) & -jB \\ j(\frac{B-B_3}{2}) & -jB & j(B_1 + \frac{B+B_3}{2}) \end{pmatrix} \tag{4.2}$$

where

$$B = \frac{B_3 B_4}{2B_3 + B_4}. \tag{4.3}$$

Since the external coupling network and the antennas are in parallel with each other, the coupling network essentially changes the admittance matrix of the antennas to $Y_a + Y_{CN}$. The equivalent circuit of the three element BMAA is shown in Fig. 4.2(a). The short-circuit currents of the antennas are denoted by $I_{sc,1} = e^{j\alpha}$, $I_{sc,2} = A$ and $I_{sc,3} = e^{-j\alpha}$ where $\alpha = \frac{2\pi d}{\lambda}\sin(\theta)$ and A, which represents the amplitude of the short-circuit current of the center element, is a constant to be determined by full-wave simulations[1]. At incident

[1]Notice that the amplitude of the short circuit current of the center antenna may not necessarily be the same as those of the ones at the edges of the array. The constant A is the ratio of the amplitude of the short circuit current of the center element to that of the edge antennas. Throughout this paper, the unit of short-circuit currents are in Amperes.

angles close to boresight, the short-circuit currents can be written as:

$$I_{sc,1} = e^{j\alpha} = \cos(\alpha) + j\sin(\alpha) \approx 1 + j\alpha$$
$$I_{sc,2} = A$$
$$I_{sc,3} = e^{-j\alpha} = \cos(\alpha) - j\sin(\alpha) \approx 1 - j\alpha$$

and we can use the common- and differential-mode circuits of Fig. 4.2(b) and Fig. 4.2(c) to determine the output voltages,

$$V_{o1} = V_1 + v_d \tag{4.4a}$$
$$V_{o2} = V_2 \tag{4.4b}$$
$$V_{o3} = V_3 - v_d = V_1 - v_d \tag{4.4c}$$

where V_1-V_3 are the terminal voltages in the common-mode. Note that due to the symmetry of the BMAA, the common-mode output voltages at ports 1 and 3 (i.e. V_1 and V_3) are equal and the differential-mode output voltages at ports 1 and 3 have opposite signs. Moreover there is a virtual ground at port 2 in the differential-mode.

We first find expressions for the output power of the BMAA at boresight ($\theta = 0$) using the common-mode circuit of the BMAA shown in Fig. 4.2(b). The output voltages at boresight, which are denoted by $V_{o1} = V_{o3} = V_1$ and $V_{o2} = V_2$, satisfy the following equation:

$$\begin{pmatrix} 1 \\ A \\ 1 \end{pmatrix} = Y \begin{pmatrix} V_1 \\ V_2 \\ V_3 \end{pmatrix} = Y \begin{pmatrix} V_{1r} + jV_{1i} \\ V_{2r} + jV_{2i} \\ V_{1r} + jV_{1i} \end{pmatrix} \tag{4.5}$$

where

$$
\begin{aligned}
Y &= Y_{CN} + Y_a + Y_L \\
&= \begin{pmatrix} G_{L_1} + G_{11} + ja & G_{12} + jc & G_{13} + jd \\ G_{12} + jc & G_{L_2} + G_{22} + jb & G_{12} + jc \\ G_{13} + jd & G_{12} + jc & G_{L_1} + G_{11} + ja \end{pmatrix}
\end{aligned} \tag{4.6}
$$

and

$$
Y_L = \begin{pmatrix} G_{L_1} & 0 & 0 \\ 0 & G_{L_2} & 0 \\ 0 & 0 & G_{L_1} \end{pmatrix}. \tag{4.7}
$$

Here, the reactances of the antennas and those of the coupling network are added together and are represented by the real numbers a, b, c and d. The power at the output ports of the BMAA at boresight are $P_1 = P_3 = 0.5G_{L_1}|V_1|^2$ and $P_2 = 0.5G_{L_2}|V_2|^2$.

Next, the phase enhancement factor of the BMAA is calculated. The phase enhancement factor is defined to be $\eta = \frac{s}{s_0}$, where

$$
s_0 = \left.\frac{d(2\alpha)}{d\theta}\right|_{\theta=0} = \frac{4\pi d}{\lambda} \tag{4.8}
$$

and s is the slope of the output phase, $\Phi_{out} = \measuredangle V_{o1} - \measuredangle V_{o3}$, with respect to the angle of incidence, θ, at boresight, i.e.

$$
s = \left.\frac{d\Phi_{out}}{d\theta}\right|_{\theta=0} = \left(\left.\frac{d\Phi_{out}}{d(2\alpha)}\right|_{\alpha=0}\right)\left(\left.\frac{d(2\alpha)}{d\theta}\right|_{\theta=0}\right). \tag{4.9}
$$

Using the differential-mode circuit of the BMAA at incident angles close to boresight (refer to Fig. 4.2(c)), the following system of equations can be obtained for v_d:

$$
\begin{pmatrix} j\alpha \\ 0 \\ -j\alpha \end{pmatrix} = Y \begin{pmatrix} v_d \\ 0 \\ -v_d \end{pmatrix} \tag{4.10}
$$

we have:

$$v_d = \frac{j\alpha}{(G_{L_1} + G_{11} - G_{13}) + j(a-d)} \triangleq j\alpha V_d. \tag{4.11}$$

Using (4.4a), (4.4c), (5.9), (5.11) and (4.11), η can be written as:

$$\begin{aligned}\eta &= \lim_{2\alpha\to 0}\left[\frac{\measuredangle V_{o1} - \measuredangle V_{o3}}{2\alpha}\right] = \lim_{2\alpha\to 0}\left[\frac{1}{2\alpha}\measuredangle\left\{\frac{1+j\alpha\frac{V_d}{V_1}}{1-j\alpha\frac{V_d}{V_1}}\right\}\right] \\ &= \lim_{2\alpha\to 0}\left[\frac{2}{2\alpha}\tan^{-1}\left(\frac{\alpha\,\mathrm{Re}\left\{\frac{V_d}{V_1}\right\}}{1-\alpha\,\mathrm{Im}\left\{\frac{V_d}{V_1}\right\}}\right)\right] \\ &= \mathrm{Re}\left\{\frac{V_d}{V_1}\right\} = \frac{V_{dr}V_{1r} + V_{di}V_{1i}}{{V_{1r}}^2 + {V_{1i}}^2}\end{aligned} \tag{4.12}$$

where V_{dr} and V_{di} are the real and imaginary parts of V_d respectively. For each given value of P_1, the value of the phase enhancement is bound by an upper limit, which can be calculated as follows:

$$\begin{aligned}\eta &= \mathrm{Re}\left\{\frac{V_d}{V_1}\right\} \leqslant \left|\frac{V_d}{V_1}\right| \\ &\leqslant \sqrt{\frac{G_{L_1}}{2P_1}}\left|\frac{1}{(G_{L_1} + G_{11} - G_{13}) + j(a-d)}\right| \\ &\leqslant \frac{1}{\sqrt{2P_1}}\frac{\sqrt{G_{L_1}}}{(G_{L_1} + G_{11} - G_{13})}.\end{aligned} \tag{4.13}$$

By taking the derivative of the right hand side with respect to G_{L_1} and setting it equal to 0, we arrive at the following upper bound for η:

$$\eta \leqslant \sqrt{\frac{1}{8\,(G_{11} - G_{13})\,P_1}}. \tag{4.14}$$

4.3 BMAA Optimization

To determine the values of the elements used in the BMAA coupling network, we use an optimization process. The goal of this process is to design a three element BMAA

that maximizes P_2 for given values of P_1 and η. Since this problem is too complicated to be solved analytically, we have used a numerical optimization procedure. To do this, the problem is formulated using a modeling language and a numerical optimization routine is invoked to find a near optimum solution. In this work, we have formulated the problem using A Mathematical Programming Language (AMPL), which is a popular modeling language used in the field of numerical optimization [58]. With this modeling language, the user declares the variables and constraints of the optimization process and the optimization goal is defined as a function of these variables. The constraints and variables can be in the form of equalities or inequalities. In this case, the declared variables are $a, b, c, d, G_{L_1}, G_{L_2}, V_{1r}, V_{1i}, V_{2r}, V_{2i}, V_{dr}$, and V_{di} and there are a total of 8 constraints. First, using (4.5), we arrive at four independent constraints (two for the imaginary parts and two for real parts):

$$(G_{L_1} + G_{11} + G_{13})V_{1r} + G_{12}V_{2r} - (a+d)V_{1i} - cV_{2i} = 1 \tag{4.15a}$$

$$(a+d)V_{1r} + cV_{2r} + (G_{L_1} + G_{11} + G_{13})V_{1i} + G_{12}V_{2i} = 0 \tag{4.15b}$$

$$2G_{12}V_{1r} + (G_{L_2} + G_{22})V_{2r} - 2cV_{1i} - bV_{2i} = A \tag{4.15c}$$

$$2cV_{1r} + bV_{2r} + 2G_{12}V_{1i} + (G_{L_2} + G_{22})V_{2i} = 0 \tag{4.15d}$$

Subsequently, (4.11) yields the following two constraints:

$$(G_{L_1} + G_{11} - G_{13})V_{dr} - (a-d)V_{di} = 1 \tag{4.16a}$$

$$(a-d)V_{dr} + (G_{L_1} + G_{11} - G_{13})V_{di} = 0 \tag{4.16b}$$

Since the value of P_1 is assumed to be known, the power constraint is given by:

$$P_1 = 0.5G_{L_1}\left({V_{1r}}^2 + {V_{1i}}^2\right). \tag{4.17}$$

and finally, from (4.12) and (4.17), we have:

$$2P_1\eta = G_{L_1}(V_{dr}V_{1r} + V_{di}V_{1i}) \tag{4.18}$$

The objective of the optimization process is to maximize P_2:

$$P_2 = 0.5 G_{L_2} \left({V_{2r}}^2 + {V_{2i}}^2 \right). \tag{4.19}$$

In this example we have chosen $\eta = 8$ and $P_1 = 1\,W$ for the phase enhancement and output power at boresight, respectively. Note that for this value of ${P_1}^2$, the maximum possible phase enhancement can be calculated using (4.14) and is equal to $\eta_{max} = 9.18$. The conductance and susceptance values for the antenna array are obtained from full-wave EM simulations in CST Microwave Studio and are given in Table 4.1. The amplitude of the short-circuit current of the center element at boresight is also found to be $A = 0.77$. After setting up the problem in AMPL, a nonlinear optimization program is invoked and

Table 4.1 Simulated conductance and susceptance values for the linear three element monopole array at $600\,$MHz. Each element has a length of $\lambda/4$. All values are reported in mS.

G_{11}	3.58	G_{12}	2.17	G_{13}	2.10	G_{22}	1.66
B_{11}	-7.11	B_{12}	10.33	B_{13}	4.39	B_{22}	-10.75

the numerical values of the variables that maximize the goal are found. The optimization engine used in this process is SNOPT[3], which is a numerical optimization code suited for nonlinear problems. Using this process, the maximum value for the objective is found to be $P_2^{max} = 42.44\,W$. The values of the variables that maximize the optimization goal are presented in Table 4.2[4]. Using these variable values, the reactance values of the coupling network are calculated by solving the following system of equations (refer to (4.2)-(4.3)

[2]The choice of P_1 is arbitrary but it affects the maximum value of the phase enhancement factor.

[3]From Stanford Business Software, Inc.

[4]Since this problem is a nonlinear optimization problem, there is no guarantee that the values obtained are for the global maximum of the objective function. Indeed, for certain combination of initial values of the variables, the optimization problem does not converge.

Table 4.2 Value of variables found by SNOPT, which maximize the objective and the calculated values for the components of the external coupling network. All values are reported in mS.

a	9.42	b	0.41	c	-3.47	d	9.46
G_{L_1}	1.77	G_{L_2}	3.34				
B_1	7.79	B_2	-16.44	B_3	3.66	B_4	-9.96

and (4.6)):

$$\begin{aligned}\begin{pmatrix} a \\ b \\ c \\ c \end{pmatrix} &= \begin{pmatrix} B_{11} \\ B_{22} \\ B_{12} \\ B_{13} \end{pmatrix} + \begin{pmatrix} B_1 + \frac{B+B_3}{2} \\ B_2 + 2B \\ -B \\ \frac{B-B_3}{2} \end{pmatrix} \\ &= \begin{pmatrix} B_{11} \\ B_{22} \\ B_{12} \\ B_{13} \end{pmatrix} + \begin{pmatrix} 1 & 0 & \frac{1}{2} & \frac{1}{2} \\ 0 & 1 & 0 & 2 \\ 0 & 0 & 0 & -1 \\ 0 & 0 & -\frac{1}{2} & \frac{1}{2} \end{pmatrix} \begin{pmatrix} B_1 \\ B_2 \\ B_3 \\ B \end{pmatrix} \end{aligned} \tag{4.20}$$

and are also shown in Table 4.2. B_1 and B_3 can be implemented using 2.07 pF and 0.97 pF capacitors and B_2 and B_4 can be implemented using 16.1 nH and 26.6 nH inductors at 600 MHz.

These component values are used in a circuit-EM co-simulation in CST Studio to obtain the response of the three-element BMAA. Fig. 4.3(a) shows the output phase response of the array as a function of the incidence angle. Observe that the the phase enhancement at boresight between the side elements is twice the phase enhancement between the center element and each of the side elements. Fig. 4.3(b) shows the output power level of the three ports of the BMAA as a function of the angle of incidence. The power is normalized to

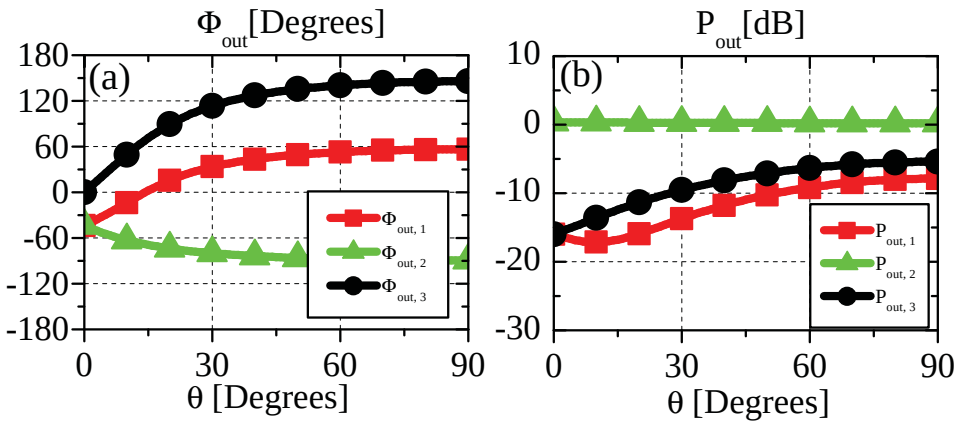

Figure 4.3 (a) Simulated output phase responses of the three-element BMAA. $\Phi_{out,1} = \measuredangle V_{o1} - \measuredangle V_{o2}$, $\Phi_{out,2} = \measuredangle V_{o3} - \measuredangle V_{o2}$ and $\Phi_{out,3} = \measuredangle V_{o1} - \measuredangle V_{o3}$. (b) Simulated output power of the three-element BMAA. The output power is normalized to the available power from an isolated monopole antenna of the same length as the BMAA antenna elements.

the available power from a single isolated monopole of the same length, which is mounted on an infinite ground plane[5]. Notice that the maximum available power from this three-element antenna array is $P_{av} = \frac{1}{4} I_{sc}^{*}(Y_a + Y_a^{*}) I_{sc} = 44.57\,W$ where $I_{sc} = [1; 0.77; 1]$ is the short-circuit current vector at boresight and ‘‘*” denotes conjugate transpose[59]. Thus, in the current BMAA, the power extracted from the signal at boresight is only 0.38% lower that the maximum available power from the antenna array (without the BMAA’s external coupling network). This indicates that the proposed three-element BMAA efficiently extracts the power from an incoming wave in addition to providing an enhanced phase sensitivity. Finally, the power level of the center output at boresight is roughly 16 dB higher than the power level of the side outputs as expected from the optimization process (i.e., $P_2/P_1 = 42.44/1$).

[5]For this isolated monopole antenna, the magnitude of the short-circuit current is $I_{sc} = 1.81$ and the input admittance is $Y_{in} = G_{in} + jB_{in} = 10.37 - j2.26$ mS. Thus, the available power is equal to $P_{av} = I_{sc}^2/(8G_{in}) = 39.5\,W$.

4.4 Conclusions

The architecture, design, and nonlinear optimization of a three-element biomimetic antenna array were presented and discussed in this section. For a given desired phase enhancement factor between the side outputs of the array, the array is optimized to extract the maximum available power at its center output. Therefore, this architecture offers the desirable phase enhancement factors of two-element BMAAs [51],[55] but also extract nearly the maximum possible power level that can be extracted from an array of this size. This feature is desirable and can alleviate some of the undesirable aspects of the range-resolution tradeoffs observed in two-element BMAAs of the types reported in [51], [55].

Chapter 5

A Two-Element Biomimetic Antenna Array with Enhanced Angular Resolution and Optimized Power Extraction

5.1 Introduction

The individual antenna elements in an array environment are generally impedance matched individually before they are connected to the array feed network. In a number of other designs, passive cross-coupled networks have also been used to feed the different elements of an antenna array. These coupling networks are in the form of multi-input-multi-output networks that create external cross coupling between the different antenna elements used in the array. These external coupling networks have been used for the purposes of decoupling the antenna elements [30]-[31], noise matching [36], and beam-forming [35],[61]. In [50]-[51], a two-element antenna array that mimics the sense of directional hearing of a small insect was presented. Referred to as a biomimetic antenna array (BMAA), this two-element electrically-small antenna array uses a passive external coupling network to achieve an enhanced output phase sensitivity compared to a regular antenna array occupying the same aperture dimensions. It has been demonstrated that such BMAAs can achieve output phase sensitivities that are significantly larger than those of regular antenna arrays with the same aperture dimensions [51]. Therefore, these antenna arrays are expected to find applications in areas where precise angular resolving capabilities are needed from small apertures (e.g. low-frequency direction finding applications).

While the previously reported passive BMAAs demonstrate higher angular sensitivities compared to conventional arrays of the same size, this added capability comes at the expense of sacrificing the output power of the antenna. This means that the better angular resolution of these arrays comes at the expense of limiting the range over which acceptable received signal-to-noise ratios (SNRs) can be achieved [55]-[56]. In certain applications, the reduction in the received signal power can degrade the system's performance and should be avoided if possible. In this chapter, we will first revisit the tradeoff between the output phase sensitivity and output power level of a two-element BMAA and provide a conceptual understanding of the source of this tradeoff. Subsequently, we propose a new coupled antenna array topology that addresses this important shortcoming of the biologically-inspired antenna arrays reported previously. In particular, the new coupled antenna array topology proposed in this chapter can be used to achieve moderate output phase sensitivities similar to some of the designs reported previously [55]-[56]. However, unlike the previously reported BMAAs, this enhanced phase sensitivity does not come at the expense of sacrificing the output power level of the array.

In this chapter, we will first present a theoretical analysis that can be used to determine an upper bound for the phase enhancement factor that can be achieved from a given two element antenna array without paying any penalty in terms of the output power level of the array. Here, the antenna array consists of two identical elements and the coupling network is assumed to be a passive 4-port network (with two inputs and two outputs). This analysis is then applied to a two-element antenna array operating at 600 MHz composed of two 13.5 cm monopole antennas separated by a distance of 2.5 cm. We demonstrate that this antenna array can theoretically show a phase sensitivity that is fives times higher than that of a regular array consisting of the same receiving elements, while extracting the same output power level from an incoming wave compared to the regular array. Next, an external coupling network is designed which achieves a phase enhancement of roughly 20%

less than the maximum possible value. The coupling network is realized using lumped components and transmission lines and the resulting two-element BMAA is fabricated and experimentally characterized. The measurements validate our theoretical findings and prove that the new BMAA architecture can be used to achieve moderate phase enhancement factors without any degradation in the output power level of the array.

5.2 Optimum BMAA Design

5.2.1 Principles of Achieving Angular Phase Sensitivity in Previously-Reported BMAAs

In a two element antenna array, one can imagine two independent modes of excitation. These include the common mode and the differential modes of excitation. The array is excited in the common (differential) mode when the two elements are excited with the same magnitude and a $0^{\circ}(180^{\circ})$ phase difference between them. When the array is used to receive an electromagnetic wave, the mode of excitation is determined by the angle of arrival of the EM wave and the spacing between the two elements. For instance, if the wave is incident from broadside, the array is excited purely in the common mode.

For an antenna array with a half-wavelength spacing between the two elements, the array will be excited in the differential mode if the incoming wave is incident on it from the end-fire direction. In general, when the array is illuminated with an oblique angle of incidence, the array is excited with a linear combination of the common and differential modes. For an array used in the receive mode, the relative strength of the power extracted from the differential mode of excitation compared to that from the common mode can be used to quantify the output phase sensitivity of the array. In a conventional antenna array with closely-spaced elements, the majority of the power extracted from the elements is

due to the common mode of excitation. In such cases, the power extracted from the differential mode is extremely small. Consequently, such arrays do not show any significant sensitivity to the angle of incidence of the incoming electromagnetic wave [1]. Biomimetic antenna arrays of the type reported in [55]-[56] offer a means of achieving enhanced angular sensitivities from antenna arrays with closely spaced elements (e.g. 0.05λ) compared to conventional antenna arrays. This enhanced angular sensitivity is obtained by using an external coupling network that increases the contrast between the power extracted from the common and the differential modes of excitation. In the BMAAs reported in [55]-[56], the external coupling network acts as a mode selective filter that attenuates the common mode of excitation more than the differential mode. Therefore, at the output of the array, the contrast between the common and differential modes of excitation is increased and the array demonstrates enhanced angular sensitivities. However, this process reduces the power available from the array compared to a conventional antenna array. Consequently, the enhanced angular sensitivities offered by the BMAAs reported in [55]-[56] is obtained at the expense of sacrificing the output power level of the array. For example, the design reported in [55] achieves a phase enhancement factor of 15.6 with a power degradation of 12 dB compared to a regular array. As with all other two-element antenna arrays, the two-element BMAAs reported in [55]-[56] can only be used to estimate the angle of arrival of one source. The BMAA concept has also been extended to arrays with multiple elements as discussed in [57].

The goal of the current chapter is to introduce a new coupling network and to outline a new design approach that enable achieving the maximum possible phase enhancement factor without sacrificing the output power of the BMAA compared to that of a regular array. To achieve this goal for a two-element antenna array, the antennas should be matched to the optimum load impedance for both the common *and* the differential modes of excitation. Matching the antenna in the common mode ensures that the maximum power is delivered

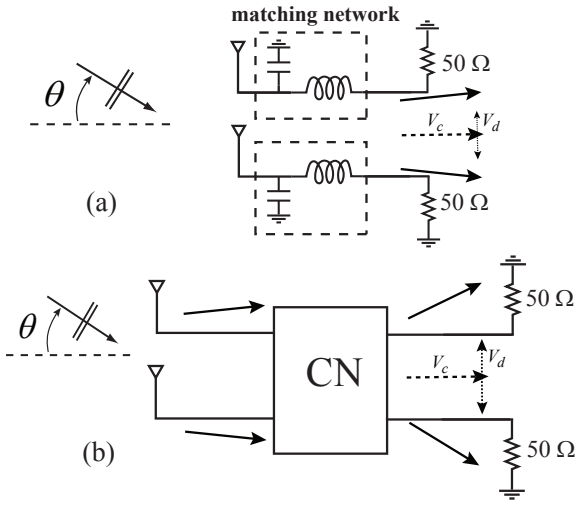

Figure 5.1 (a) A two-element regular antenna array where the receiving elements are individually impedance matched. (b) Block diagram of a two-element biomimetic antenna array (BMAA).

to a $50\,\Omega$ output load impedance when the array is excited with a plane wave incident from the boresight. Since the array has different impedances for these two linearly-independent modes of excitation, the external coupling network should be designed to perform differently for each mode. Matching the antenna in the differential mode results in maximizing the amplitude of the differential mode voltage at the $50\,\Omega$ output load when the array is excited with a plane wave with an oblique incidence angle. Since conventional antenna arrays extract the power efficiently only from the common mode excitation of the array, this ensures that the BMAA can achieve a higher phase enhancement factor compared to a regular array (refer to Fig. 5.1) while providing the same output power level at boresight compared to a regular antenna array. The next subsection outlines the design procedure for obtaining a BMAA that achieves the maximum possible phase enhancement factor without sacrificing any output power.

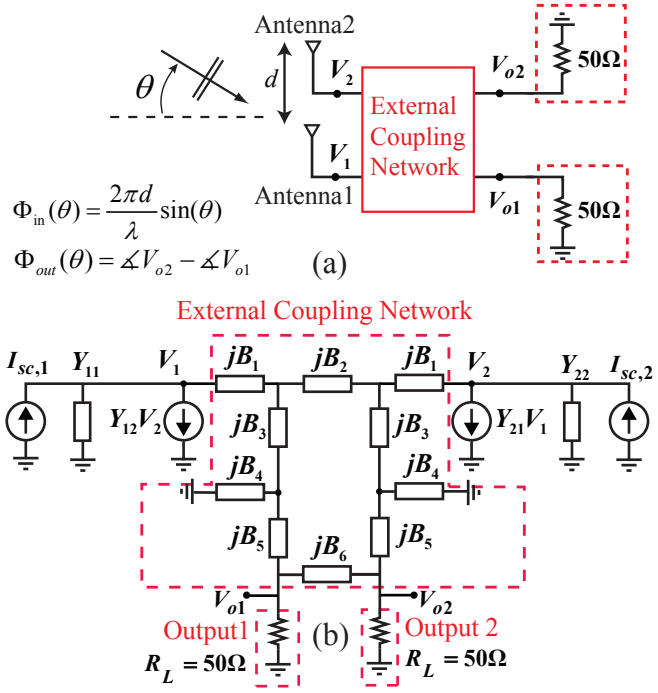

Figure 5.2 (a) Block diagram of a two-element biomimetic antenna array. (b) The equivalent circuit model of the two-element BMAA shown in part (a) and the architecture of its external coupling network are shown.

5.2.2 Optimum BMAA Design

The block diagram of the two-element BMAA is shown in Fig. 5.2(a) and its equivalent circuit model is shown in Fig. 5.2(b). The two antennas are identical and are separated by a distance of $d \ll \lambda$ from each other. A plane wave with an angle-of-incidence of θ is incident on the two antennas, where θ is measured from boresight. The two antennas are modeled with their Norton equivalent circuit models and the mutual coupling between them is modeled using two voltage controlled current sources. A symmetric external coupling network, consisting of reactances $B_1 - B_6$, are placed between the two antenna elements and connected to two load impedances of $R_L = 50\,\Omega$. The short-circuit cur-

rents of the two antenna elements are assumed to have the following dependance on the angle-of-incidence, θ:

$$I_{sc,1} = (1 - c_A \sin(\theta))e^{-jc_\theta \sin(\theta)} \tag{5.1a}$$

$$I_{sc,2} = (1 + c_A \sin(\theta))e^{jc_\theta \sin(\theta)} \tag{5.1b}$$

where the coefficients c_A and c_θ are the slopes of the amplitude and phase of $I_{sc,1}$ with respect to the angle-of-incidence (θ) at boresight, respectively. These coefficients are determined using full-wave EM simulations. Fig. 5.3 plots the normalized magnitudes of the short-circuit currents of the two antennas assuming that the elements are monopole antennas with a length of 13.5 cm and a spacing of 2.5 cm and that they are placed on top of an infinite PEC ground plane. In this case, the frequency of operation is 600 MHz and the results are obtained for a vertically-polarized EM wave incident at different directions along the azimuth plane. For incident angles close to boresight, the expressions for the short-circuit currents can be further simplified to:

$$\begin{aligned} I_{sc,1} &= (1 - c_A\theta)(\cos(c_\theta\theta) - j\sin(c_\theta\theta)) \\ &\approx (1 - c_A\theta)(1 - jc_\theta\theta) \\ &\approx 1 - j\theta(c_\theta - jc_A) \end{aligned} \tag{5.2a}$$

$$I_{sc,2} \approx 1 + j\theta(c_\theta - jc_A) \tag{5.2b}$$

and the common mode and differential mode short-circuit currents can be written as (refer to Fig. 5.4):

$$I_c(\theta) = \frac{I_{sc,2}(\theta) + I_{sc,1}(\theta)}{2} = 1 \tag{5.3a}$$

$$I_d(\theta) = \frac{I_{sc,2}(\theta) - I_{sc,1}(\theta)}{2} = j\theta(c_\theta - jc_A). \tag{5.3b}$$

The BMAA is designed to have the same output power as a regular array composed of the same receiving elements (i.e. the BMAA without the external coupling network

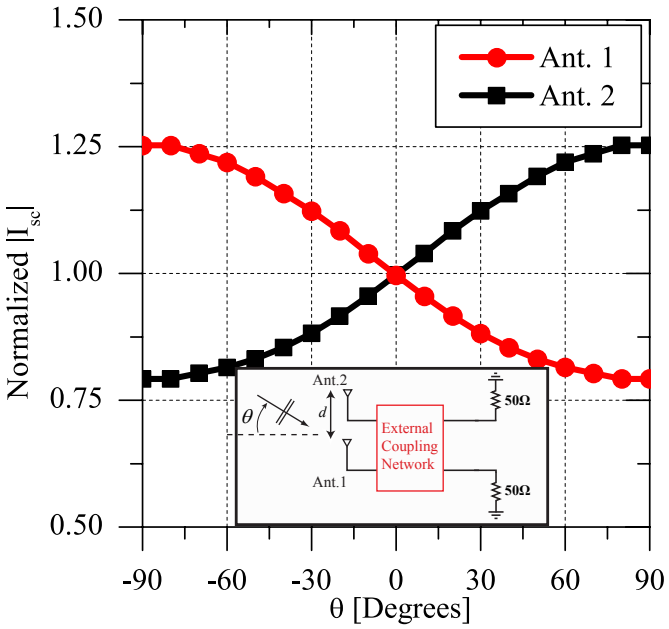

Figure 5.3 Normalized magnitudes of the short-circuit currents of two 13.5 cm long monopole antennas spaced at a distance of 2.5 cm and operating at 600 MHz. The inset shows the definition of positive and negative angles of incidence and the orientation of antennas 1 and 2 with respect to the incident wave.

terminated at matched loads) at boresight. Therefore, the coupling network should match the load impedance ($50\,\Omega$) to the admittance of the antenna array in the common mode (i.e., $Y_{11} + Y_{12}$). Therefore, we must have:

$$Y_{in,c} = (Y_{11} + Y_{12})^*. \tag{5.4}$$

If this condition is satisfied, the input common mode voltage is equal to:

$$V_{in,c} = \frac{I_c}{2G_c} = \frac{1}{2G_c} \tag{5.5}$$

where

$$G_c = G_{11} + G_{12}. \tag{5.6}$$

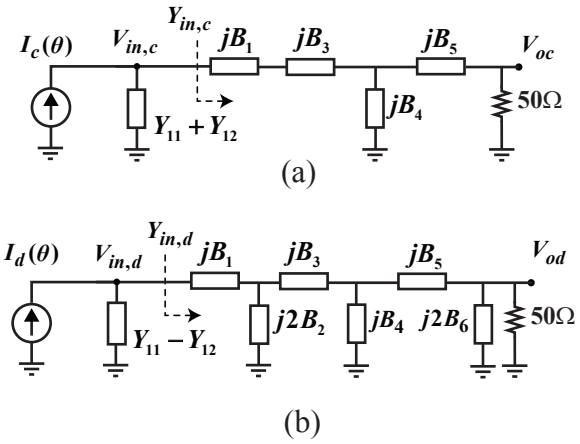

Figure 5.4 The equivalent circuit model of the two-element BMAA shown in Fig. 5.2 in the (a) common mode and (b) differential mode of excitation.

Due to the fact that the external coupling network is lossless, the power delivered to the coupling network is totally dissipated in the load and no power is lost in the coupling network. Moreover, if (5.4) is satisfied, there is maximum power transfer from the antenna to the load and the magnitude of the output common mode voltage is maximized. In other words, matching the antenna in the common mode ensures that the output power is equal to the available power from the antenna. We have:

$$\frac{1}{2}R_L|V_{oc}^{\max}|^2 = \frac{1}{2}G_c|V_{in,c}|^2 = \frac{1}{8G_c} \tag{5.7}$$

and the maximum magnitude of the output common mode voltage can be written as:

$$|V_{oc}^{\max}| = \frac{1}{2}\sqrt{\frac{1}{G_c R_L}}. \tag{5.8}$$

Next, an expression for the phase enhancement factor of the BMAA is derived and a theoretical upper bound for its value is determined. The phase enhancement factor is defined to be $\eta = \frac{s}{s_0}$ where s_0 is the slope of the output phase of a regular array with

respect to the angle of incidence at boresight, i.e.

$$s_0 = \left.\frac{d(\frac{2\pi d}{\lambda}\sin(\theta))}{d\theta}\right|_{\theta=0} = \frac{2\pi d}{\lambda} \tag{5.9}$$

and s is the slope of the output phase, $\Phi_{out} = \measuredangle V_{o2} - \measuredangle V_{o1}$, of the biomimetic array i.e.:

$$s = \left.\frac{d\Phi_{out}}{d\theta}\right|_{\theta=0}. \tag{5.10}$$

The phase enhancement factor is a measure of the enhanced phase sensitivity of the BMAA compared to a regular array. We have:

$$\begin{aligned} s &= \lim_{\theta\to 0}\frac{\measuredangle V_{o2} - \measuredangle V_{o1}}{\theta} = \lim_{\theta\to 0}\left[\frac{1}{\theta}\measuredangle\left\{\frac{V_{oc}+V_{od}}{V_{oc}-V_{od}}\right\}\right] \\ &= \lim_{\theta\to 0}\left[\frac{1}{\theta}\measuredangle\left\{\frac{1+\frac{V_{od}}{V_{oc}}}{1-\frac{V_{od}}{V_{oc}}}\right\}\right] \\ &= \lim_{\theta\to 0}\left[\frac{1}{\theta}\measuredangle\left\{\frac{1+\mathrm{Re}\left\{\frac{V_{od}}{V_{oc}}\right\}+j\,\mathrm{Im}\left\{\frac{V_{od}}{V_{oc}}\right\}}{1-\mathrm{Re}\left\{\frac{V_{od}}{V_{oc}}\right\}-j\,\mathrm{Im}\left\{\frac{V_{od}}{V_{oc}}\right\}}\right\}\right] \\ &= \lim_{\theta\to 0}\left[\frac{2}{\theta}\,\mathrm{Im}\left\{\frac{V_{od}}{V_{oc}}\right\}\right] = \lim_{\theta\to 0}\left[\frac{2}{\theta}\left|\frac{V_{od}}{V_{oc}}\right|\sin(\varphi)\right] \end{aligned} \tag{5.11}$$

where

$$\varphi = \measuredangle V_{od} - \measuredangle V_{oc}. \tag{5.12}$$

Thus for a fixed $|V_{oc}|$, to have the maximum possible phase enhancement η, we must:

- Maximize the output amplitude for the differential mode of excitation. An increase in the differential mode voltage ensures a larger phase enhancement factor, provided that the common mode and the differential mode voltages are not in-phase (have a 0° phase difference).

- Make the phasors V_{oc} and V_{od} orthogonal to each other at boresight.

The upper bound on η can be determined by assuming V_{oc} and V_{od} are orthogonal and maximizing $|V_{od}|$. Similar to the common mode case, to maximize the amplitude of the differential mode output voltage, we must have:

$$Y_{in,\,d} = (Y_{11} - Y_{12})^* \tag{5.13}$$

In other words, matching the antenna in the differential mode ensures that the differential mode output voltage (the voltage at the terminals of the $50\,\Omega$ loads) is the maximum value possible. In this case, the input differential mode voltage is equal to:

$$V_{in,d} = \frac{I_d}{2G_d} = j\theta\frac{c_\theta - jc_A}{2G_d} = \theta\frac{c_A + jc_\theta}{2G_d} \tag{5.14}$$

where

$$G_d = G_{11} - G_{12}. \tag{5.15}$$

The coupling network is lossless, thus we have:

$$\frac{1}{2}R_L|V_{od}^{\max}|^2 = \frac{1}{2}G_d|V_{in,\,d}|^2 \tag{5.16}$$

and the maximum magnitude of the output differential mode voltage at incident angles close to boresight can be written as:

$$|V_{od}^{\max}| = \frac{1}{2}\theta\sqrt{\frac{c_\theta^2 + c_A^2}{G_d R_L}}. \tag{5.17}$$

If $|V_{oc}| = |V_{oc}^{max}|$, the upper bound of the phase enhancement factor can be written as:

$$\eta_{\max} = \frac{2}{s_0}\sqrt{(c_\theta^2 + c_A^2)\,\frac{G_c}{G_d}} = \frac{\lambda}{\pi d}\sqrt{({c_\theta}^2 + c_A^2)\,\frac{G_c}{G_d}} \tag{5.18}$$

It is noted that this expression is only a function of the antenna parameters and does not depend on component values of the external coupling network. As can be seen from (5.18),

the maximum phase enhancement factor that can be obtained increases as the distance between the antenna elements decrease. However, this decreases the bandwidth of the phase enhancement factor, η. Moreover, as the distance between the elements decrease, the available power from the antenna array also decreases (due to the smaller aperture size of the array).

There is a trade-off between the output power level and the phase enhancement factor in a two-element BMAA. A reduction of output power at boresight leads to a higher phase enhancement. In this chapter, however, the goal is to obtain the maximum possible phase enhancement without sacrificing output power. That is why, in calculating the maximum phase enhancement factor, the value of the output common-mode voltage, V_{oc}, is set to the maximum possible value, i.e. the value of V_{oc} when the antennas are connected to matched loads and the available power is extracted from the array. If this condition is relaxed and a lower value of V_{oc} is considered, a higher phase enhancement value can be obtained as can be seen from (5.11).

In summary, to achieve maximum phase enhancement factor, the external coupling network must be designed to match the $50\,\Omega$ load to the common and differential mode source admittances and also make the phasors V_{oc} and V_{od} orthogonal at boresight. These conditions lead to a nonlinear system of five equations with six independent variables $B_1 - B_6$ (two for the real and two for the imaginary parts of the common mode and differential mode impedances and one for the phase condition).

5.3 Experimental verification

The two-element array considered in this chapter consists of two $13.5\,$cm long monopole antennas separated from one another by a distance of $2.5\,$cm. The two-port Y-parameters of the antennas, at the operating frequency of $600\,$MHz, are obtained by simulation and

Table 5.1 Calculated Y-parameters of the two monopole antenna system discussed in Section 5.2 at $600\,\mathrm{MHz}$.

$G_{11} = \mathrm{Re}(Y_{11})$	$4.58\,m\mho$
$G_{12} = \mathrm{Re}(Y_{12})$	$3.98\,m\mho$
$B_{11} = \mathrm{Im}(Y_{11})$	$-6.41\,m\mho$
$B_{12} = \mathrm{Im}(Y_{12})$	$11.89\,m\mho$

presented in Table 5.1. Assuming an infinite ground plane size and an incident vertically-polarized plane wave, the simulated values obtained by full-wave EM simulations for c_A and c_θ are:

$$c_A = 0.193 \tag{5.19a}$$

$$c_\theta = 0.102 \tag{5.19b}$$

There is no guarantee that the nonlinear system of equations discussed in the previous section for finding the global optimum has a solution, or whether the solution yields practical values for the components of the coupling network. Therefore, a numerical procedure was used to find an acceptable sub-optimal solution for component values which results in a practically implementable coupling network. To this end, the antenna was matched to a $50\,\Omega$ load in the common mode and a range of acceptable values which $\varphi = \measuredangle V_{od} - \measuredangle V_{oc}$ can take was specified. The goal of the optimization procedure was to make $|V_{od}|$ as close to $|V_{od}^{max}|$ as possible. As can be seen from (5.11), the phase enhancement factor is proportional to the sine of φ. Thus if the orthogonality condition is relaxed to a 60° phase difference, the phase enhancement factor would only decrease by a factor of $\sin(60) \approx 0.87$ which is a relatively acceptable value. Therefore, the following range was specified for φ:

$$60^\circ \leqslant \varphi \leqslant 90^\circ \tag{5.20}$$

and an optimization tool was used to maximize $|V_{od}|$. The equivalent circuit parameters of the antennas, obtained by full-wave EM simulations, were imported into Agilent's Advanced Design System (ADS) software, which is a circuit simulation tool. Using the equivalent circuit shown in Fig. 5.2(b), five goals based on the five nonlinear equations discussed in the Section 5.2 were defined and the values B_1-B_6 were optimized to yield the maximum possible value for $|V_{od}|$. The reactive elements were defined as generic reactive elements and no prior knowledge of them being a capacitor or an inductor was assumed. The specific optimization routine performed was "random optimization" with a maximum iterations of 16000. The optimization process took 80s to complete on a core i7-870 processor running at 2.93GHz. The component values for the coupling network that are obtained from this optimization procedure are listed in Table 5.2.

Table 5.2 Values for the components of the external coupling network (in mS) obtained from an optimization process.

B_1	33.3
B_2	22.2
B_3	-10.2
B_4	10.0
B_5	-20.4
B_6	-14.0

These values result in

$$|V_{od}| = 0.93\,|V_{od}^{\max}| \tag{5.21}$$

$$\varphi \approx 60^{\circ}. \tag{5.22}$$

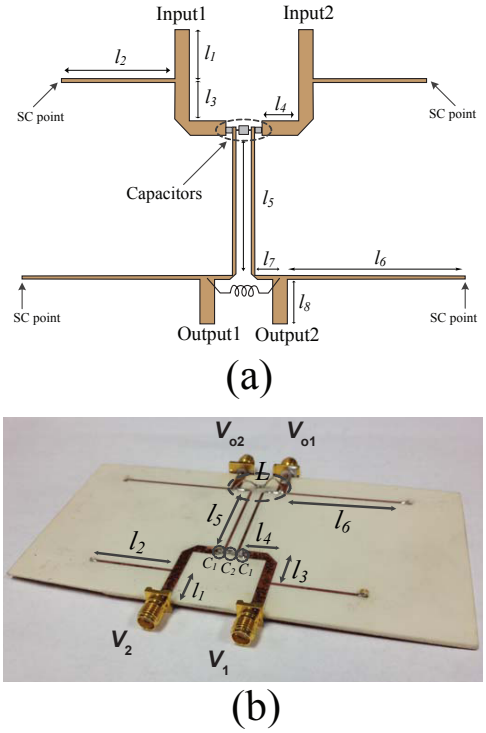

Figure 5.5 (a) Topology of the modified external coupling network. (b) Photograph of the fabricated two-input two-output external coupling network. $C_1 = 3.6$ pF, $C_2 = 6.2$ pF, and $L \approx 19$ nH. Thickness of thick and thin lines are respectively 3.36 mm and 0.8 mm (refer to Fig. 5.2 for port naming conventions).

Using (5.11) and (5.17)-(5.18), we have:

$$\eta = \frac{s}{s_0} = 0.93 \sin(\varphi)\eta_{\max} = 4.2 \tag{5.23}$$

where $\eta_{\max} = 5.2$. Therefore, when these element values are used in the external coupling network shown in Fig. 5.2, we expect to achieve a phase enhancement factor of roughly 80% of the maximum theoretical value.

The four-port external coupling network must have specific scattering parameters to have the desired performance including maximum phase enhancement and output power at 600 MHz. This can easily be realized using reactive lumped elements. This network

is to be connected to the two ports of the BMAA. Since these two ports are 2.5 cm apart from each other, the external coupling network must be modified such that it fits in the 2.5 cm spacing and still provides the same scattering parameters. To do so, a distributed coupling network composed of microstrip lines etched on the dielectric substrate and three lumped capacitors is designed and fabricated to cover the spacing and maintain the S-parameters obtained from the optimization procedure. Fig. 5.5(a) shows the topology of this modified external coupling network and Fig. 5.5(b) shows a photograph of a fabricated prototype. The values of the transmission line lengths and characteristic impedances of the different transmission lines used in this external coupling network are provided in Table 5.3. Reactance B_6 is implemented by a lumped inductor with a value of $L \approx 19$ nH.

Table 5.3 Length and characteristic impedances of the different transmission lines used in the coupling network.

l_1	1.11 cm	w_1	3.36 mm	50 Ω
l_2	2.57 cm	w_2	0.8 mm	100 Ω
l_3	8.42 cm	w_3	3.36 mm	50 Ω
l_4	0.79 cm	w_4	3.36 mm	50 Ω
l_5	3.32 cm	w_5	0.8 mm	100 Ω
l_6	4.0 cm	w_6	0.8 mm	100 Ω
l_7	0.35 cm	w_7	0.8 mm	100 Ω
l_8	1.0 cm	w_8	3.36 mm	50 Ω

The inductor is implemented using a short piece of wire, as shown in Fig. 5.5(b) and its inductance is measured using a vector network analyzer. In this design, Rogers RO4003C with the dielectric constant of $\epsilon_r = 3.55$ and a thickness of 60 mils is used as the substrate. The two monopole antennas are made out of hollow copper tubes with a circular cross

section with inner and outer radii of 1.8 mm and 2.4 mm, respectively, and mounted on a brass ground plane with physical dimensions of 60 cm $\times$ 60 cm. To minimize the impact of the scattering and diffraction from the edges of the finite ground plane on the BMAA response, the edges of the ground plane are covered with thin absorbers (6.35 mm thick ECCOSORB LS-30/SS-3 absorbers manufactured by Emerson $\&$ Cuming).

Fig. 5.6 shows the measured and simulated output phase responses of this BMAA as a function of the angle of incidence and compares it with that of a regular array with the same elements and dimensions. The simulations are done using CST Microwave Studio (for the monopole antennas on the infinite ground plane) and Agilent ADS (for the coupling network). As can be seen, the asymmetries in the coupling network have shifted the zeros crossing of the phase from boresight to $\theta \approx 5^{\circ}$. However, there is generally a good agreement between the simulated and measured results. The measured phase enhancement factor at boresight is $\eta \approx 3.3$. The main reason for the slight discrepancy between the measured phase enhancement at boresight and the simulated value of $\eta = 4.2$ is attributed to component tolerances and the asymmetries in the coupling network that have resulted in the shift of boresight. Fig. 5.7 shows the measured and simulated power levels at the two BMAA outputs normalized to the output power level achieved from a regular antenna array (i.e. BMAA without the coupling network). As expected, the simulated output power at the two ports of the BMAA is equal to that of a regular array. The measured output power at boresight is $P_{out} = -0.1$ dB at port 2 and $P_{out} = -0.7$ dB at port 1. The differences between the measured and simulated values for the normalized output power can be primarily attributed to the asymmetries in the coupling network and also lossy components (in our design procedure, the components were taken to be lossless) as described extensively in [55]. Other factors that contribute to the differences observed between the measurement and the simulation results include the tolerances of the component values of the capacitors and inductor, the slight asymmetries that may exist in the fabricated two-element antenna

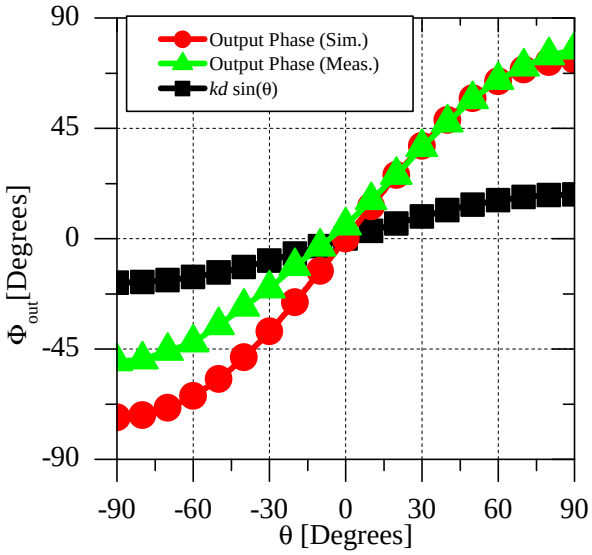

Figure 5.6 Measured and simulated output phase responses of the two-element BMAA discussed in Section 5.2 as well as the phase response corresponding to the propagation of an electromagnetic wave over a distance of d at an angle of θ.

array and its external coupling network, potential measurement uncertainties, and the finite dimensions of the ground plane (which were assumed to be infinite in the simulations).

5.4 Application in Designing Directive End-fire Antenna Arrays

The optimum BMAA introduced in this chapter can be used to design a two-element, end-fire array with a moderate superdirectivity (i.e., the directivity of this array is larger than that of a regular array occupying the same aperture). The architecture of such an array is shown in Fig. 5.8 where the external coupling network is followed by a 180° hybrid which extracts the common mode and differential mode outputs of the BMAA. After phase shifting the differential mode by 90°, the signals are added. The resultant measured and simulated power at the output of this end-fire array are normalized to the measured

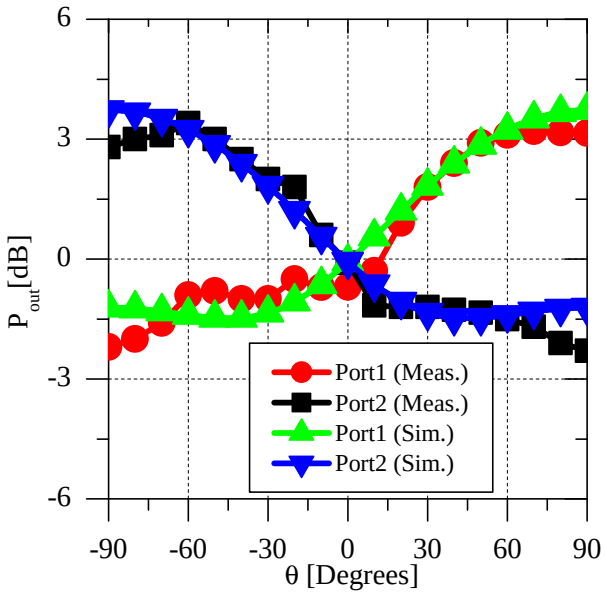

Figure 5.7 Measured and simulated amplitude responses of the two-element BMAA discussed in Section 5.2. Port 2 is the output closer to the incident wave (the ipsilateral antenna) and port 1 is the output further from the incident EM wave (the contralateral antenna).

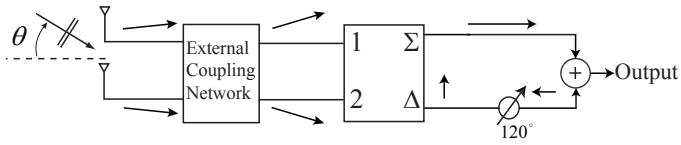

Figure 5.8 Block diagram of a two-element end-fire array based on the BMAA presented in this chapter.

and simulated output power of a regular array at boresight respectively and plotted as a function of angle of incidence in Fig. 5.9. The normalized simulated output power from a regular array (the same antennas with the same spacing) along with the hybrid and phase shifter has also been plotted for comparison. As can be seen, the two-element BMAA with

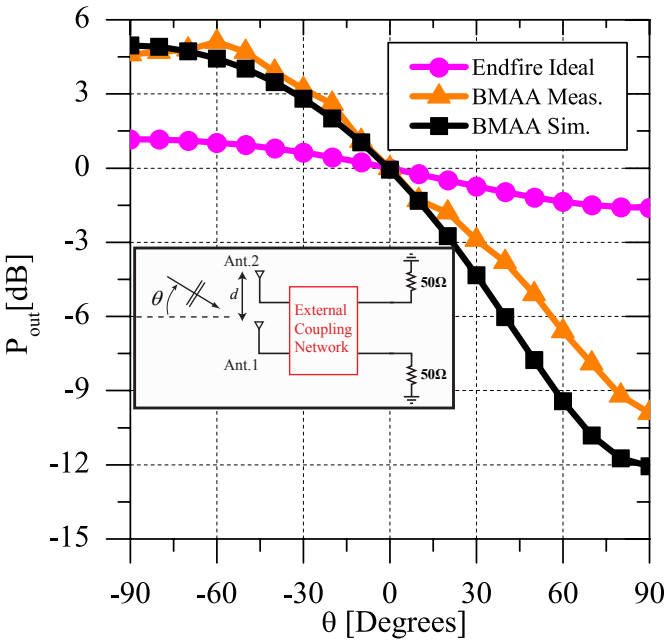

Figure 5.9 Normalized output power at the output of the end-fire array shown in Fig. 5.8 and a regular array followed by a 180° hybrid and phase shifter (the structure shown in Fig. 5.8 without the external coupling network of the BMAA).

optimum power extraction and moderate phase enhancement factor can be used to design a moderately super-directive end-fire antenna array.

5.5 Conclusions

A new architecture for two-element biomimetic antenna arrays was presented. Using this design, a theoretical upper limit for the phase enhancement factor of a given two-element BMAA is obtained, which ensures that the output power of the array is not reduced compared to a conventional antenna array occupying the same aperture dimensions. A methodology for the design of a coupling network that can achieve this upper bound is

outlined and based on that a prototype was designed, fabricated, and experimentally characterized. It was experimentally demonstrated that the new design does not have the main drawback of the previously-reported BMAAs. Namely, the degradation of received signal power to achieve an enhanced output phase sensitivity. Since this new antenna extracts maximum available power from both the common and the differential modes of excitation of the array, it can also be used to design end-fire antenna arrays with moderate superdirectivity. This new two-element array is expected to find applications in systems where a small aperture area is available to accommodate the array but enhanced angular resolving capabilities or directionality from the array is expected (e.g., small aperture direction finding systems). Therefore, the proposed design can have applications in long-range small-aperture direction finding systems.

Chapter 6

Bandwidth Enhancement of Biomimetic Antenna Arrays using Non-Foster Coupling Networks

6.1 Introduction

Biomimetic antenna arrays (BMAAs) have been previously introduced [55]-[57]. They offer enhanced angular resolution compared to regular antenna arrays and can potentially have applications in miniature direction finding systems, small aperture imaging systems and wireless communication systems. A drawback of previously designed BMAAs is that the enhanced angular resolution occurs in a relatively narrow bandwidth which is undesirable in many applications where bandwidth is crucial. To improve the bandwidth, one can resort to more complicated passive multi-section design techniques similar to the techniques used in wideband filter design. However, more reactive elements leads to more loss in the external coupling network and consequently degradation of received signal power.

A possible method for obtaining a higher bandwidth is the use of non-Foster elements, i.e. elements that violate Foster's reactance theorem, in the network. Non-Foster elements have been previously used in wideband impedance matching of small antennas [62]-[66]. The motivation behind this approach is that the input impedance of a typical electrically small antenna has a small resistive and a large frequency-varying reactive component. Therefore, conventional matching techniques based on passive lumped elements result in

a very narrow impedance bandwidth. To overcome this issue, non-foster matching circuits, have been proposed, which cancel the reactive part of the antenna input impedance over a wide frequency band, thereby increasing the impedance bandwidth of the antenna. For example, the input impedance of an electrically small dipole consists of a small resistance in series with a capacitor. The technique implements a negative capacitor of the size as seen looking into the antenna terminals, thereby cancelling the the reactive part of the input impedance seen by the source. Non-foster matching circuits typically use negative impedance converters, which employ positive feedback [62].

In this chapter, non-foster elements have been employed in the external coupling network of a BMAA consisting of electrically small antenna elements to cancel the reactive part of the antenna impedance in the common and differential modes, thereby increasing the bandwidth over which a considerable phase enhancement factor may be obtained. The proposed technique has been verified by comparing the non-Foster BMAA to a passive BMAA designed using previously reported techniques and with the same characteristics.

6.2 Design Procedure

The block diagram of a two-element biomimetic antenna array is shown in Fig. 6.1. A plane wave with an angle-of-incidence of θ is incident on the two antennas, where θ is measured from boresight. The outputs of the antennas ($x_1,\ x_2$) are fed to the two inputs of an external coupling network. This coupling network takes the two input signals, x_1 and x_2, with a phase difference of $\Phi_{in}(\theta)$ between them and converts them to two output signals, y_1 and y_2, with a considerably larger phase difference of $\Phi_{out}(\theta)$. To quantify this,

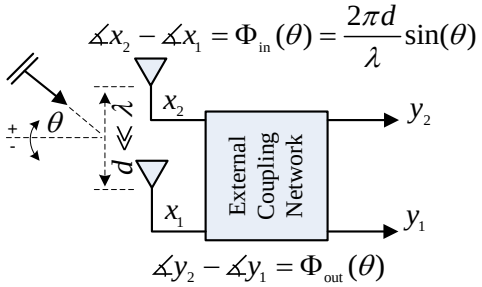

Figure 6.1 Block diagram of a two-element regular antenna array (BMAA).

the phase enhancement factor is defined as $\eta = \frac{s}{s_0}$, where

$$s = \left.\frac{d\Phi_{out}}{d\theta}\right|_{\theta=0}$$
$$s_0 = \left.\frac{d\Phi_{in}}{d\theta}\right|_{\theta=0} = \frac{d}{d\theta}\left(2\pi\frac{d}{\lambda}\sin(\theta)\right)\Bigg|_{\theta=0} = 2\pi\frac{d}{\lambda}\,.$$

The antenna array discussed in this chapter is a two-element monopole array. The elements are located on an infinite ground plane, have a length of 5 cm, and are spaced 2.5 cm apart. This structure is simulated in CST Microwave Studio and the two-port Y-parameters of the antennas, at the frequency of 500 MHz, are obtained and presented in Table 6.1.

To compare the performance of the non-Foster coupling network proposed in this chapter with previous designs, a passive coupling network based on the procedure outlined in [56] is also designed. Fig. 6.2 shows the maximum phase enhancement factor that can be obtained from the two-element antenna array as a function of normalized output power at 500 MHz when the incident wave arrives from boresight (i.e., $\theta = 0$). In this figure, the output power of the two-element BMAA is normalized to the power available from each array element at boresight, P_0, where

$$P_0 = \frac{1}{8(G_{11} + G_{12})}$$

Table 6.1 Simulated Y-parameters of the two-element array discussed in Section 6.2 at 500 MHz. The monopoles have a length of 5cm and are spaced 2.5cm apart. Values are in mS.

$G_{11} = \mathrm{Re}(Y_{11})$	0.047
$G_{12} = \mathrm{Re}(Y_{12})$	0.046
$B_{11} = \mathrm{Im}(Y_{11})$	13.6
$B_{12} = \mathrm{Im}(Y_{12})$	-0.57

assuming unity amplitude short-circuit currents. The maximum phase enhancement factor at a normalized output power level of -3 dB is roughly 6.4. Therefore, the passive coupling network is designed to have $\eta = 6$ and $P_{out}^{n} = -3$ dB. The circuit implementation of the passive coupling network is shown in Fig. 6.3(a)[1].

For comparison, the non-Foster coupling network is designed to have the same phase enhancement factor and output power values as the passive coupling network and its topology is shown in Fig. 6.3(b). Due to the fact that the antennas are small at the frequency of 500 MHz (the length of each monopole antenna is $\lambda/12$), the equivalent circuit model of the antennas can be approximated with a capacitor in parallel with a radiation resistance [62]. Using Table 6.1, the equivalent circuit models of the antenna array in the common and the differential modes are obtained and shown in Fig. 6.3(c) and Fig. 6.3(d), respectively. Here, we have assumed that the short-circuit currents of the antennas are $I_{sc,1} = e^{j\alpha}$ and $I_{sc,2} = e^{-j\alpha}$ where $\alpha = \pi d \sin(\theta)/\lambda$ and d is the distance between the antennas. At angles close to boresight, the common- and differential-mode antenna short-circuit currents

[1]The reader is referred to [56] for details of the design procedure.

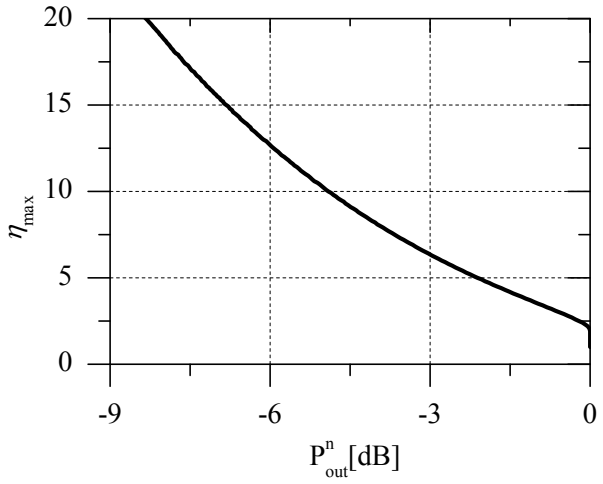

Figure 6.2 Variation of the maximum phase enhancement factor as a function of the normalized output power for the two-element BMAA discussed in this chapter. This curve is obtained for the antenna array whose Y-parameters are provided in Table 6.1.

can be written as:

$$I_c(\theta) = \frac{I_{sc,1}(\theta) + I_{sc,2}(\theta)}{2} \approx 1$$
$$I_d(\theta) = \frac{I_{sc,2}(\theta) - I_{sc,1}(\theta)}{2} \approx j\alpha$$

The imaginary parts of the common-mode and the differential-mode admittances of the antennas are equal to $B_c = j(13.6-0.57) = j13.03$ mS and $B_d = j(13.6+0.57) = j14.17$ mS, respectively. These values correspond to capacitors with values of $C_c \simeq 4.14$ pF and $C_d \simeq 4.51$ pF at 500 MHz. To obtain a broadband match in the common and the differential modes, the non-Foster coupling network should cancel the common- and the differential-mode capacitances of the antenna array. This can be seen by examining the common- and the differential-mode equivalent circuit models of the non-Foster BMAA shown in Figs. 6.3(c) and 6.3(d). Thus, we have:

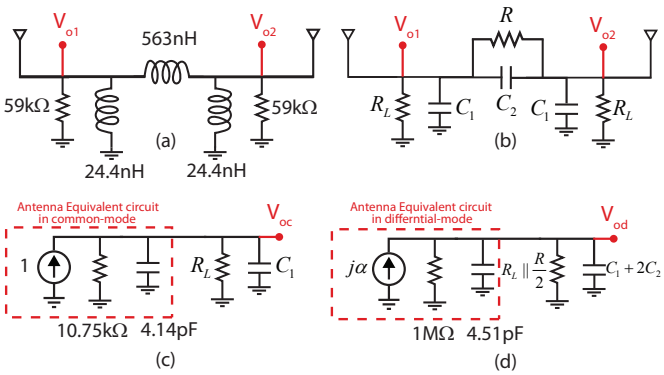

Figure 6.3 Circuit implementation of the coupling networks discussed in this chapter. a) Passive. b) Non-Foster. c) Common-mode equivalent circuit of non-Foster BMAA at 500 MHz. d) Differential-mode equivalent circuit of non-Foster BMAA at 500 MHz ($\alpha = \pi \frac{d}{\lambda} \sin(\theta)$).

$$C_1 = -C_c = -4.14\,\text{pF}$$

$$\text{C}_1 + 2C_2 = -C_d = -4.51\,\text{pF} \Rightarrow \text{C}_2 = -0.185\,\text{pF}$$

Similar to the imaginary part of the input admittance, the real part of the common and differential-mode admittance of the antenna array is equal to $G_c = 0.047 + 0.046 = 0.093$ mS and $G_d = 0.047 - 0.046 = 0.001$ mS, respectively. The power delivered to the load resistance R_L at boresight can be obtained using the common-mode circuit of Fig. 6.3(c) and it is equal to[2]:

$$P_L = \frac{1}{2} R_L \left(\frac{R_c}{R_c + R_L} \right)^2$$

where $R_c = 1/G_c = 10.75$ kΩ. The power available from the array at boresight at 500 MHz is equal to $P_0 = \frac{R_c}{8}$. Therefore, to obtain a normalized output power of -3 dB (0.5 in linear scale), R_L must satisfy:

$$\frac{1}{2} R_L \left(\frac{R_c}{R_c + R_L} \right)^2 = 0.5 \frac{R_c}{8}$$

[2]Assuming the reactive part of the antenna admittance is canceled by the coupling network.

This equation has two solutions for R_L of which we arbitrarily choose $R_L = 1.85$ kΩ[3].

Next, the value of R that yields a phase enhancement factor of $\eta = 6$ is determined. The phase enhancement factor can be written as:

$$\begin{aligned}\eta &\triangleq \lim_{2\alpha\to 0}\left[\frac{\measuredangle V_{o1} - \measuredangle V_{o2}}{2\alpha}\right] = \lim_{2\alpha\to 0}\left[\frac{1}{2\alpha}\measuredangle\left\{\frac{1+j\alpha\frac{V_d}{V_{oc}}}{1-j\alpha\frac{V_d}{V_{oc}}}\right\}\right] \\ &= \lim_{2\alpha\to 0}\left[\frac{2}{2\alpha}\tan^{-1}\left(\frac{\alpha\,\mathrm{Re}\left\{\frac{V_d}{V_{oc}}\right\}}{1-\alpha\,\mathrm{Im}\left\{\frac{V_d}{V_{oc}}\right\}}\right)\right] \\ &= \mathrm{Re}\left\{\frac{V_d}{V_{oc}}\right\}\end{aligned}$$

where $V_{od} = j\alpha V_d$. Using Fig. 6.3(c) and Fig. 6.3(d) and assuming that the reactive part of the antenna admittance is canceled in the common and the differential mode by the coupling network, η can be written as:

$$\eta = \frac{R_d||R_L||\frac{R}{2}}{R_c||R_L} \approx \frac{R_L||\frac{R}{2}}{R_L||R_c}$$

where $R_d = 1/G_d = 1$ MΩ. The reader can easily verify that a $R = -4.6$ kΩ yields $\eta = 6$. This concludes the determination of the values for the ideal non-Foster coupling network shown in Fig. 6.3(b).

6.3 Practical Implementation

Next, the non-Foster elements were designed using a negative impedance converter (NIC) with the specific topology shown in Fig. 6.4 using transistor-based circuits found in [63]-[64]. Fig. 6.5(a) and (b) show the transistor based implementation of the $C_1 = 4.14$ pF capacitor and the parallel combination of the $R = -4.6$ kΩ and $C_2 = 0.185$ pF with the accompanying bias circuitry, respectively. The Infineon BFP620F SiGe bipolar transistor SPICE model was imported and the circuit simulations for the non-Foster elements were

[3]The other solution is $R_L = 62.66$ kΩ.

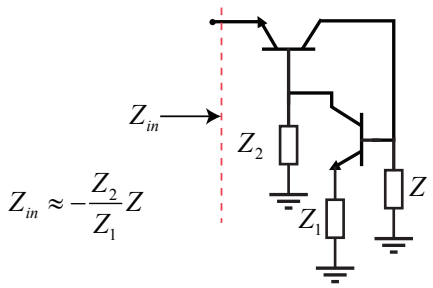

Figure 6.4 Negative impedance converter (NIC) topology employed for implementing the non-Foster components in this chapter.

done in Agilent ADS. To validate the implementation, the admittance of these circuits have been compared to the admittance of ideal negative valued circuit components in Fig. 6.6. Due to the parasitic effects of the transistor, some tuning was carried out to match the admittance of the transistor-based implementations and their ideal-circuit-element counterparts. As can be seen, the real and imaginary parts of the admittance agree well over the frequencies of interest. The response of the non-Foster BMAA using both an idealized and a practically-realizable non-Foster external coupling network was simulated.

Fig. 6.7(a) and 6.7(b) compare the phase enhancement factor and the normalized output power of the three implementations. As can be seen, the passive and the non-Foster circuits have a phase enhancement factor of $\eta = 6$ and a normalized boresight output power level of $P_{out}^{n} = -3$ dB at 500 MHz. Furthermore, the 3-dB bandwidth of the phase enhancement factor for the ideal non-Foster implementation is roughly 33 times that of the passive implementation. Also, the transistor-based non-Foster implementation of the coupling network achieves the same output power level with an $\eta = 6.6$ at 500 MHz. The discrepancy between the phase enhancement factor of the the ideal non-Foster implementation and the transistor implementation is due to the fact that the admittance values associated with the two implementations are designed to match at 500 MHz and are slightly different at other frequencies (refer to Fig. 6.6).

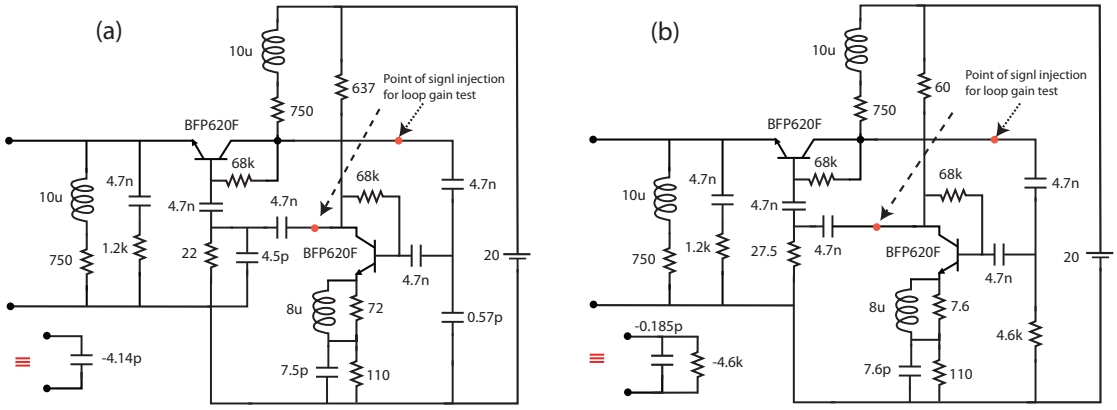

Figure 6.5 Transistor implementation of the non-Foster elements. a) -4.14 pF capacitor. b) -4.6 kΩ resistor in parallel with a -0.185 pF.

The stability of the proposed transistor-based implementation is investigated using Agilent ADS. A signal is injected in the feedback loop of the circuits shown in Fig. 6.5 at the indicated points using the Oscport element and the complex loop gain (magnitude and phase) is calculated with the harmonic balance simulation controller. The simulation parameters are adjusted so that simulator searches for oscillation within 5 octaves of center frequencies from 100 MHz to 1 GHz in 100 MHz increments and the stability of the transistor-based non-Foster BMAA is verified.

6.4 Conclusions

A BMAA with a non-Foster external coupling network has been designed and compared to a passive BMAA with the same phase enhancement factor and output power level. It is shown that the phase enhancement factor of the BMAA with non-Foster elements has roughly 33 times the bandwidth of its passive counterpart. A practical implementation of

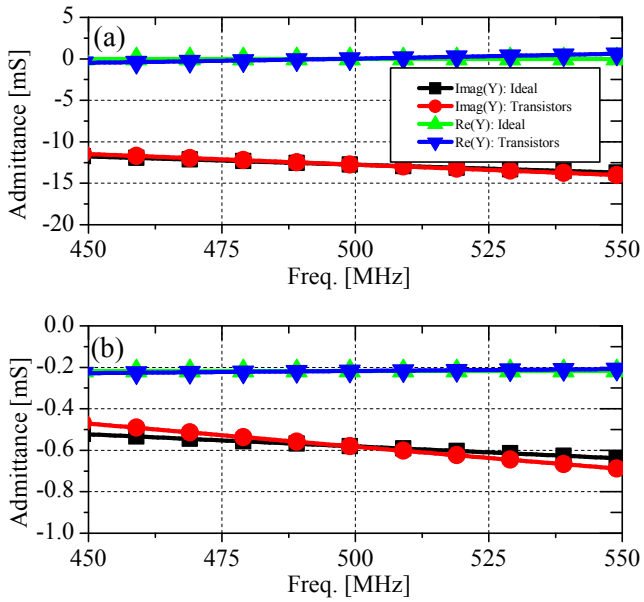

Figure 6.6 Comparison of the real and imaginary parts of the admittance of the non-Foster elements with their corresponding circuit implementations using transistors. a) -4.14 pF capacitor. b) -4.6 kΩ resistor in parallel with a -0.185 pF capacitor.

the non-Foster coupling network with transistors was also introduced and its phase enhancement factor and output power level was compared to that of its ideal-circuit-element counterpart.

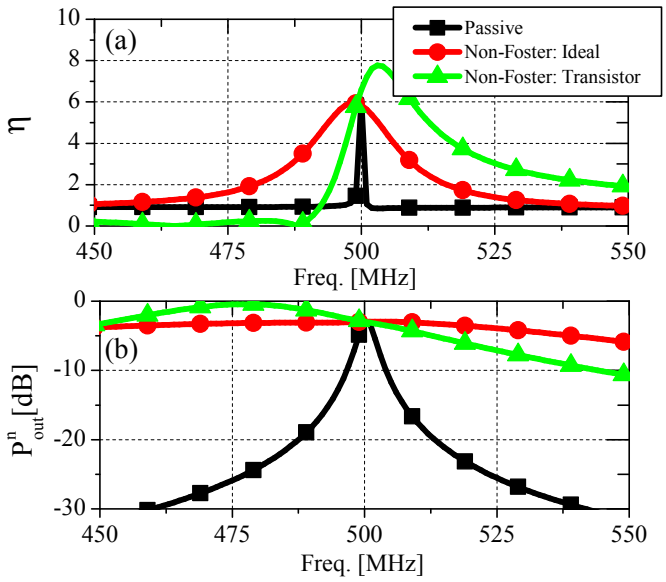

Figure 6.7 a) Phase enhancement factor as a function of frequency for the three different circuit implementations of the coupling network. b) Normalized output power as a function of frequency. The power is normalized to the available power from the antenna array at 500 MHz.

Chapter 7

Biomimetic Nano-Antenna Arrays: A Concept for Designing Sub-Wavelength Angle-Sensing Detectors at Optical Wavelengths

7.1 Introduction

Despite having two closely spaced ears (with a spacing of $\lambda_s/140$, where λ_s is the wavelength of the sound), the parasitoid fly *Ormia Ochracea* has hyperacute directional hearing capabilities and can precisely determine the direction of arrival of a sound wave of interest with a 1°-2° angular resolution [44]-[45]. Therefore, the auditory system of *Ormia Ochracea*, acts as a sub-wavelength, angle-sensing acoustic detector. Recently, we have investigated the analogies between the auditory system of *Ormia Ochracea* and antenna arrays composed of two [55]-[56] or more [57] elements. We have demonstrated that such an antenna array, while occupying an extremely sub-wavelength aperture dimensions, demonstrate significant sensitivity to the angle of incidence of an electromagnetic wave. Therefore, these arrays can be used as sub-wavelength, angle sensing detectors for electromagnetic waves. At RF/microwave frequencies, such antenna arrays are expected to be useful in scenarios where the physical size of the aperture is small but angle-sensing capabilities are desired. One method for conducting angle sensing in a two-element BMAA is to perform phase coherent measurements at the two outputs of the array and use the output phase contrast to determine the angle of arrival of the electromagnetic wave. However,

a two-element BMAA can be designed to allow for angle sensing without the need for conducting coherent measurements at its output. This technique is expected to be useful in situations where conducting coherent measurements is not practical and is expected to be praticularly useful at frequency bands in the sub-millimeter-wave range or higher.

In this paper, we expand the concept of biomimetic antenna arrays to frequency bands outside of the RF/microwave range and present the design of a two-element nano-antenna array with sub-wavelength dimensions. We will demonstrate how the proposed nano-antenna array can act as a sub-wavelength angle-sensing optical detector without requiring any coherent measurements (i.e., using amplitude detectors only). Therefore, at frequency bands where conducting coherent measurements is not straight forward (e.g. sub-millimeter wave, infrared, and optical frequencies), the proposed sub-wavelength detectors and arrays of such detectors offer a new transduction mechanism that can enable the detection and characterization of properties of the incoming electromagnetic wavefront beyond the commonly-measured irradiance. These include detection of the angle of arrival, spectral distribution, and the state of polarization of the wave at the single pixel level with a sub-wavelength spatial dimension.

In what follows, the principles of operation of the proposed nano-antenna array along with simulation results demonstrating the performance of the structure will be presented and discussed.

7.2 Sub-wavelength Nano-Antenna Arrays: Design and Principles of Operation

The phase enhancement characteristics of a two-element BMAA have been studied extensively [55]-[56]. Compared to a regular antenna array of the same aperture size, the two-element BMAA provides an enhanced phase resolution. This enhanced resolution can

be used to detect the direction-of-arrival of an incident wave with a higher degree of accuracy compared to that of a conventional array. The main challenge at frequencies in the THz, infrared, and visible range is the impracticality of performing phase measurements at the two outputs of the BMAA.

Therefore, the two-element BMAA designs reported previously, which relied on phase measurements, cannot be directly used to design sub-wavelength, angle-sensing detectors at optical wavelengths. This problem can be circumvented by transforming the phase-contrast enhancement capabilities of a two-element BMAA to amplitude-contrast enhancement capabilities. This will allow us to use amplitude detection at the outputs of the two-element BMAA and extract useful information about the angle of arrival (AoA) of the electromagnetic wave from the ratio of the extracted output powers at the two ports. This can be accomplished by introducing asymmetry in the array.

In this case, the array can be designed such that the ratio of the power absorbed by the two elements (absorption ratio) becomes a strong function of the incidence angle of an incoming electromagnetic wave. This can be used as a method to determine the angle of arrival of the wave without requiring any phase measurement.

Since good electric conductors are not readily available at optical frequencies, the antenna elements are designed with dielectrics. Each dielectric waveguide is made of silicon. The real and imaginary parts of the dielectric constant of silicon at wavelengths of interest is plotted in Fig. 7.1 [67]. Fig. 7.2(a) shows the cross sectional view of a potential implementation of the angle-sensing optical detector proposed in this work. In this case, the structure is composed of two coupled leaky wave optical antennas. Each leaky-wave optical antenna is in the form of a dielectric waveguide with a rectangular cross section.

A thin layer of silicon dioxide separates the two antennas from the substrate underneath. The array is illuminated by a vertically polarized electromagnetic (EM) plane wave with an angle of incidence of θ.

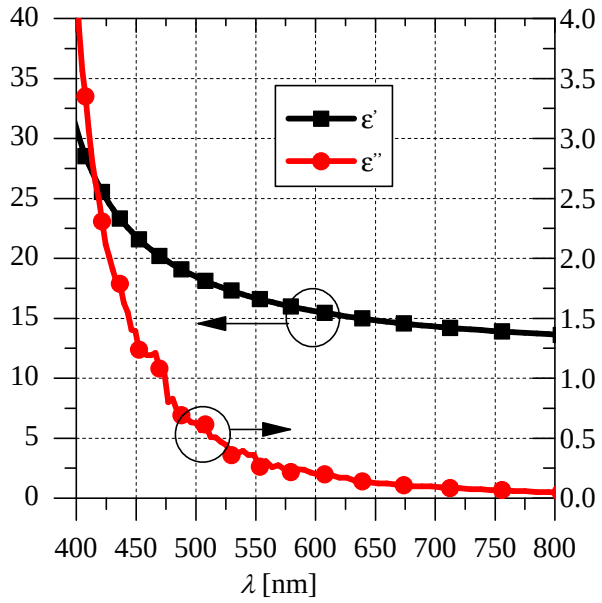

Figure 7.1 Permittivity of silicon at optical wavelengths.

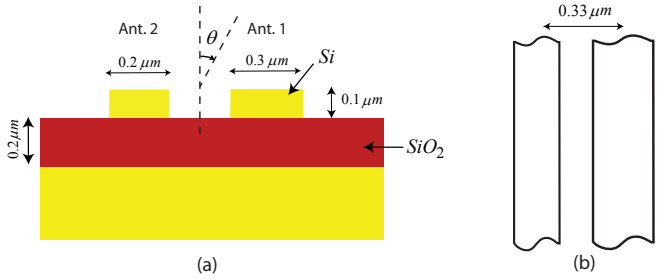

Figure 7.2 (a) Cross sectional view of the asymmetric optical antenna elements located on top of a silicon substrate. (b) Top view of the structure showing dimensions. A thin layer of silicon dioxide is placed between the antenna elements and the silicon substrate. Silicon and silicon dioxide are shown with green and red, respectively.

7.3 Simualtion Results

The structure shown in Fig. 7.2 is simulated using the time domain solver of CST Microwave Studio with the silicon permittivity shown in Fig. 7.1. The larger waveguide has

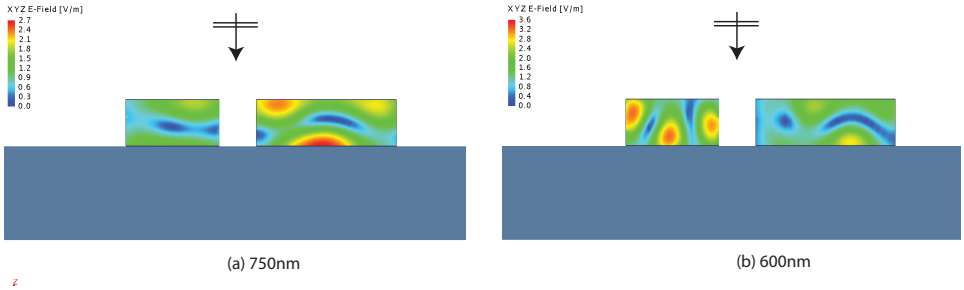

Figure 7.3 Magnitude of electric field distribution in the cross sections of the two asymmetric optical antenna elements at two different wavelengths. The structure is illuminated with a plane wave with a transverse electric polarization and an angle-of-incidence of $\theta = 0$.

cross sectional dimensions of $0.3\mu m \times 0.1\mu m$ and the smaller one has a cross sectional dimensions of $0.2\mu m \times 0.1\mu m$. The antennas are separated by a distance of $0.33\mu m$. In this simulation, the length of both waveguides are assumed to be infinite. This assumption is reasonable in the simulations because the loss of the waveguides (due to their conductivity and also due to radiation) ensures that the response of the infinite structure will be similar to that of the finite structure with a relatively large electrical length (a few tens of micrometers at these wavelengths). In this simulation, the antennas are excited with a plane wave arriving at normal incidence angle ($\theta = 0$) and the induced current and hence power absorbed by each element per unit length is calculated as a function of the wavelength of the incident wave. The electric field distribution at the cross sections of the elements are illustrated in Fig. 7.3 for two different wavelengths. The absorption ratio, i.e. the ratio of the power absorbed by the two elements per unit length for this structure is plotted in Fig. 7.4. As can be seen, the absorption ratio has a dynamic range of roughly 10dB over the wavelengths of interest. Moreover, there is a one to one correspondence between absorption ratio and frequency. Therefore, this structure can be possibly used as a frequency sensing detector at optical wavelengths.

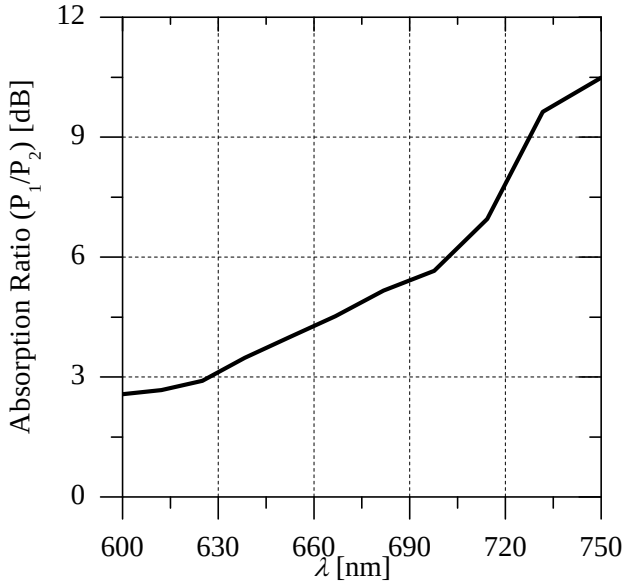

Figure 7.4 Ratio of the power absorbed (dissipated) at the cross sections of the two asymmetric elements as a function of the wavelength.

Next the angular sensing capabilities of the optical detector is studied. In this simulation, the antennas are excited with plane waves arriving from different angles of incidence and the power absorbed by each of the waveguides is calculated. As can be seen in Fig. 7.5, the structure is symmetric in this case. The two waveguides have cross sectional dimensions of $0.2\mu m \times 0.2\mu m$ and are separated by a distance of $0.33\mu m$. As the angle of incidence of the EM wave is changed, the electric field intesity at the cross section of the antennas is calculated and plotted for four different angles of incidence in Fig. 7.6. Observe that the electric field distribution in each waveguide is a strong function of the incidence angle. Also, the ratio of the power absorbed by the two elements per unit length, as a function of angle-of-incidence, is calculated from full-wave EM simulations and the result is plotted in Fig. 7.7. The wavelength of operation is 650 nm. As expected from the

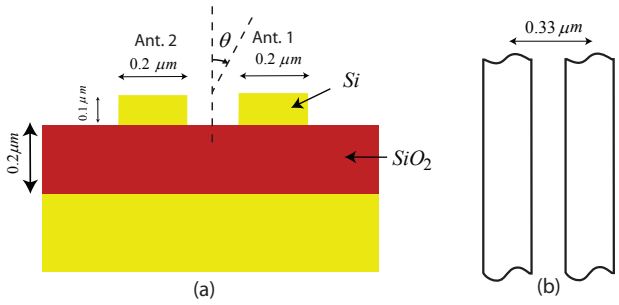

Figure 7.5 (a) Cross sectional view of the symmetric optical antenna elements located on top of a silicon substrate. (b) Top view of the structure showing dimensions.

symmetry of the antenna array, the absorption ratio is 0 dB at boresight. Notice that when a light wave with the appropriate wavelength is incident on this device, dc currents will be induced in each waveguide (because of the semiconducting nature of the coupled waveguides). Therefore, the structure essentially acts as a direct detector where the intensity of the incident electromagnetic wave is converted to a direct current that flows between the input and output of each of the waveguides and can be measured directly. As can be seen from Fig. 7.7, the absorption ratio of the structure has roughly 8 dB dynamic range as the angle-of-incidence changes from -90 to 90 degrees.

7.4 Conclusion

A two-element biomimetic nano-antenna array, which can act as a sub-wavelength angle-sensing optical detector is proposed. Simulation results demonstrate that, despite their sub-wavelength lateral dimensions, such detectors can be designed to demonstrate significant output amplitude variations as a function of the angle of incidence and wavelength of light in their cross-sectional planes. The proposed concept of asymmetric biomimetic nano-antenna array can be used in designing optical detectors that can detect and characterize certain properties of the incoming EM wavefront beyond its irradiance, including

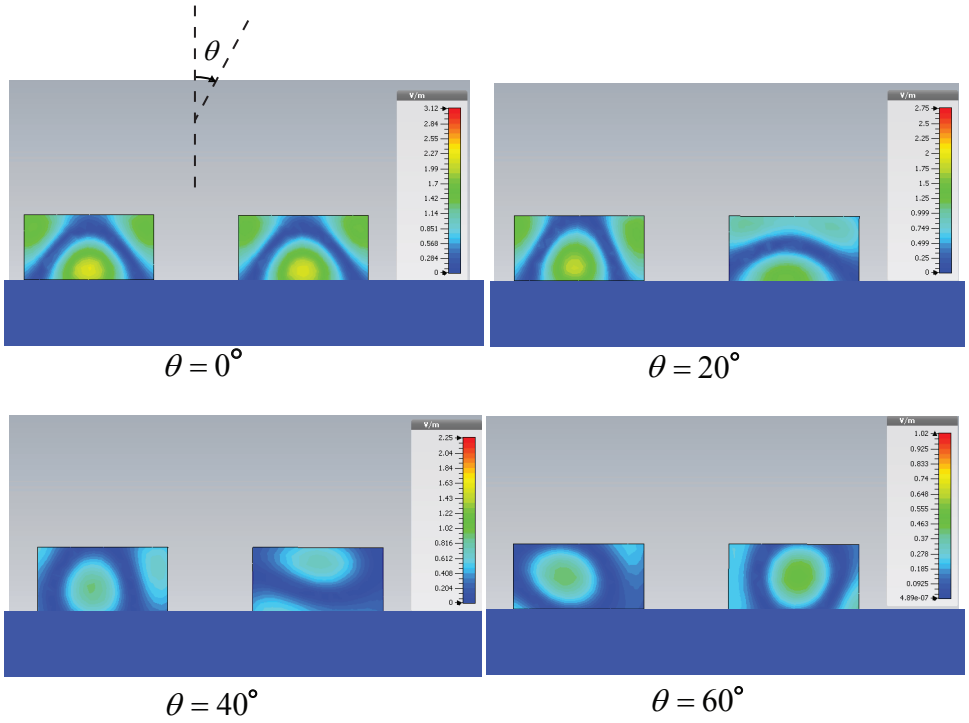

Figure 7.6 Magnitude of electric field distribution in the cross sections of the two optical antenna elements for different angles of incidence. The structure is illuminated with a plane wave with a transverse electric polarization and various different angles of incidence as indicated in each figure.

angle of arrival. By using more complicated coupled-resonator topologies, the proposed nano-antenna array concept can be expanded to develop detectors that are capable of sensing the spectral distribution and state of polarization of the incoming wavefront at the single pixel level with sub-wavelength spatial dimensions. Such detectors are expected to result in the development of new imaging systems at sub-millimeter-wave through the infrared and visible frequency bands.

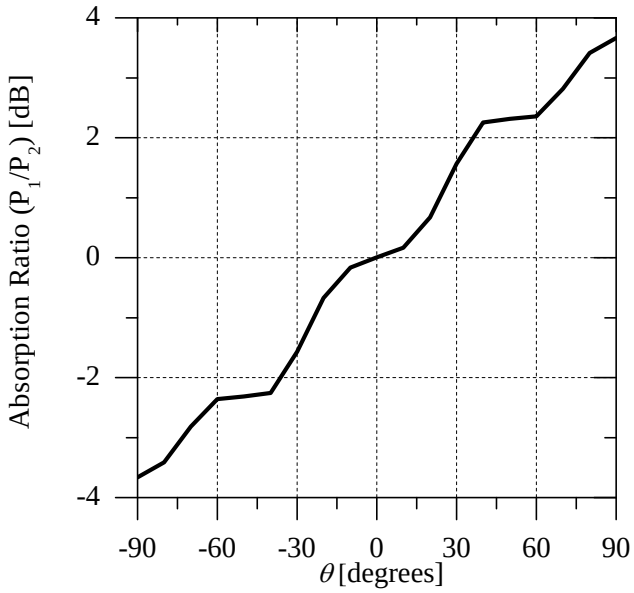

Figure 7.7 Ratio of the power absorbed (dissipated) at the cross sections of the two symmetric elements as a function of the angle-of-incidence. The wavelength of the incident wave is $\lambda = 650nm$.

Chapter 8

Future work

In this thesis, a new class of passive networks have been introduced. Added to small aperture antenna arrays, they increase the angular resolution of the array compared to a regular antenna array. Here I identify three major areas where the present work can be extended:

8.1 Design of small aperture compact direction finding systems

A potential application for BMAAs is in small aperture direction finding systems. By sacrificing bandwidth, passive coupling networks introduced in chapter 5 can increase the angular sensitivity of direction finding systems. In other words, for a given angular resolution, BMAAs proposed in this thesis can lead to a more compact direction finding system. This fact becomes more important when operating at VHF frequencies where the wavelength is quite large compared to dimensions of common wireless devices. Moreover, for a given aperture size, the proposed BMAAs can lead to more accurate angle sensing systems without increasing total system cost and could therefore lead to low-cost systems. A full system analysis of small aperture direction finding systems based on BMAAs is an area of future study.

8.2 MIMO Communications

Another potential application of the BMAAs introduced in this thesis is MIMO communications. As discussed in section 1.1.3 using antenna arrays that are more sensitive to the angle-of-arrival of the incoming signal can lead to more spatial diversity and consequently improved capacity in MIMO communication systems. The investigation of the application of BMAAs in improving the capacity of MIMO communications and the trade-offs involved is an area worth investigation. Due to the fact that signal to noise ratio (SNR) is of utmost importance in any communication system, it is believed that the class of optimum BMAAs discussed in chapter 5 would be more suitable in communication applications.

8.3 Infrared angle sensing detectors

As discussed in chapter 7, the BMAA concept can be extended to infrared and optical frequencies. Chapter 7 merely provided a preliminary analysis of a proof-of-concept optical detector employing two rectangular cross section elements made from silicon. A more detailed analysis of optical multi-element BMAAs using elements with more complicated geometries and other semiconductors is an area of future study. Moreover, investigation of potential applications of optical BMAAs in angle-of-arrival sensing and high resolution optical and infrared imaging can also be an area of study.

LIST OF REFERENCES

[1] C. A. Balanis, *Antenna Theory*, 3rd ed. New York: Wiley, 2005.

[2] H. L. Van Trees, *Optimum Array Processing*, New York: Wiley, 2002.

[3] L. Lu and H. Wu, "Novel Robust Direction-of-Arrival-Based Source Localization Algorithm for Wideband Signals," *IEEE Transactions on Wireless Communications*, vol. 11, no. 11, pp. 3850-3859, November 2012.

[4] Y. Bar-Shalom, et al., *Estimation with Applications to Tracking and Navigation: Theory Algorithms and Software*: Wiley, 2004.

[5] A. A. D'Amico, et al., "DOA and channel parameter estimation for wideband CDMA systems," *IEEE Transactions on Wireless Communications*, vol. 3, pp. 1942-1947, 2004.

[6] "Introduction into Theory of Direction Finding", Rohde & Schwarz, 2012.

[7] R. O. Schmidt, "Multiple emitter location and signal parameter estimation," *IEEE Transactions on Antennas and Propagation*, vol. 34, pp. 276-280, 1986.

[8] R. Roy and T. Kailath, "ESPRIT-estimation of signal parameters via rotational invariance techniques," *IEEE Transactions on Acoustics, Speech and Signal Processing*, vol. 37, pp. 984-995, 1989.

[9] D. R. Wehner, *High-Resolution Radar*: Artech House, Incorporated, 1995.

[10] Q. Huang, et al., "UWB Through-Wall Imaging Based on Compressive Sensing," *IEEE Transactions on Geoscience and Remote Sensing*, vol. 48, pp. 1408-1415, 2010.

[11] Y. Yeo-Sun and M. G. Amin, "High-Resolution Through-the-Wall Radar Imaging Using Beamspace MUSIC," *IEEE Transactions on Antennas and Propagation*, vol. 56, pp. 1763-1774, 2008.

[12] J. G. Proakis and M. Salehi, *Digital Communications*: McGraw-Hill Higher Education, 2008.

[13] S. Liang, et al., "Capacity of MIMO Systems With Mutual Coupling: Transmitter Optimization With Dual Power Constraints," *IEEE Transactions on Signal Processing*, vol. 60, pp. 848-861, 2012.

[14] J. W. Wallace and M. A. Jensen, "Mutual coupling in MIMO wireless systems: a rigorous network theory analysis," *IEEE Transactions on Wireless Communications*, vol. 3, pp. 1317-1325, 2004.

[15] S. J. Wijnholds, et al., "Antenna applications corner: Phased-array antenna system development for radio-astronomy applications," *IEEE Antennas and Propagation Magazine*, vol. 55, pp. 293-308, 2013.

[16] P. E. Dewdney, et al., "The Square Kilometre Array," *Proceedings of the IEEE*, vol. 97, pp. 1482-1496, 2009.

[17] R. C. Hansen, *Electrically Small, Superdirective, and Superconducting Antennas*, Wiley-Interscience, 2006.

[18] M. A. Dawoud and M. A. Hassan, "Design of superdirective endfire antenna arrays," *IEEE Transactions on Antennas and Propagation*, vol. 37, pp. 796-800, 1989.

[19] E. E. Altshuler, et al., "A Monopole Superdirective Array," *IEEE Transactions on Antennas and Propagation*, vol. 53, pp. 2653-2661, 2005.

[20] S. R. Best, et al., "An Impedance-Matched 2-Element Superdirective Array," *IEEE Antennas and Wireless Propagation Letters*, vol. 7, pp. 302-305, 2008.

[21] G. Walker, et al., "Superconducting superdirectional antenna arrays," *IEEE Transactions on Antennas and Propagation*, vol. 25, pp. 885-887, 1977.

[22] I. P. Ivrissimtzis, et al., "Supergain printed arrays of closely spaced dipoles made of thick film high-Tc superconductors," *IEE Proceedings Microwaves, Antennas and Propagation*, vol. 142, pp. 26-34, 1995.

[23] B. N. Getu and R. Janaswamy, "The effect of mutual coupling on the capacity of the MIMO cube," *IEEE Antennas and Wireless Propagation Letters*, vol. 4, pp. 240-244, 2005.

[24] P. S. Kildal and K. Rosengren, "Correlation and capacity of MIMO systems and mutual coupling, radiation efficiency, and diversity gain of their antennas: simulations and measurements in a reverberation chamber," *IEEE Communications Magazine*, vol. 42, pp. 104-112, 2004.

[25] L. Xin and N. Zaiping, "Mutual coupling effects on the performance of MIMO wireless channels," *IEEE Antennas and Wireless Propagation Letters*, vol. 3, pp. 344-347, 2004.

[26] K. R. Dandekar, et al., "Effect of mutual coupling on direction finding in smart antenna applications," *Electronics Letters*, vol. 36, pp. 1889-1891, 2000.

[27] E. M. Friel and K. M. Pasala, "Effects of mutual coupling on the performance of STAP antenna arrays," *IEEE Transactions on Aerospace and Electronic Systems*, vol. 36, pp. 518-527, 2000.

[28] Z. Tong Tong, et al., "Compensation for the mutual coupling effect in the ESPRIT direction finding algorithm by using a more effective method," *IEEE Transactions on Antennas and Propagation*, vol. 53, pp. 1552-1555, 2005.

[29] S. Henault, et al., "A Methodology for Mutual Coupling Estimation and Compensation in Antennas," *IEEE Transactions on Antennas and Propagation*, vol. 61, pp. 1119-1131, 2013.

[30] J. B. Andersen and H. H. Rasmussen, "Decoupling and descattering networks for antennas," *IEEE Trans. Antennas Propag.*, vol. 24, no. 6, pp. 841-846, Nov. 1976.

[31] J. Weber, C. Volmer, K. Blau, R. Stephan, and M. A. Hein, "Miniaturized antenna arrays using decoupling networks with realistic elements," *IEEE Trans. Microw. Theory Tech.*, vol. 54, no. 6, pp. 2733-2740, Jun. 2006.

[32] C. Volmer, et al., "An Eigen-Analysis of Compact Antenna Arrays and Its Application to Port Decoupling," *IEEE Transactions on Antennas and Propagation*, vol. 56, pp. 360-370, 2008.

[33] Y. Yantao and H. Hon Tat, "Design of a Mutual Coupling Compensation Network for a Small Receiving Monopole Array," *IEEE Transactions on Microwave Theory and Techniques*, vol. 59, pp. 2241-2245, 2011.

[34] I. L. Tzung and W. Yuanxun Ethan, "Mode-Based Information Channels in Closely Coupled Dipole Pairs," *IEEE Transactions on Antennas and Propagation*, vol. 56, pp. 3804-3811, 2008.

[35] L. K. Yeung and Y. E. Wang, "Mode-Based Beamforming Arrays for Miniaturized Platforms," *IEEE Transactions on Microwave Theory and Techniques*, vol. 57, pp. 45-52, 2009.

[36] K. F. Warnick and M. A. Jensen, "Optimum noise matching for mutually coupled arrays," *IEEE Trans. Antennas Propag.*, vol. 55, no. 6, pp. 1726-1731, Jun. 2007.

[37] K. F. Warnick, et al., "Minimizing the Noise Penalty Due to Mutual Coupling for a Receiving Array," *IEEE Transactions on Antennas and Propagation*, vol. 57, pp. 1634-1644, 2009.

[38] D. Arceo and C. A. Balanis, "A Multiport Impedance-Matching Feed Network for Directional Antennas," *IEEE Antennas and Wireless Propagation Letters*, vol. 11, pp. 1548-1551, 2012.

[39] A. Michelsen "Hearing and Sound Communication in Small Animals: Evolutionary Adaptations to the Laws of Physics," In: D. B. Webster et al. (eds) The Evolutionary Biology of Hearing, A, Springer, New York, pp. 61-77, 1991.

[40] A. Michelsen, A.V. Popov and B. Lewis, "Physics of directional hearing in the cricket Gryllus Bimaculatus," J. Comp. Physiol., A, vol. 175, pp. 153-164, 1994.

[41] A. Michelsen and O. N. Larsen, "Pressure difference receiving ears," Bioinsp. Biomim., vol. 3, 011001, 2008.

[42] D. Young and K.G. Hill "Structure and function of the auditory system of the cicada, Cystosoma Saundersii," J. Comp. Physiol., A, vol. 117, pp. 23-45, Jan 1977.

[43] U. Kohler and R. Lakes-Harlan, "Auditory behavior of a parasitoid fly (Emblemasoma Auditrix, Sarcophagidae, Diptera)," J. Comp. Physiol., A, vol. 187, pp. 581-587, 2001.

[44] W. Cade, "Acoustically orienting parasitoids: Fly phonotaxis to cricket song," Science, vol. 190, Issue 4221, pp. 190-191, 1975.

[45] A. C. Mason, et. al, "Hyperacute directional hearing in a microscale auditory system," Nature, vol. 410, pp. 686-690, 5 April 2001.

[46] D. Robert, R. N. Miles, and R. R. Hoy, "Directional hearing by mechanical coupling in the parasitoid fly Ormia ochracea," Journal of Comparative Physiology, vol. 179, pp. 29-44, 1996.

[47] R. N. Miles and R. R. Hoy, "The Development of a Biologically-Inspired Directional Microphone for Hearing Aids," Audiology and Neurotology, vol. 11, pp. 96-94, 2006.

[48] H. J. Liu, M. Yu, and X. M. Zhang, "Biomimetic optical directional microphone with structurally coupled diaphragms," Applied Physics Lett., vol. 93, 243902, 2009.

[49] R. N. Miles, Q. Su, W. Cui, "A Low Noise Differential Microphone Inspired by the Ears of the Parasitoid Fly Ormia Ochracea," J. Acoustic. Soc. Am., vol. 125, pp. 2013-2026, 2009.

[50] N. Behdad, M. Al-Joumayly, and M. Li "Biomimetic electrically small antennas," Electronics Letters, vol. 46, pp. 1650-1651, 2010.

[51] N. Behdad, M. Al-Joumayly, and M. Li, "Biologically inspired electrically small antenna arrays with enhanced directional sensitivity," *IEEE Antennas Wireless Propagat. Lett.*, vol. 10, pp. 361-364, 2011.

[52] M. Akcakaya and A. Nehorai, "Biologically inspired coupled antenna beampattern design," *Bioinsp. Biomim.*, vol. 5, pp. 1-11, Dec. 2010.

[53] A. T. D. Hoop, "The N-port receiving antenna and its equivalent electrical network," *Philips Res. Rep.*, vol. 30, pp. 302-315, 1975.

[54] J. W. Wallace and R. Mehmood, "On the Accuracy of Equivalent Circuit Models for Multi-Antenna Systems," *IEEE Trans. on Antennas and Propag.*, vol. 60, no. 2, pp. 540-547, Feb. 2012.

[55] A. R. Masoumi, Y. Yusuf and N. Behdad, "Biomimetic Antenna Arrays Based on the Directional Hearing Mechanism of the Parasitoid Fly *Ormia Ochracea*," *IEEE Trans. on Antennas and Propag., vol. 61, no. 5, pp. 2500-2510, May 2013.*

[56] A. R. Masoumi and N. Behdad,"An Improved Architecture for Two- Element Biomimetic Antenna Arrays," *IEEE Trans. Antennas and Propag.*, vol.61, no. 12, pp. 6224-6228, Dec. 2013.

[57] A. R. Masoumi and N. Behdad,"Architecture, Design, and Nonlinear Optimization of Three-Element Biomimetic Antenna Arrays," *IEEE Antennas and Wireless Propag. Letters*, no. 12, pp.1416-1419, Dec. 2013.

[58] R. Fourer, D. M. Gay, and B. W. Kernighan, AMPL: A Modeling Language for Mathematical Programming, Cengage Learning, 2nd Edition, November 12, 2002.

[59] C. Desoer, "The maximum power transfer theorem for n-ports," *IEEE Transactions on Circuit Theory*, vol. 20, pp. 328-330, May 1973.

[60] C. Volmer, M. Sengul, J. Weber, R. Stephan and M. A. Hein, "Broadband decoupling and matching of a superdirective two-port antenna array," *IEEE Antennas and Wireless Propagation Letters*, vol.7, pp. 613-616, 2008.

[61] T. Lee and Y. E. Wang, "Mode-based information channels in closely coupled dipole pairs," *IEEE Trans. Antennas Propag.*, vol. 56, no. 12, pp. 3804-3811, Dec. 2008.

[62] R. C. Hansen, *Electrically Small, Superdirective, and Superconducting Antennas*, Wiley-Interscience, 2006.

[63] J. G. Linvill, "Transistor Negative Impedance Converters," *Proc. IRE*, vol. 41, pp. 725-729, Jun. 1953.

[64] S. E. Sussman-Fort and R. M. Rudish, "Non-Foster impedance matching of electrically-small antennas," *IEEE Trans. Antennas Propag.*, vol. 57, no. 8, pp. 2230-2241, Aug. 2009.

[65] H. Mirzaei and G. V. Eleftheriades, "A Resonant Printed Monopole Antenna With an Embedded Non-Foster Matching Network," *IEEE Transactions on Antennas and Propagation*, vol. 61, pp. 5363-5371, 2013.

[66] C. R. White, et al., "A Non-Foster VHF Monopole Antenna," *IEEE Antennas and Wireless Propagation Letters*, vol. 11, pp. 584-587, 2012.

[67] E. D. Palik, *Handbook of Optical Constants of Solids*, Academic Press, Burlington, 1997.